THE UNIVERSITY OF TEXAS AT AUSTIN
CENTER FOR TRANSPORTATION RESEARCH

TECHNICAL REPORT 0-6873-1
TxDOT PROJECT NUMBER 0-6873

Development of a Laser-based Sensor to Measure True Road Surface Deflection

Jorge A. Prozzi
Christian Claudel
Praveen Pasupathy
Ambika Verma
Joaquin B. Hernandez

August 2016; Published April 2017

http://library.ctr.utexas.edu/ctr-publications/0-6873-1.pdf

Technical Report Documentation Page

1. Report No. FHWA/TX-16/0-6873-1	2. Government Accession No.	3. Recipient's Catalog No.
4. Title and Subtitle Development of a Laser-based Sensor to Measure True Road Surface Deflection		5. Report Date August 2016; Published April 2017
		6. Performing Organization Code
7. Author(s) Jorge A Prozzi, Christian Claudel, Praveen Pasupathy, Ambika Verma, and Joaquin B Hernandez.		8. Performing Organization Report No. 0-6873-1
9. Performing Organization Name and Address Center for Transportation Research The University of Texas at Austin 1616 Guadalupe St., Suite 4.202 Austin, TX 78701		10. Work Unit No. (TRAIS) 11. Contract or Grant No. 0-6873
12. Sponsoring Agency Name and Address Texas Department of Transportation Research and Technology Implementation Office P.O. Box 5080 Austin, TX 78763-5080		13. Type of Report and Period Covered Technical Report April 2015–August 2016 14. Sponsoring Agency Code
15. Supplementary Notes Project performed in cooperation with the Texas Department of Transportation and the Federal Highway Administration.		
16. Abstract The high-speed measurement of accurate pavement surface deflections under a moving wheel at a network-level still remains a challenge in pavement engineering. This goal cannot be accomplished with stationary deflection-measuring devices. Engineers recognize the usefulness of pavement deflection data to evaluate and monitor pavement response and existing pavement structural conditions. Network-level studies of pavement structure are being performed but have major limitations such as lack of accurate measurements, no true deflection is measured at any point, complexity, and safety concerns. The purpose of this project is to develop a laser measuring system for network-level studies that continuously moves along the pavement at speed above 10 mph.		
17. Key Words Deflection, Laser System, Network-level study, Laser Scanner	18. Distribution Statement No restrictions. This document is available to the public through the National Technical Information Service, Springfield, Virginia 22161; www.ntis.gov.	

19. Security Classif. (of report) Unclassified	20. Security Classif. (of this page) Unclassified	21. No. of pages 102	22. Price

Form DOT F 1700.7 (8-72) Reproduction of completed page authorized

THE UNIVERSITY OF TEXAS AT AUSTIN
CENTER FOR TRANSPORTATION RESEARCH

Development of a Laser-based Sensor to Measure True Road Surface Deflection

Jorge A Prozzi
Christian Claudel
Praveen Pasupathy
Ambika Verma
Joaquin B Hernandez

CTR Technical Report:	0-6873-1
Report Date:	August 2016; Published April 2017
Project:	0-6873-1
Project Title:	True Road Surface Deflection Measuring Device
Sponsoring Agency:	Texas Department of Transportation
Performing Agency:	Center for Transportation Research at The University of Texas at Austin

Project performed in cooperation with the Texas Department of Transportation and the Federal Highway Administration.

Center for Transportation Research
The University of Texas at Austin
1616 Guadalupe St, Suite 4.202
Austin, TX 78701

http://ctr.utexas.edu/

Disclaimers

Author's Disclaimer: The contents of this report reflect the views of the authors, who are responsible for the facts and the accuracy of the data presented herein. The contents do not necessarily reflect the official view or policies of the Federal Highway Administration or the Texas Department of Transportation (TxDOT). This report does not constitute a standard, specification, or regulation.

Patent Disclaimer: There was no invention or discovery conceived or first actually reduced to practice in the course of or under this contract, including any art, method, process, machine manufacture, design or composition of matter, or any new useful improvement thereof, or any variety of plant, which is or may be patentable under the patent laws of the United States of America or any foreign country.

Notice: The United States Government and the State of Texas do not endorse products or manufacturers. If trade or manufacturers' names appear herein, it is solely because they are considered essential to the object of this report.

Engineering Disclaimer

NOT INTENDED FOR CONSTRUCTION, BIDDING, OR PERMIT PURPOSES.

Research Supervisor: Dr. Jorge Prozzi

Acknowledgments

The authors express appreciation to all personnel from the Texas Department of Transportation that contributed to this research project and provided the research team with useful guidance and continuous support. In particular, we would like to thank Wade Odell from the Research and Technology Implementation Office. In addition, the following people are acknowledged for their technical contribution and advice: Doug Eichorst II (DE Lubbock District), Magdy Mikhail and Robin Huang (Maintenance Division), and Gisel Carrasco (Construction Division).

Products Included

Chapter 6 describes the measuring sensor (0-6873-P2) created for this project. The sensor is at The University of Texas at Austin for continuing the research in Phase 2 of this project. The sensor setup consists of the following components:

- Two laser displacement sensor heads, LJ-V7300
- One laser displacement controller, LJ-V7001P
- 24V DC power supply, CA-U4
- Cable, CB-B3

Table of Contents

List of Figures

List of Tables

Chapter 1. Deflection Measuring Systems

The measurement of pavement surface deflection under a moving wheel with high-fidelity presents several challenges in pavement engineering today. Pavement deflection measurements began more than 60 years ago with the development of the Benkelman Beam (BB) as part of the WASHO Road Test. Engineers have always recognized the usefulness of pavement deflection data to evaluate and monitor pavement response (e.g., maximum deflection, radius of curvature) and existing pavement structural conditions (by means of backcalculation of layer moduli). The Texas Department of Transportation (TxDOT) has been, and continues to be, one of the leaders in using deflection data (TxDOT operates a large fleet of falling weight deflectometers [FWD]) as well as in developing and implementing devices used to measure pavement deflections. Two examples of TxDOT supporting the development of new devices are the Rolling Dynamic Deflectometer (RDD) and the Total Pavement Acceptance Device (TPAD) (Stokoe et al., 2013). These two devices, developed over the past six decades for pavement deflection measurements, are briefly discussed in the following sections. However, these devices do not measure pavement deflection under a standard axle load and they operate at very low speeds.

Since the goal of this project is to develop a measuring device for project- and network-level studies that continuously moves along the pavement at speeds above 10 mph, all stationary detection-measurement devices such as the FWD, the Road Rater, and the Dynaflect are excluded from this discussion, as they do not meet the technical objectives. Our goal is to develop a device that can measure actual deflection under a fully loaded axle at a speed of 10 mph.

All continuous (or quasi-continuous) pavement deflection measurement devices have loading systems that move along with the measuring vehicle. There are two major differences between these devices: (1) some deflection sensors move along the pavement at the speed of the device while other sensors are stationary on the pavement as the loading mechanism moves past the sensor, and (2) the speed along the pavement differs from very slow to fast.

We have identified eight available devices that are currently used to perform pavement deflection measurements. These devices are divided into four groups:

- very slow moving load and stationary sensors (speed < 1 mph)
- slow moving load and sensors (speed < 3 mph),
- moderate moving load and stationary sensors (speed ~ 10 mph), and
- fast moving load and sensors (speed > 40 mph).

Not all devices are appropriate for network-level studies, but they have all historically contributed to understanding pavement deflection measurements. This project aims to develop a device that operates just above 10 mph.

1.1 Benkelman Beam (BB)

This device was developed in 1953 by A.C. Benkelman of the U.S. Bureau of Public Roads. The BB was first used on the WASHO Road Test in 1953. This device is still in use today and commercially available. For the BB test, a moving truck wheel is used to apply loading onto the

pavement and the resulting deflections of the pavement surface are measured by a stationary dial gauge.

A simplified drawing of the BB is shown in Figure 1.1. It is composed of a stationary reference frame and a probe arm pivoting at one point supported by the reference frame. During testing, the probe point is positioned between the dual rear wheels of a loaded truck. The reference frame is leveled and the first reading is taken. When the loaded truck moves away, the second reading on the dial gauge is taken. The maximum pavement movement is equal to the difference between the first and second readings times the lever-arm multiplier. The main advantage is that it measures actual pavement deflection directly; however, it is not efficient.

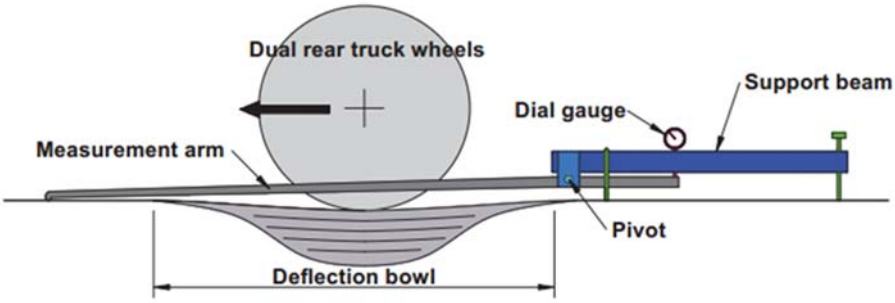

Figure 1.1 Simplified side views of the BB (Baltzer et al., 2010)

1.2 Road Surface Deflectometer (RSD)

The RSD was developed by the Council for Scientific and Industrial Research in South Africa and is used to measure surface deflection under a loaded, moving wheel (Prozzi, 1994). The RSD is an upgraded BB that uses two reference feet at the stationary end for stability and one measuring point at the other end. The RSD is shown taking deflection measurements in Figure 1.2. For testing, the standard 18-kip axle load is used, as is a linear variable differential transformer (LVDT). The beam is 10 ft long and thin enough to be located between the dual tires of the moving load.

Like the BB, the RSD measures actual deflection directly without the need to process the signal. In addition, the RSD measures the entire deflection bowl while the BB determines only the maximum deflection. However, as with the BB, the RSD is stationary and therefore not very efficient.

Figure 1.2 RSD during deflection measurements

1.3 LaCroix Deflectograph

The Lacroix Deflectograph is a moving deflection measuring device that was developed in the mid-1960s by the Laboratoire Central des Ponts et Chaussees in France. Basically, it is an automatic version of the BB, performing two sets of deflection measurements (with one BB in each wheel path) to capture the deflections created by a specified axle load. The Lacroix Deflectograph is shown during testing in Figure 1.3.

First, the frame holding the backward-pointing measurement system is positioned in each wheel path between the dual wheels. The truck moves at a speed of slightly less than 2.0 mph. During the measurement cycle, the frame remains stationary on the pavement while the loaded tires move along the measurement length. Then wires and a guidance system move the measurement frame to a new position along the road, and the procedure is repeated. The distance between measurements is about 10 to 20 ft depending on the vehicle used and the testing speed. The Lacroix Deflectograph was the first commercially available device capable of measuring actual deflection under a moving axle load. It is a very good and robust piece of equipment; however, the operational speed is below our target.

(a) Start of Test Cycle **(b) End of Test Cycle**

Figure 1.3 Testing with LaCroix Deflectograph

1.4 Rolling Dynamic Deflectometer (RDD)

The RDD was developed by at the University of Texas at Austin's Center for Transportation Research in the 1990s under TxDOT's research program and has been used for about 15 years as a valuable tool for project-level pavement deflection under a dynamic vibratory load. The RDD applies a static hold-down force combined with a dynamic sinusoidal force to the pavement surface with two loading rollers while continuously moving along the pavement. An array of rolling sensors is used to measure continuously the induced dynamic pavement deflections. By applying the load at a pre-determined frequency and by filtering the response, many of the signal-to-noise ratio issues are circumvented.

The device moves along the pavement at a speed of about 1.0 mph, so it is used only for project-level studies. Each of the rolling sensors consists of a three-wheeled cart supporting a vertically oriented velocity transducer (geophone) with a 2-Hz resonant frequency. The RDD is a truck-mounted device upon which an electro-hydraulic loading system is used to deliver the dynamic forces to the pavement (see Figure 1.4). The array of rolling sensors is positioned on the pavement along the longitudinal centerline of the truck, beginning mid-way between the loading rollers and extending ahead of the rollers.

Due to the close spacing between deflection measurements, the RDD has become an invaluable device for monitoring joints in jointed concrete pavements. To date, its main application is for airport pavements.

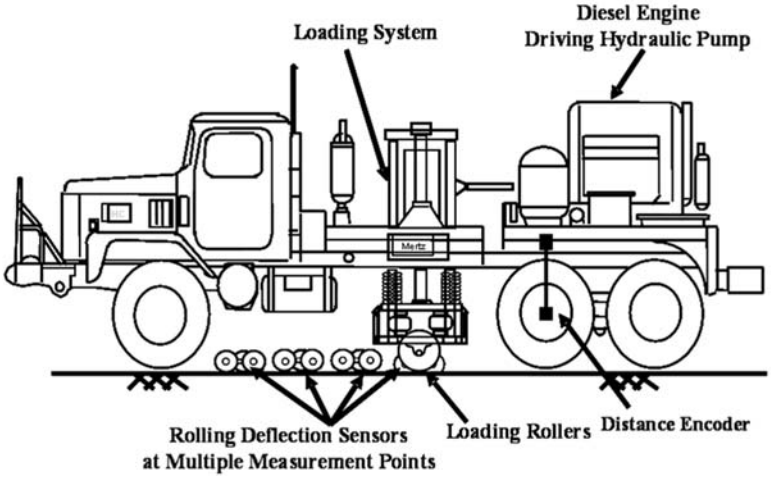

Figure 1.4 Schematic diagram of the RDD

1.5 Total Pavement Acceptance Device (TPAD)

The TPAD (Figure 1.5) was developed through TxDOT's research program by a joint effort between UT Austin's Center for Transportation Research and the Texas Transportation Institute. The objectives of developing this device were to integrate multiple testing functions into one piece of equipment and to increase the speed along the pavement. The TPAD provides multiple functions: (1) RDD, (2) ground penetrating radar (GPR), (3) global positioning system (GPS), (4) pavement surface temperature, (5) digital video imaging of pavement and right-of-way conditions, and (6) longitudinal survey distances.

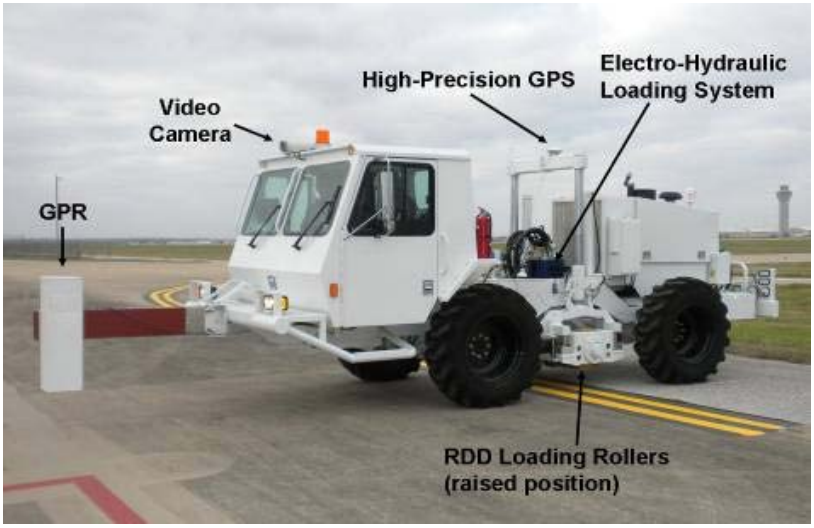

Figure 1.5 Photograph of the TPAD

The continuous testing speed of the TPAD is 2.0 to 3.0 mph, which, at this time, still places it in the realm of project-level studies. Above this speed range, the signal-to-noise ratio becomes unacceptably large. The principle of the TPAD pavement deflection measurements is the same as the RDD, so 2-Hz geophones are used as transducers.

1.6 Curviameter

The Curviameter was jointly developed between France and Spain in 1970s and was the first device with which "quasi-continuous" pavement deflections were measured. The basic principle of the Curviameter is that geophones are mounted on a continuous closed-loop chain that positions the geophones to remain stationary while dual rear wheels travel past them. The particle velocity of the pavement surface during passage of the rear wheels is measured (Geem, 2010). Since geophones measure the velocity of the deflection, simple integration of the signal is necessary.

In October 2013, the University of Texas at Austin organized a demonstration of the Curviameter (model MT 3000.2) for TxDOT at the Bull Creek office of the Maintenance Division (see Figure 1.6 and 1.7). This model has a testing speed of 10 mph and 50-ft-long closed-loop chain with three geophones on the chain.

Figure 1.6 Detail of Curviameter measuring system

Figure 1.7 Detail of Curviameter's geophone on the pavement surface

When placed on the pavement, each geophone remains stationary (Figure 1.7) because the chain is moving in the opposite direction of the vehicle but at the same speed. For the model evaluated, stationary measurement points are generated every 16.4 ft. The Curviameter can measure both the deflection-time history and the curvature of the deflection bowl at each stationary measurement point. The geophone starts measuring deflections when the rear axle is several feet away from the location of the geophone and stops measuring when the rear axle passes the geophone's location by about 10 ft. A rear axle of the Curviameter is loaded to weigh 18 to 29 kips.

To date, this is the closest device to meeting the technical objectives of the research study. The main limitation of the Curviameter is that above 10 mph the chain used to hold the geophones down onto the pavement surface starts affecting the geophone signal. It should also be noted that the chain also acts as the power and data transmission line. It is believed that the implementation of wireless technologies could simplify the design of the chain and considerably improve the current operation range of the Curviameter.

1.7 Rolling Wheel Deflectometer (RWD)

The RWD was developed by Applied Research Associates, Inc., to measure pavement surface deflections at traffic speeds and to characterize the load carrying capacity of in-service pavements (Gedafa et al., 2008). The first prototype was introduced in the late 1990s and was designed to perform measurements on airfield pavements at a maximum speed of 6 mph (Elseifi, 2012). The latest version of the RWD was introduced in 2003 and can collect deflections at traffic speeds. It consists of a 53-ft. long semitrailer (Figure 1.8) applying a standard 18,000-lb. load on the pavement structure by means of a regular dual-tire assembly over the rear single axle.

Figure 1.8 General view of RWD

The RWD measures wheel deflections at the pavement surface by means of a spatially coincident method, which compares the profiles of the surface in both undeflected and deflected states. This method was originally developed by the Transport and Road Research Laboratory and furthered by Dr. Milton Harr at Purdue University. As the RWD travels on top of the pavement, triangulation lasers, mounted on a 25.5-ft. aluminum beam and placed at 8-ft. intervals, are used to measure surface deflections. The intervals can be varied in response to the temperature, speed, and property of the pavement. The beam is mounted on the right side of the semitrailer to follow the right wheel path on the right lane, which is usually the weakest location on the pavement structure. Three spot lasers are placed in front of the loaded wheel to define the unloaded surface, and one spot laser is placed directly on top of the loaded dual-tire assembly in order to measure the deflected surface (Figure 1.9). The laser sensors are set to collect a reading at a fixed interval of 0.6 in. at all truck speeds.

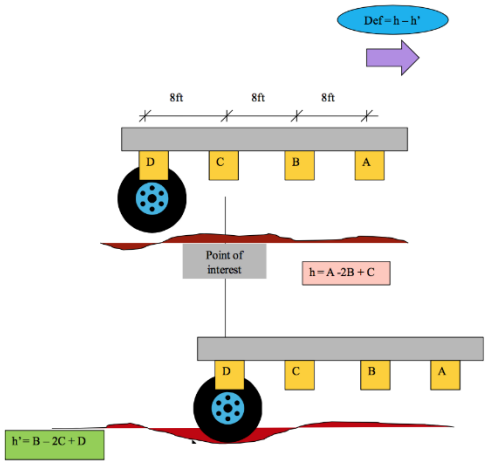

Figure 1.9 Illustration of the spatially coincident method

There are two steps in this measurement process. Three equally separated points ahead of the load wheel are measured by the lasers. When the RWD has moved forward a distance equal to the sensor separation distance, these points are measured again by using the second, third, and fourth sensor. An important requirement for the accuracy of this measurement is that sensor A, B, and C must be positioned out of the deflection basin. Sensor C is the critical one because it is

nearest the loaded wheel. The deflections are measured in real time at a frequency of 2 kHz, and they are averaged every 0.1 mile.

The first measurement uses the front three sensors to measure the three points on the pavement surface, the second measurement is made over the same three points, but use the back three sensors. That is, sensor D is located where sensor C was previously, sensor C is located where sensor B was, etc. A high-resolution encoder mounted on the axle of one of the RWD tires is used to take data after moving a specified distance.

Assuming the beam is rigid with negligible bending, the profile defined by readings B2 and C2 is shifted in slope and magnitude to fit the previous readings at the same locations, A1 and B1. This allows for a comparison of the pavement surface at the same location between its undeflected and deflected states (i.e., D2 and C1). Deflection is then calculated using the following equation:

$$\text{Deflection}=[(B2 - 2C2 + D2) - (A1 - 2B1 + C1)]$$

where

A1, B1 and C1 = laser readings at A, B, and C at time=0; and

B2, C2 and D2 = laser readings at B, C, and D after 8 ft of travel.

A high-resolution encoder mounted on the axle commands the system to take data after moving a specified distance. To ensure maximum deflection measurement accuracy, the odometer should have a total error rate of no more than 2%—approximately 50 mm in 274 cm. This device presents two constraints:

1. The pavement sensors must sequentially pass over identical areas of pavement.
2. The pavement sensors must never move with respect to each other.

A 0.1 mm error due to a pavement sensor that has moved vertically is manifested as a 0.3 mm deflection error; in fact, the algorithm magnifies sensor movement errors. The algorithm requires the sensors to remain vertically fixed with respect to each other at all time. Laser signals are acquired by a data acquisition board installed in a desktop computer located in the RWD trailer (Elseifi et al., 2012). Applied Research Associates has developed software that powers the lasers, generates output files, and stores the files on the computer hard drive. The laser readings are referenced longitudinally by monitoring the anti-lock braking system tone counter that is part of the rear-axle braking system. The data acquisition system is also capable of handling outputs from the accelerometers mounted on the aluminum beam. The accelerometers are used for monitoring beam movements and diagnostic purposes during prototype development. Currently, the data are post-processed within minutes of collection on the computer used for data collection.

The main limitation of the RWD is that it does not measure deflection at any given point but only the average deflection over a given distance. Therefore, it doesn't so much measure deflection as provide an indicator of the pavement deflection over a relatively large area. Although not an actual deflection value, this is a good indicator of overall network condition. However, the RWD results cannot be used for backcalculation purposes.

1.8 Traffic Speed Deflectometer (TSD)

The TSD is a truck-trailer combination; the trailer can apply a 22,000-lb (10-ton) axle load. The movement of the pavement surface caused by the axle load is measured with four Doppler

laser sensors (Krarup et al., 2006). Figure 1.10 shows the TSD and positions of the Doppler laser sensors in the trailer. The first laser sensor measures the undeflected profile of the pavement while other three laser sensors close to the loading wheels measure the deflected profile. The number of the sensors can reach up to 10 depending on the request of the customer. The testing speed is up to 50 mph (Ferne et al., 2009; Jenkins, 2009; Katicha and Flintsch, 2015).

As the TSD moves along the pavement, the pavement surface in front of the wheel moves downward, creating a deflection-time history from which deflection bowl can be determined. The vertical pavement deflection velocities are recorded at a very high rate. Then, deflection slopes at discrete points along the TSD route can be obtained by dividing deflection velocities by the instantaneous vehicle speed. The absolute deflections can be obtained by integrating the deflection slopes either numerically or using a closed-form solution of a mechanical model (Imou et al., 2001; Pedersen, 2012; Muller and Roberts, 2013; Zofka and Sudyka, 2015). It should be noted that the TSD does not measure actual deflection at a given point but take averages over distances. As in the case of the RWD, these measurements are good indicators of pavement response and condition but by no means are actual deflections.

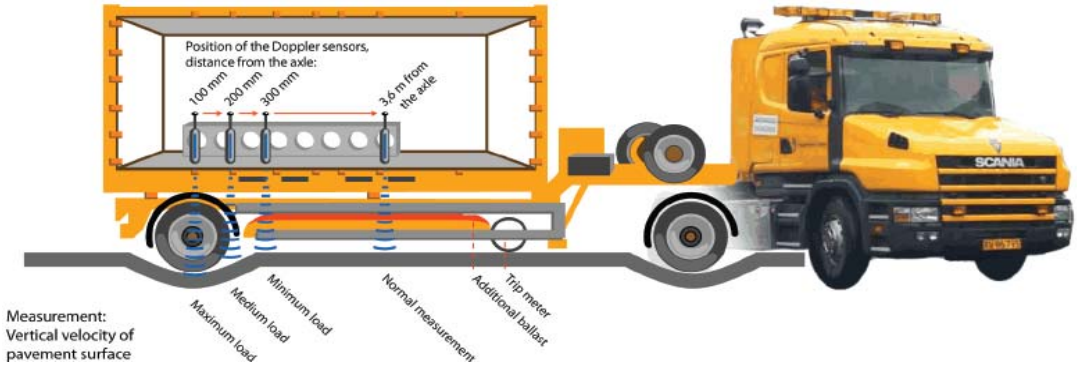

Figure 1.10 Schematic diagram of the TSD

The TSD uses Doppler lasers mounted at a small angle to measure the horizontal vehicle velocity, the vertical and horizontal vehicle suspension velocity, and the vertical pavement deflection velocity (Krarup et al., 2006). The lasers are pointed at a slight angle at the road directly in front of the rear wheelset, illustrated in Figure 1.11.

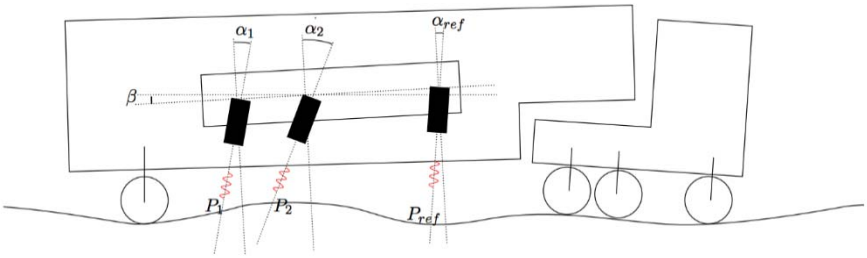

Figure 1.11 An illustration of the measurement situation

The use of Doppler lasers means that we must consider the Doppler effect, which refers to the change in frequency of a wave for an observer moving relative to its source. Figure 1.12 shows a block diagram of a typical conventional ultrasonic Doppler speed sensor. An oscillator generates

a standard signal of frequency F_0. It is amplified and transmitted from a transmitter to the ground surface in an inclined direction. The sonic wave is reflected diffusely on the ground where it is separated into many weak sounds, a few of which are received by a receiver. The Doppler effect causes the frequency to be shifted. If F_D denotes the Doppler shift, the frequency of the received signal is F_0+F_D (Imou et al., 2001):

$$F_D = F_0\left(\frac{C_S + V\cos\beta}{C_S - V\cos\alpha} - 1\right)$$

where Cs is the velocity of sound in air, V is the vehicle velocity relative to the ground, α is the angle between the vehicle velocity vector and the transmitted direction of the ultrasonic wave, and β is the supplement of the angle between the vehicle velocity and the direction of the received wave. The signal is amplified and mixed with the transmission signal in a mixer to create the beat-frequency signals. Therefore, the output frequency, F_{OUT}, is equal to the absolute value of Doppler shift $|F_D|$. If the vehicle velocity is much less than the sound velocity, then:

$$F_{OUT} = |F_D| = F_0\left|\frac{C_S + V\cos\beta}{C_S - V\cos\alpha} - 1\right| \approx F_0\frac{|V|}{C_S}(\cos\alpha + \cos\beta)$$

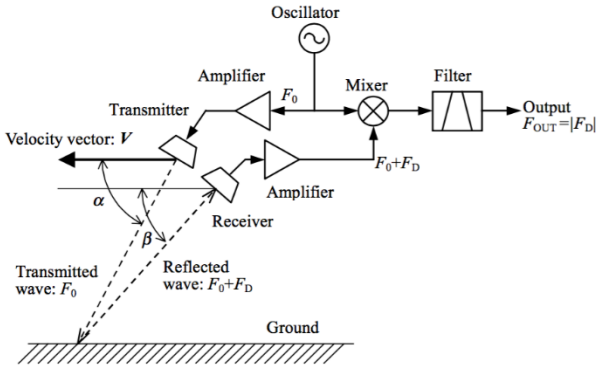

Figure 1.12 Block diagram of a conventional ultrasonic Doppler speed sensor

One drawback of the TSD is that it cannot decide the movement direction; at low velocity, accurate measurement is difficult because the output frequency approaches zero.

A modified version, shown in Figure 1.13, can solve these problems. An oscillator generates the standard signal, which is divided into the transmission frequency F_0. The signal is amplified and transmitted to the ground. The frequency of the received signal (F_0+F_D) is multiplied by k through a frequency multiplier, which helps improve the resolution of measurement of the transient speed.

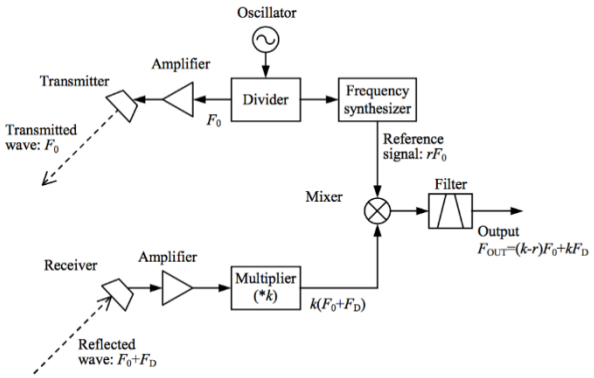

Figure 1.13 Block diagram of the modified Doppler speed sensor

The output frequency is expressed as:

$$F_{OUT} = \left|k(F_0 + F_D) - rF_0\right| = \left|(k-r)F_0 + kF_D\right|$$

We can choose the suitable value of r to keep the value of $(k\text{-}r)\,F_0+kF_D$ positive. However, FD is negative when the vehicle travels in reverse. Hence,

$$F_{OUT} = (k-r)F_0 + kF_D \approx kF_0\left\{\frac{k-r}{k} + \frac{V(\cos\alpha + \cos\beta)}{C_S}\right\}$$

Forward and reverse motions can be distinguished as the output frequency increases in forward motion and decreases in reverse motion.

One of the most challenging aspects in using TSD is the calibration procedure. For ideal operation, the lasers require a constant velocity input. This cannot be achieved by mounting the lasers perfectly vertically, as they would then measure the highly variable vertical suspension movements of the trailer. The problem is solved by mounting the lasers at an angle of approximately two degrees from the vertical. This gives an approximately constant speed input, as a component of the horizontal vehicle velocity is measured, but has little effect on the component of vertical velocity measured. The lasers measure velocities from three sources: horizontal vehicle velocity, vertical and horizontal vehicle suspension velocities, and vertical pavement deflection velocity. As an error in angle of 0.005 degrees could cause a 25% error in the final results, thus making the calibration process necessary.

Dynamic calibration methods rely on being able to drive a measurement comparable to that made by the TSD. Therefore, for our research project it was decided that investigating instrumentation mounted in the pavement to measure the pavement response was the important way forward. The accelerometer was chosen because of its low cost, the easy installation procedure, etc. Figure 1.14 shows the position of the accelerometer in the study by Arraigada and Part (2006 and 2009).

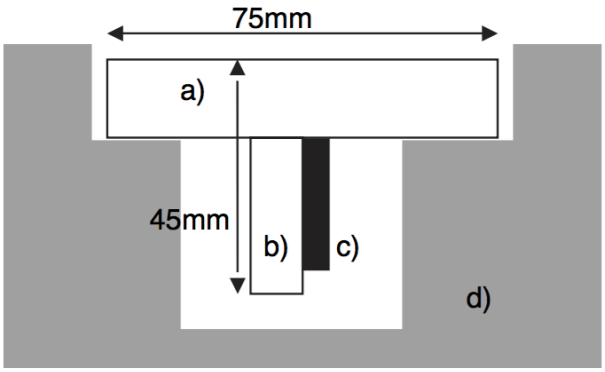

Figure 1.14 Accelerometer mounting (approximate dimensions are shown): (a) circular steel top plate, (b) steel mounting plate, (c) accelerometer, and (d) road surfacing

Arraigada and Part (2006, 2009) used an FWD in conjunction with accelerometers. The FWD was used to verify that accelerometer was functioning correctly. The FWD tests were made with the loading plate placed centrally over the accelerometer, and the time histories from the central geophone were recorded along with the accelerometer output. The responses of the two instruments could then be compared to check that the response from the accelerometer was reasonable. The results for the concrete section are shown in Figure 1.15. The two instruments recorded very similar results. This result confirmed that the accelerometer was accurately reproducing the pavement response.

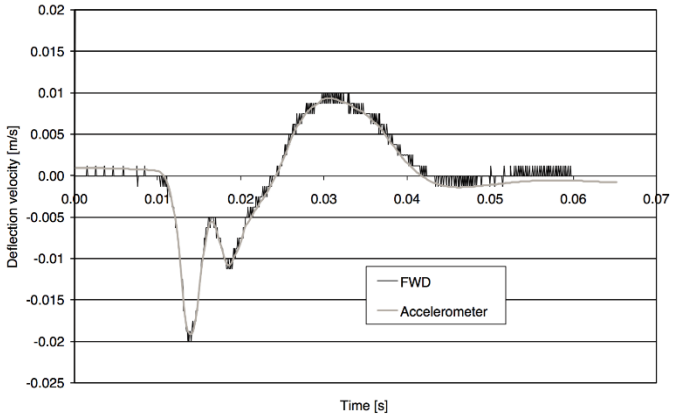

Figure 1.15 Result comparison between FWD and accelerometer

The total velocity measured by the lasers depends on three parameters: horizontal velocity of the TSD, deflection velocity of the pavement, and the laser angle from the vertical (Figure 1.16).

$$V_{total} = V_{vertical} \cos(\theta_{absolute}) + V_{horizontal} \sin(\theta_{absolute})$$

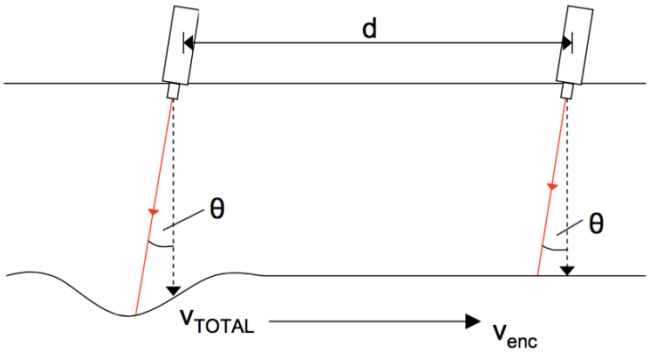

Figure 1.16 Schematic diagram of measurement principle

The maximum deflection velocity recorded on the concrete is on the order of 3 mm/s, the difference between using the cos term and assuming that it's equal to 1 is on the order of just 2 um/s—that is, a percentage error of 0.07%.

$$\theta_{absolute} = \sin^{-1} \frac{V_{total} - V_{vertical}}{V_{horizontal}}$$

The numerator can be thought of as a modification to the recorded velocity to remove the measured deflection velocity and as such is renamed *Vmodified*:

$$\theta_{absolute} = \sin^{-1} \frac{V_{modified}}{V_{horizontal}}$$

Because of the noisy velocity result, it's better to use the distance instead of velocity by integrating them. The horizontal distance traveled (*Dhorizontal*) can be provided by the encoder wheel onboard the TSD. *Dmodified* can be found simply by numerical integration of *Vmodified* with respect to time (*t*). So the angle of the laser can be obtained by,

$$\theta_{absolute} = \sin^{-1} \frac{D_{modified}}{D_{horizontal}}$$

To explain the approach to get the deflection profile of the pavement surface, consider an example in which the TSD vehicle is moving at a constant speed. After a very short period, the deflection of one certain point can be expressed as a function of the average vertical velocity over the period,

$$dy = \bar{V}_V dt.$$

while the horizontal displacement and velocity of the TSD vehicle are also related to the same time period,

$$dx = V_H dt.$$

Then, we can get,

$$dy = \frac{\bar{V}_V}{V_H} dx.$$

Although only some sensors are used to measure the velocity, we can fit a curve along a relative long distance. This could for example be a polynomial fit. These quantities are illustrated in Figure 1.17.

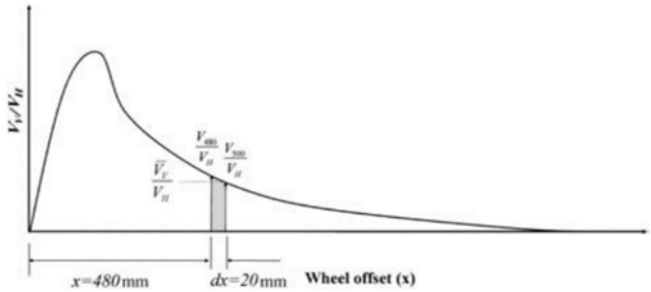

Figure 1.17 Relationship between Vv/VH and wheel offset

In the limiting case where $dx \to 0$, the entire deflection bowl can be determined by numerically integrating the plot of slope (*S)* versus wheel offset (*x*), working from the edge of the deflection bowl towards the wheel load; see Figure 1.18.

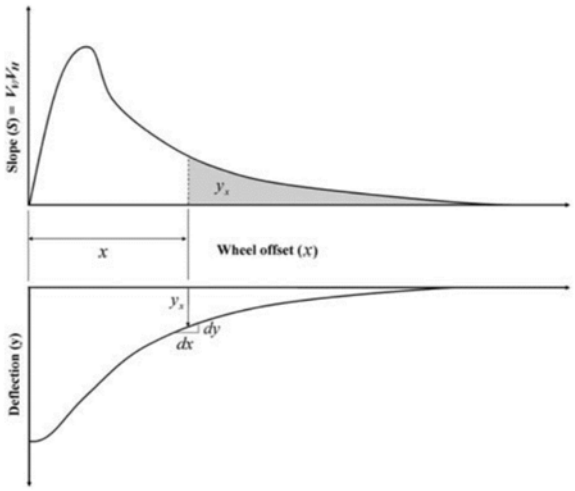

Figure 1.18 Slope and deflection file measured by TSD

1.9 Summary of Reviewed Devices

Obtaining high-fidelity pavement deflections at the network level cannot be accomplished with stationary deflection-measuring devices such as the FWD, which is the prevalent deflection measuring device in Texas.

As discussed in this chapter, at least eight moving-load devices for pavement deflection measurements have been developed over the past 60 years and are still in use. Two devices, the BB and the RSD, are stationary and therefore too slow for network-level studies; however, both

measure deflection directly without the need of data processing and the development of algorithms to integrate the signal.

Another three devices—LaCroix Deflectograph, RDD, and TPAD—work well in project-level studies but would need significant improvements to even be considered for network-level studies.

It should be noted that for the purposes of this project, we defined a device potentially capable of performing network-level evaluation as one that can measure actual deflection under an actual fully loaded axle at a speed of at least 10 to 11 mph. Theoretically such a device will be able to travel the entire TxDOT network in one year. Therefore, two or three such devices will be able to provide full network coverage on an annual basis.

To date, relatively effective network-level studies are being performed with the Curviameter (which travels at about 10 mph and employs stationary geophones to continuously measure pavement deflections), and the RWD and the TSD, which travel at 40 to 60 mph and use laser-based sensors. However, the major problem with the RWD and TSD devices is the lack of fidelity in the measurements due to pavement texture and roughness leading to determining average deflections over fifty to hundreds of ft. In terms of the Curviameter, the fidelity of the measurement is high but the complexity and mass of the continuous chain mechanism to locate the geophones inhibit improvements in testing speed and continuity of measurements.

Chapter 2. Pavement Deflection Measurement Sensors

The selection of a suitable and accurate sensor for the measurement of pavement deflection is essential for the success of this project. Commonly used measuring sensors employed in the past include dial gauges, LVDTs, geophones, and lasers. A brief description of some of these measuring sensor technologies is presented in this chapter.

2.1 Linear Variable Differential Transformer (LVDT)

An LVDT is a transducer designed to measure linear displacements. The main components of an LVDT are a cylindrical ferromagnetic core and a coil assembly formed by one primary and two secondary windings. The measured linear displacement is applied to the core, which moves frictionless through the cylindrical coils. The primary coil is charged with an alternating current that generates a variable magnetic flux. This flux is channeled through the magnetic core, which induces a voltage to the secondary coil proportional to the position of the core. The device is calibrated in order to translate the secondary voltage into the amount of physical linear displacement as well as the direction of the displacement.

LVDT sensors are widely used for industry applications and in civil engineering testing laboratories. They are considered reliable, long-life sensors and are designed to support a wide range of external conditions. The main advantage of LVDTs is the fact that the generated voltage is directly proportional to the displacement, so no further integration of the signal is required. They are also very robust and reliable, so we intend to use LVDTs to obtain our reference measurements against which we will compare other sensors.

2.2 Geophones

Geophone sensors are designed to measure linear displacement velocity using a spring-mounted magnetic mass and a coil. They are typically used in seismology to measure vertical displacement of the earth's surface. The motion of the ground activates inertial forces to the hanging mass, resulting in differential movement with respect to the coil (which is fixed to the ground). The relative movement of the magnetic mass induces an electric voltage in the coil that is proportional to the velocity at which the ground is moving. The variation of induced voltage is translated to physical linear displacement. The signal has to be integrated once to obtain displacement.

It is important to note that geophones are used in the FWD, the Curviameter, the RDD, and the TPAD. Therefore, to date, the geophone seems to be the sensor of preference for speeds up to 10 mph. Above 10 mph, laser systems seem to be the preferred sensor technology.

2.3 Accelerometers

Accelerometers measure the acceleration of a body. Displacement data can be obtained from accelerometers by double integration of the acceleration readings. Accelerometers are commonly designed using piezoelectric, piezoresistive or capacitive sensors. Conceptually, the accelerometer principle can be modelled as a mass with known weight mounted on a spring. When the accelerometer is accelerated, the mass is displaced relatively to the casing causing the spring to deform. The deformation of the spring is measured to obtain the acceleration of the body.

Accelerometers measure linear acceleration and can be assembled orthogonally to produce planar or triaxial measurements. The majority of accelerometers employ piezoelectric crystals, such as quartz. The vibrating mass deforms the piezoelectric material which produces an electrical charge proportional to the applied force. Since the weight of the seismic mass is known, the calculation of the acceleration is straightforward.

Usually, it is difficult to use deformation sensors to measure the pavement surface deflection due to the traffic load and often involves very complicated installation. The anchor of accelerometer is simple because there's no need to mount it in great depth. In addition, the cost of an accelerometer is low and decreasing. Thus, accelerometers are very promising devices that can be used in the measurement of the deflection of pavement surface. One drawback, however, is that an accelerometer can only obtain the acceleration directly rather than the deflection. In the measurement, discrete accelerometer data is obtained and a double numerical integration needs to be done to obtain the value of the deflection. The velocity and displacement can be derived from,

$$vc_{(i)} = vc_{(i-1)} + \frac{a_{(i-1)} + a_{(i)}}{2}\Delta t$$

$$dc_{(i)} = dc_{(i-1)} + \frac{vc_{(i-1)} + vc_{(i)}}{2}\Delta t$$

where $a_{(i)}$ is the acceleration value at ith sample; $vc_{(i)}$ is the calculated velocity at i-th sample; $dc_{(i)}$ is the calculated deflection at i-th sample.

Usually, the digital data comprises the so-called *baseline offset*, which could lead to unreasonable results after the integration because the high frequency component will be diminished after numerical integration. Arraigada and Partl (2009) developed a method to resolve this problem. There are two periodic functions:

- The first function: the sum of two sine with frequencies of 0.5 Hz and 10 Hz and an amplitude of 0.1 m/s^2.
- The second function: the same as the first function but adds a small constant offset.

Figure 2.1 shows these two waveforms and the results after integration and double integration.

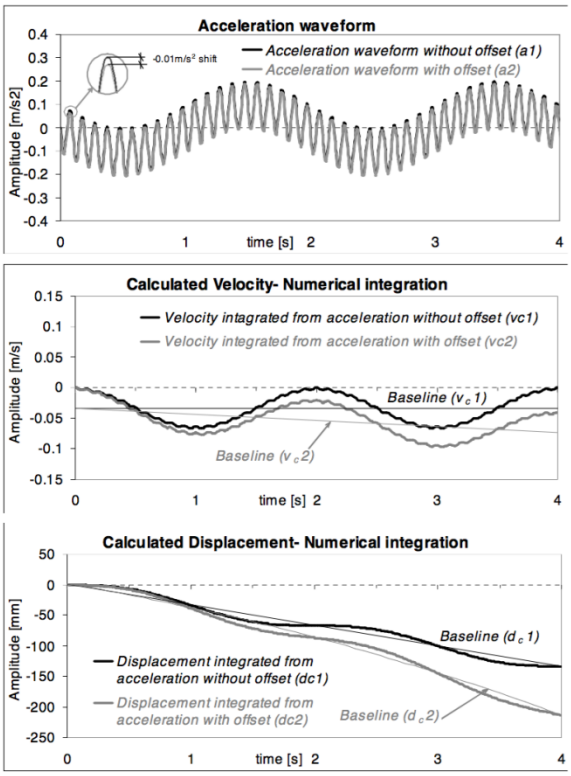

Figure 2.1 Two acceleration periodic waveforms (top); calculated velocity (middle); calculated displacement (bottom), Arraigada and Partl (2009)

The baseline of velocity and displacement present a linear drift and a quadratic drift, respectively. There is a difference of 80 mm at 4s between these two functions. This simple example clearly demonstrates that even a little constant offset error in the measured acceleration may produce a significant linear trend in the calculated velocity and a quadratic baseline error in calculated displacements. Arraigada and Partl (2009) conducted a test in the in the lab to evaluate the performance of two kinds of accelerometers: a MEMS-based model and a model from PCB PiezoTonics (http://www.pcb.com/). Both accelerometers were attached to a moving plate excited by a horizontal servo hydraulic; see Figure 2.2.

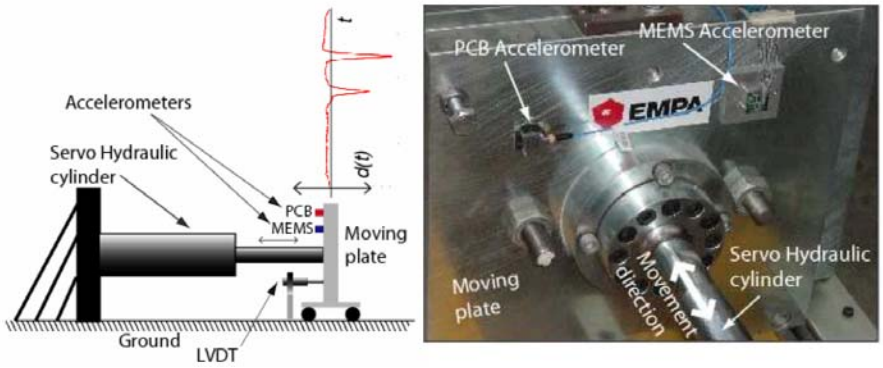

Figure 2.2 Schematic testing setup

Available deflection data collected from road measurements *d(t)* were used to simulate a passing truck. The acceleration traces for both accelerometers and the corresponding power spectrum are shown in Figure 2.3.

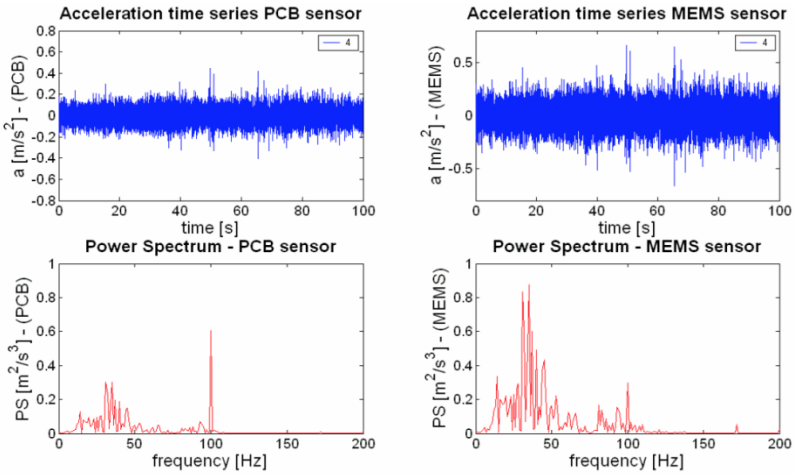

Figure 2.3 Acceleration time signals and power spectrum

The displacements can be obtained by double integration of the acceleration, which is shown in Figure 2.4.

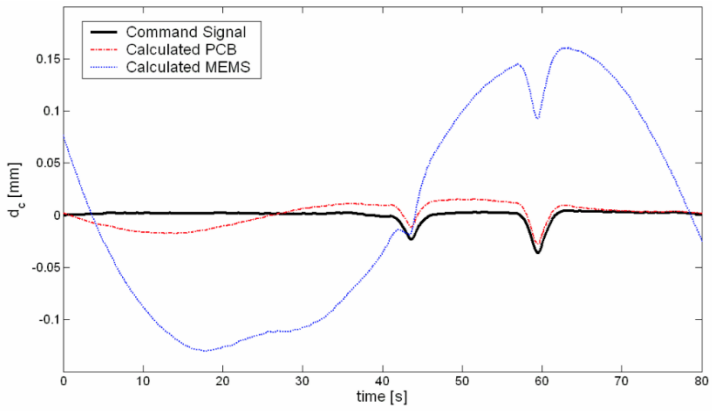

Figure 2.4 Command signal vs. displacement PCB & MEMS

Obviously, the calculated result from the PCB sensor is much better than that of MEMS. However, there is still noticeable drift from the PCB. The displacement trace is corrected using a high-order polynomial to approximate the displacement drift. First, the initial and final points for each event (tire passes of the two axle truck) are assigned. Second, the calculated displacement during these two events is replaced using a linear interpolation. Third, a high-order polynomial is used to approximate the displacement drift. Finally, the corrected displacement can be obtained by subtracting the polynomial function from the originally calculated displacement. The whole process is shown in Figure 2.5.

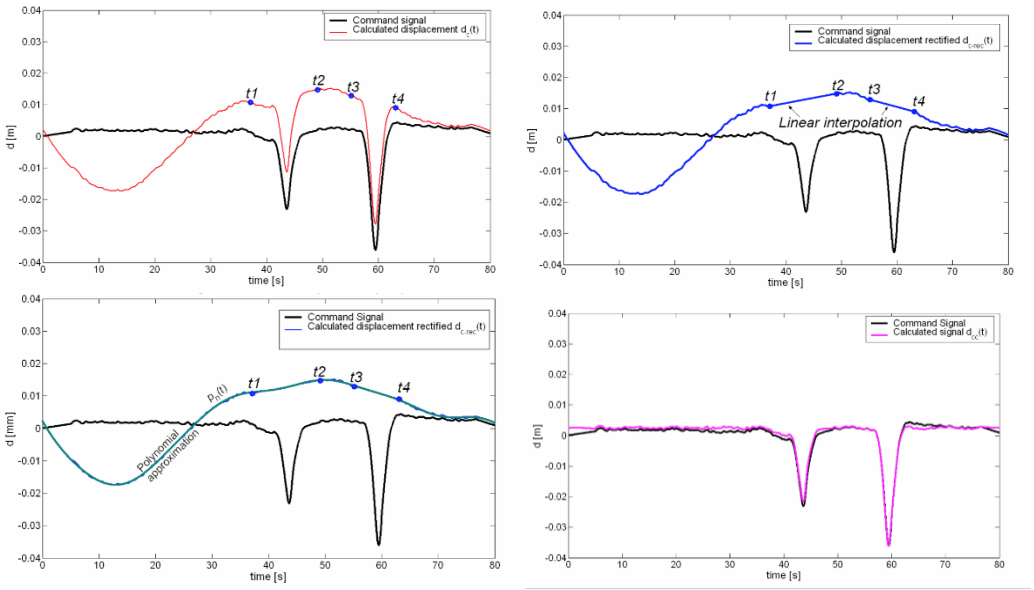

Figure 2.5 Originally calculated displacement (top-left); linear interpolate during two events (top-right); polynomial approximation (bottom-left); corrected displacement (bottom-right)

From the final drift corrected data, we can see that it is possible to reconstruct the displacement signal with quiet good accuracy.

In this method, one apparent drawback is that the initial and final points of each event need to be decided artificially which may generate error. Therefore, the next step is to remove this influence. The accelerometers were installed within different pavement structures of a specially prepared pavement on the Circular Pavement Test Track (CPTT) at EMPA (Arraigada and Partl, 2009); see Figure 2.6. In this project, there are three arms with loaded tires to simulate traffic loads and five accelerometers at five different points to measure the deflection.

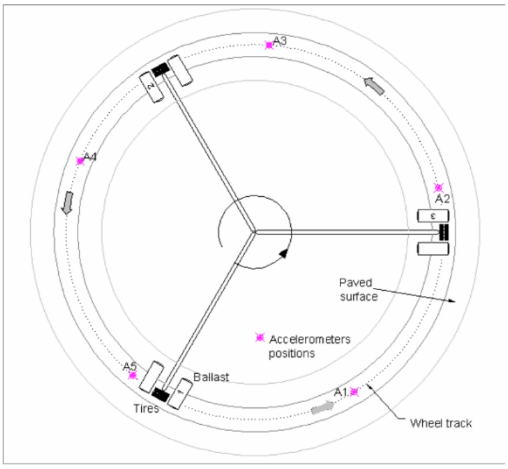

Figure 2.6 Schematic of the CPTT

An empirically developed algorithm was implemented to detect the initial and final points of each event. The algorithm is based on the calculation of sliding root mean square (RMS) using the following formula,

$$a\left(\frac{n+i}{2}\right)_{rms} = \sqrt{\frac{\sum_{i=1}^{n} a(i)^2}{n}}$$

where *a(i)* is the *i*-th sample from the acceleration waveform, and *n* is the uneven number of samples used for the calculation of the RMS. The moving time window for calculating this RMS is 0.5 s and a threshold of 0.015 m/s^2 is set. Figure 2.7 shows the example of the calculated deflection the RMS of the original acceleration signal. Figure 2.8 shows one example of the final results.

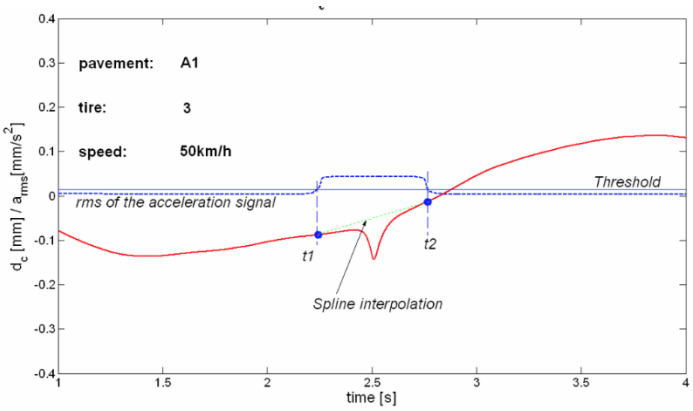

Figure 2.7 Calculation deflection and RMS of the acceleration signal

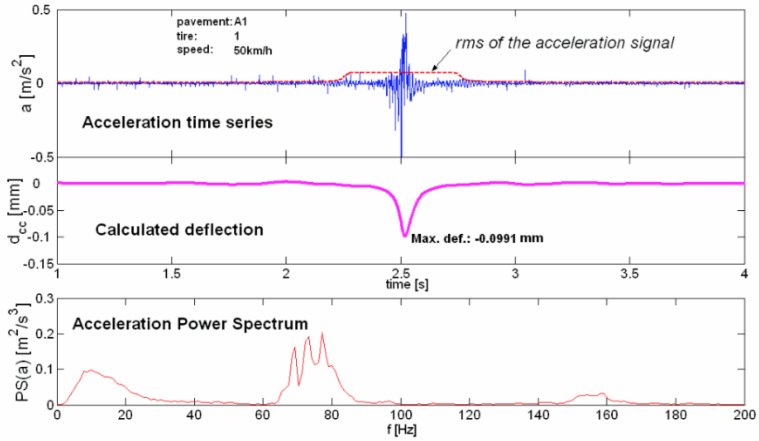

Figure 2.8 Acceleration traces and RMS of the acceleration signal (top); calculated deflection (middle); PS analysis (bottom)

Then two trials were carried out in two sites (Arraigada et al., 2009): the full-scale load simulator Circular Test Track and the A1 motorway in Switzerland. The deflection calculated from the accelerometer is compared to that from deflectometers and Finite Element models. It shows a reasonable qualitative correlation between the results from accelerometers and deflectometers. The

research shows that it's difficult for accelerometer to accurately measure low frequency motion. To date, the use of accelerometers in the pavement performance monitoring and analysis is very common. Accelerometers were used to measure the pavement surface deflection on the Jurmu test road. A four-axle truck was used to apply load. There is an additional issue that requires attention when using the accelerometer. The accelerometer readings should be equal to gravity when the pavement is not loaded. This gravity should be subtracted from the measurements to obtain the true deflection at the measured point. In principle, the gravity factor should be a constant, but the change in the third decimal changes the displacement about 10%; see Figure 2.9. Therefore, the corrections must be done individually and a single constant value cannot be used.

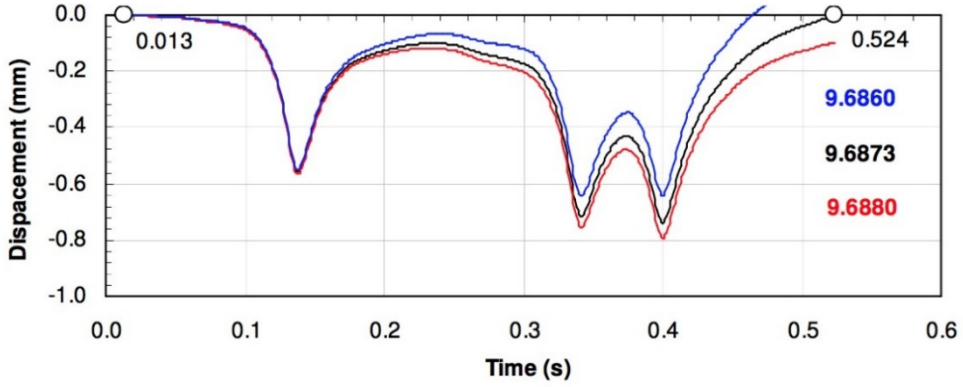

Figure 2.9 Displacements obtained from different gravity factor

Chapter 3. Load Measurement Systems

Continuous pavement deflection measurement devices typically load the pavement through the rolling axle loads that move along the pavement. The actual load may vary depending on the road surface type and the tire pressure due to the presence of dynamic loading effects. Accurate and real-time load measurement therefore becomes essential to further process the road deflection data to reliably estimate the road structural condition. Load-measurement devices are commonly used in performance evaluation of suspension systems by car manufacturers. A handful of sensor-based accurate load measurement devices are available in the market. Examples of such load measurement technologies are described below.

3.1 Multi-Axis Wheel Force Transducer

The multi-axis wheel force transducer is a one-piece sensor that is mounted between the vehicle hub and the wheel rim and reportedly delivers highly accurate load data measurement. The sensor accounts for potential temperature effects on the load measurement and water-resistance. Figure 3.1a shows an example, the PCB Series 5400. A significant limitation of this device is its cost; a three-axis system for a fully loaded truck could cost on the order of US $100,000.

Figure 3.1 Multi-axis wheel force transducer: a) PCB® Series 5400 setup; (b) transducer interface unit; (c) RoaDyn® S6XT sp System 2000

The force transducer measures six axes of force and moments on a vehicle wheel. However, the deflectometer requires only the vertical force measurement in the direction perpendicular to the road surface. This sensor consists of four major components: 1) the wheel force transducer (WFT), 2) the WFT amplifier, 3) the modified rim, and 4) hub adapter. Six individual strain gauge bridges on the WFT measure the forces and moments. The transducer interface unit (TIU) (see Figure 3.1b) handles the conversion of output signals to the forces and moments with respect to the global vehicle coordinates. One TIU is used with each WFT. The TIU processes the road load data prior to being sent to a data acquisition system. Another example of a multi-axis wheel force transducer is Kistler's RoaDyn System 2000 (see Figure 3.1c). This is specially designed for load measurement on heavy trucks and robust enough to handle off-road vehicles. The RoaDyn System 2000 is typically used for investigations into vehicle dynamics and tire testing of load data and experimental simulation. It is also mounted to the vehicle wheels and the load data can be collected into a computer using the relevant software.

3.2 Tire Pressure Measurement Sensor

Vehicle tire pressure significantly affects the loading conditions and deflection measurements, therefore, as part of this project we will investigate tire pressure monitoring technologies. The main goal will be to measure the tire pressure in real time along with the deflection and load measurements. As an example, Figure 3.2 shows the Doran 360HD tire pressure sensor that continuously monitor tire pressure and temperature data received through radio frequency signals transmitted from wireless sensors that are mounted in place of the valve stem caps in each tire.

Figure 3.2 Doran 360HD tire pressure sensors

3.3 Preliminary Evaluation of Contact-Based Sensors

Preliminary study was undertaken to evaluate whether contact-based motion sensors, such as accelerometers or geophones, can reliably detect pavement deflection induced by typical tire loading. Contact-based motion sensors include those that must be placed on a moving surface:

- **LVDTs** – these devices have a shaft with a tip that directly contacts with a surface. Highly sensitive LVDTs are available for measuring a range of displacements of interest; however, using an LVDT would require placing the tip/shaft on the surface, establishing a datum, making a measurement over the period of deflection, and then removing the LVDT. This approach is not compatible with desired use of a moving sensor platform. For this reason, the LVDT is primarily of value as a laboratory and field reference device.
- **Geophone** – a geophone is a velocity-sensing device in which a voltage is generated from sensing coils used to detect moving magnetic elements. In a geophone device, the magnetic element motion is induced when the geophone contacts with a moving surface. Geophones have the advantage of being self-generating, meaning that the motion induces an output signal and no power supply is needed. Typical sensitivity on commercially available geophones is about 28 V/(m/s).
- **Seismic accelerometers** – seismic accelerometers are used to measure very low-level accelerations. Using integrated signal conditioning and amplification, these sensors have sensitivities of about 10 V/g.

In this early assessment of contact-based sensors, the goal was to determine whether geophones and seismic accelerometers can provide a reasonable measurement of expected deflection levels. This requires one stage of numerical integration of a geophone signal and two integrations of the signal from an accelerometer. There are practical issues in detecting displacement in this manner. To begin with, the signal levels for expected pavement deflections will be at the lower region of operating range for these devices. The expected peak deflections are

assumed to range from 50 to 100 microns up to 1 to 2 mm. This means that both vibrational and electrical noise will play a large role in how accurately displacement can be estimated from measured signals. To begin understanding these issues, preliminary work focused on testing with a seismic accelerometer. Results from testing with geophones will require follow up investigations.

This preliminary report describes how a simple deflecting surface model is used to estimate the range of expected velocity and acceleration levels. These estimates provide requirements that must be met by commercially available sensors. Results from preliminary laboratory testing with a selected seismic accelerometer are shown to reliably detect an acceleration pulse of the type that might be expected during pavement deflection. Measured data was used to demonstrate the challenges in estimating both velocity and displacement from measured acceleration.

Chapter 4. Model to Estimate Expected Acceleration Levels

A seismic sensor placed on a dynamically deflecting pavement will detect velocity or acceleration, depending on the type of sensing mechanism used. A geophone is sensitive to velocity while an accelerometer provides a measure of the acceleration. The sensitivity, noise properties, bandwidth, and other key specifications for these devices will determine how well each can be used in a given application, and the problem for measuring displacement has certain unique issues as well.

Motion signals were simulated by considering a sensor placed on a surface that deflects due to a passing moving tire load. An approximate smooth pulsed deflection bowl with a spatial length Lt is assumed to move at constant velocity *V* past a surface-mounted sensor. The vertical velocity at the sensor location is estimated by $vz = (dz/dx)\, V$, where *z* is the vertical deflection and *x* is the position of the moving load (or along the bowl). Acceleration (*az*) in the vertical direction is then estimated by a simple numerical derivative of *vz*.

As an example, a deflection bowl with a peak of 100 microns with length 3 m is used to simulate typical surface motions. If the load is moving at a constant speed of 5 mph, the peak velocity and acceleration are found to be about 0.5 mm/s and 0.95 mg. This would result in peak voltage signals in the range of 10 to 20 millivolts, since sensitivities of 30 V/(m/s) and 10 V/g can be expected for typical geophones and accelerometers, respectively. Plots of simulated signals are shown in Figure 4.1. The simulated voltage signals are deemed measurable using modern data acquisition hardware; however, the influence of electrical and vibrational noise must be considered.

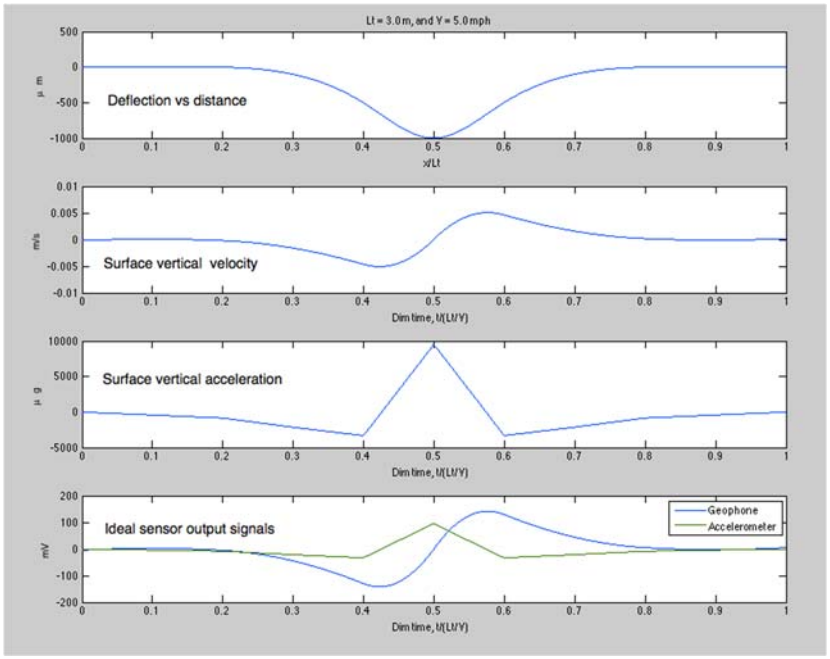

Figure 4.1 Simulated deflection bowl of length *Lt* = 3m.
For a moving load at 5 mph, the lower plots show velocity and acceleration, with the lowest plot comparing expected voltage signals for typical commercially available geophone and accelerometer sensors.

For larger deflections at the same speed, such as a 1-mm deflection, the geophone and accelerometer peak values increase by about a factor of 10. These preliminary calculations provide sufficient confidence in acquiring these sensors for lab testing.

4.1 Seismic Sensor Selection

During the initial phase of this project, research was conducted into viable accelerometers and geophones for use in estimating pavement deflection. The preliminary estimates of expected velocity and acceleration levels (e.g., as illustrated in Figure 4.1) were used to narrow the focus to low-noise seismic accelerometers. Geophones were also investigated, but this initial study has focused on the evaluation of highly sensitive accelerometers.

The most sensitive commercially available seismic accelerometers have sensitivity of about 10 V/g. These IEPE (piezo electric with integrated electronics) accelerometers have very low noise. Using the simulation described earlier, it was found that viable sensors would generate electrical signals ranging from 10 to 200 millivolts, which are low but detectable levels, and sufficiently above expected electrical noise values.

Preliminary work focused on evaluating two different seismic accelerometers: a) Wilcoxon 731A, and b) PCB 393B31. These fully calibrated devices have specified equivalent noise levels in the neighborhood of 0.01 to 0.5 mg/sqrt(Hz) across the frequency range of interest. This 'noise floor' level and the high sensitivity (~10 V/g) place these seismic accelerometers well above any other devices. The Wilcoxon 731A, shown in Figure 4.2 is similar in size and form to the PCB 393B31.

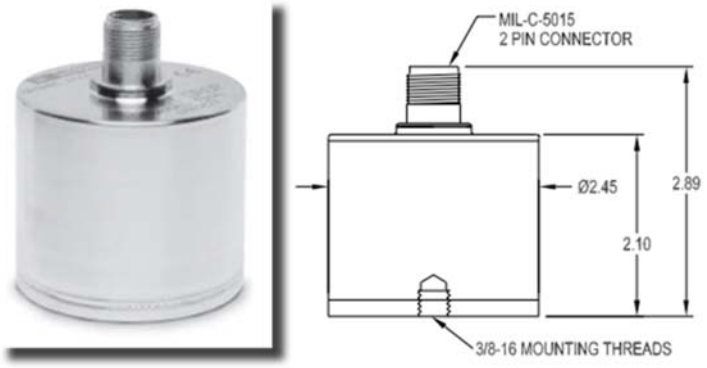

Figure 4.2 The Wilcoxon 731A seismic accelerometer

Geophones sensing elements can provide velocity sensing with a sensitivity of about 30 V/(m/s), and as illustrated in Figure 4.1 ideally this sensor could also provide deflection sensing capability.

4.2 Laboratory Benchtop Assessment of Low-G Seismic Accelerometers

A bench test was set up to evaluate how well a Wilcoxon 731A (Wilcoxon Research, Inc., Germantown, MD) seismic accelerometer can detect low level displacement, and to assess the signal quality at low level vibration.

The test surface was a cantilevered aluminum beam with some stiff foam adding damping, acting like an elastic foundation. Light taps on the beam or the foam induces motion that can be

detected by both the accelerometer and a reference point-laser displacement sensor (Model IL-030, Keyence, Inc.). Note that an IL-030 laser displacement sensor that measures displacement directly was used to monitor the accelerometer motion as well.

Programmed acquisition and analysis of sensor signals was made using a program in LabVIEW (National Instruments, Inc., Austin, TX). The program controls signal acquisition and test signals from this accelerometer were evaluated. To illustrate the low g detection and noise levels, the accelerometer was used to pick up ambient vibration (about 2000 micro-g peak) on the test bench. Test signals are shown in Figure 4.3, and spectral analysis (Figure 4.4) shows about a 20 Hz dominant vibration mode, likely coming into the test setup from the building.

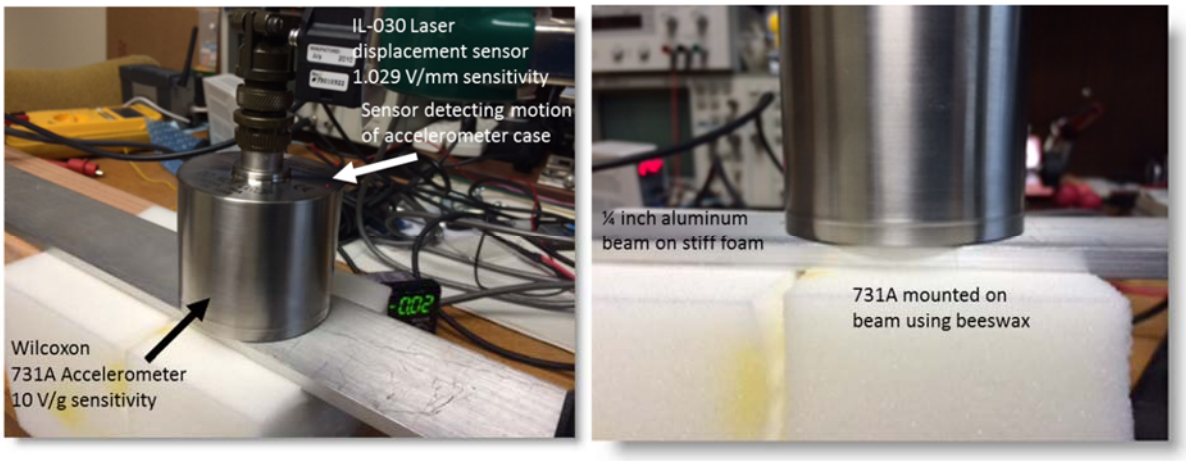

Figure 4.3 Bench test setup of a Wilcoxon 731A IEPE seismic accelerometer

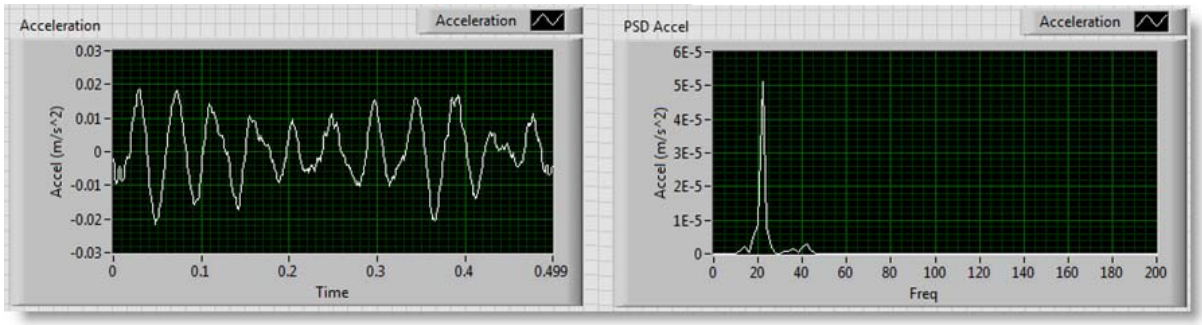

Figure 4.4 Ambient vibrational noise detected by Wilcoxon 731A sitting on test bench

To illustrate the ability of this sensor to pick up low level acceleration as expected from deflected pavement, a simple test was devised using this bench test. As shown in the left photo in Figure 4.5, a small displacement induced in the foam support was sufficient to induce response in the beam on the order of 50 to 100 microns peak displacement. This motion is simultaneously measured by the laser sensor and by the accelerometer.

Some preliminary algorithms for integration of the acceleration signal (twice) to estimate displacement have been tested. On the graph in Figure 4.5, the red line is the output from the laser sensor while the white is the displacement estimated by double-integration of the acceleration signal. These results show that a reasonable displacement measurement can be derived from the accelerometer. It is clear that the electrical noise is very low for these sensors. It is expected,

however, that in a field deployment there will be external vibrational noise that may corrupt the pure deflection signals.

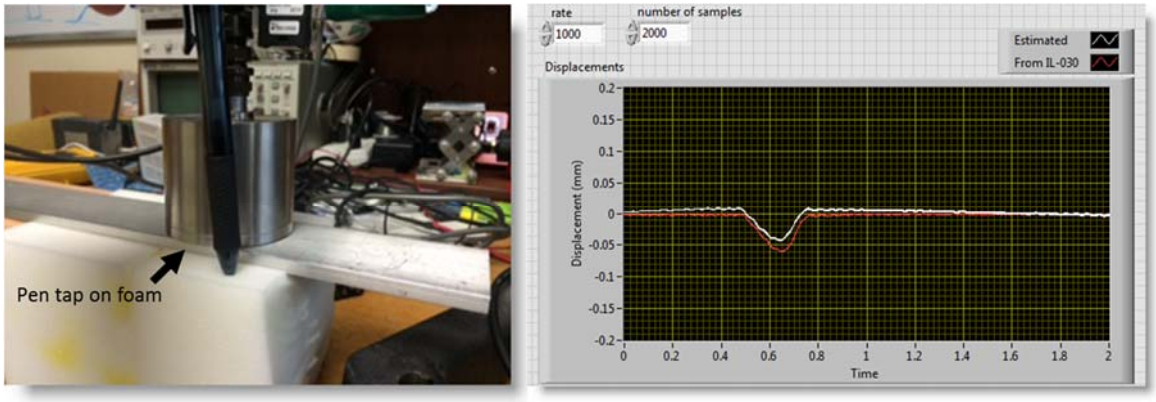

Figure 4.5 Inducing a test pulse deflection that is simultaneously measured using a Keyence IL-030 laser displacement sensor and a Wilcoxon 731A seismic accelerometer. The signal comparison on the right shown the doubly integrated acceleration (white) provides a fairly accurate estimate of the displacement measurement from the laser sensor (red). The peak value is about 50 microns.

Chapter 5. Estimation of Deflection Bowl Using High Precision Lasers

5.1 Basic Principle

This project investigated high performance lasers for monitoring the deflection caused by a truck driving on a road. The sensing principle is driven by physical considerations of the system, outlined below:

- The system must contain at least two distance measurement lasers—one laser monitors the undeflected pavement surface, while the second monitors the deflection caused by the truck.
- While modern distance measurement lasers have a very high accuracy, no currently available technology can determine the absolute position of a system (such as a laser) with respect to some inertial frame of reference, with the required precision (0.1 mm or less), and during the minimal time required by both lasers to cover the deflection bowl. Assuming a truck velocity of 20 m/s (45 mph), the position of both lasers would have to be known in an inertial frame of reference for at least 0.25s, with 0.1 mm accuracy.
- The above considerations mandate some sort of physical coupling between both sensors, in order to reduce the degrees of freedom of the system, and the addition of other sensors to estimate such degrees of freedom. The absence of coupling between sensors would lead to a position estimation problem that could not be theoretically solved

One of the simplest mechanical coupling approaches is use of a structural beam that would be rigid enough to only have six degrees of freedom (that is, three degrees of freedom in translation and three degrees of freedom in rotation). This assumption is valid only if the beam can be considered a rigid body—that is, if the distance between two points of the beam remains constant at any single time. In practice, we can tolerate changes in distances that do not exceed a fraction of the required accuracy, which is a fraction of < 0.1mm. The spatial scale of the deflection bowl defines the required length of the beam, which should be on the order of 5 meters. Thus, the CTR research team created a laser sensor system using a structural beam as the basis.

The setup is outlined in Figure 5.1. This setup contains a beam suspended from a trailer, on which the distance-measuring lasers are attached with this configuration:

- One laser monitors the pavement far away from the deflection bowl (Laser 1)
- A secondary laser monitors the pavement immediately after Laser 1, to estimate the position of the beam with respect to the ground (Laser 2)
- The third laser monitors the deflection bowl itself (Laser 3)

5.2 Laser Characteristics

Given the uneven texture of the pavement, a point distance measurement would be associated with a significant uncertainty, on the order of a few millimeters or centimeters. Therefore, measurements have to be taken using at least a 1D line scanner that can monitor a large

number of points in the transverse direction, to identify features that can be used by all lasers to obtain an absolute distance measurement.

The 1D line scanner has the additional advantage of matching the horizontal positions through their transverse scan patterns. This is extremely important in practice, since we have to precisely estimate when Lasers 1, 2, and 3 are above the same exact point in space. This could not be achieved with a point laser since the truck is not expected to drive on a straight line with deviations less than the laser spot size (a fraction of a millimeter).

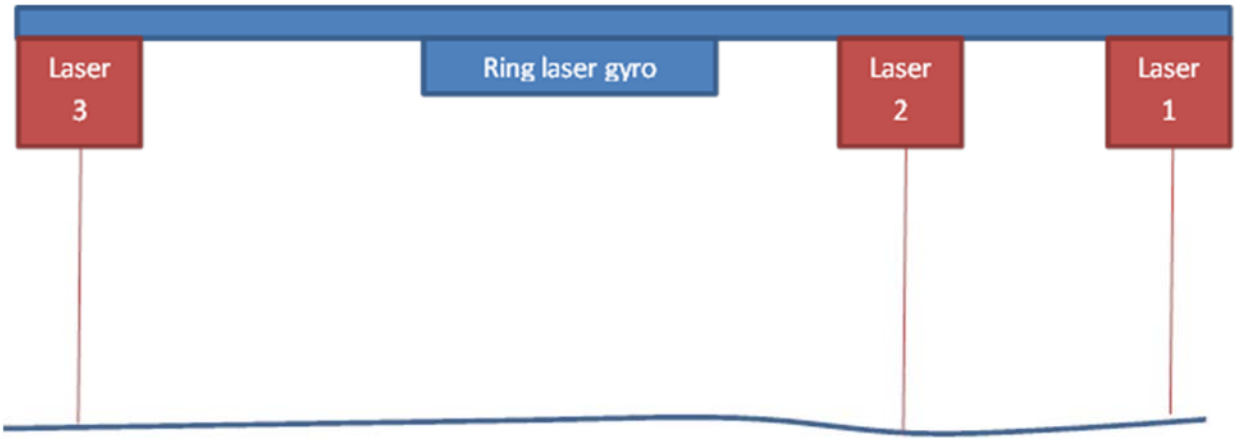

Note that this system allows only the maximal deflection to be measured. In practice, more lasers can be added between Laser 2 and Laser 3, to obtain intermediate measurements of the deflection bowl.

Figure 5.1 Proposed setup

The horizontal positions will be matched using algorithms such as cross-correlation, run on the transverse laser scans. A model of the truck velocity can be useful to speed up the search across the various transverse scans. Since cross-correlation functions can be computed very quickly, we expect that this position matching will not be an issue in practice, though this will require powerful embedded computers, given the very high data rate (megabits per second).

5.3 Data Processing

As a rigid body confined to a 1D environment, the beam has theoretically only two degrees of freedom: a degree of freedom in translation, and a degree of freedom in rotation. These can be represented using the following variables:

- The vertical position of the center of gravity of the beam
- The angle of the beam with respect to a direction of reference (which we will refer to as "pitch angle")

In the three-laser setup described above, the measurement data only allows us to estimate one of these variables—either the pitch angle or the vertical position of the center of gravity of the beam. The displacement measurements (d) from the various lasers can be modeled as a delay system:

$$d2(t+T) = d1(t) + f[p(t+T)-p(t), z(t+T)-z(t)]$$

where *d2(t+T)* represents the measurement of Laser 2 at time *t+T*, *d1(t)* represents the displacement measurement of Laser 1 at time *t*, *p(t+T)* and *p(t)* respectively correspond to the pitch angle of the beam at times *t+T* and *t*. The vertical position of the center of gravity of the beam (with respect to a fixed inertial frame of reference) is *z(t+T)* and *z(t)* at times *t+T* and *t* respectively. By "stacking up" streaming measurement data and performing regression, one obtains a system of *n*-equations and two variables (*n* is the number of measurements considered in the regression). While this system is overdetermined, it can unfortunately not be solved since the corresponding matrix is rank deficient (rank 1 instead of 2). Therefore, one cannot independently estimate what *p(t+T)* and *z(t+T)* are in function of *z(t)* and *p(t)* respectively.

5.4 Ring Laser Gyrometer

To address this theoretical issue, we need additional sensors to be placed on the beam, to estimate some of its state variables. The two possible sensor candidates are:

- An accelerometer, to estimate the absolute vertical position of the beam
- A gyrometer (or gyroscope), to estimate the pitch angle of the beam

The application requirements make the accelerometer a complex solution. In order to estimate the absolute position of the beam with an accelerometer, one would need to build a model of the suspensions of the beam, the suspensions of the truck, and the road itself. This model would likely have residual errors far above the required fraction of 0.1 mm.

In contrast, a high precision gyrometer could theoretically be used to estimate the pitch angle of the beam, with respect to an inertial frame of reference. The most accurate gyrometers available are known as "ring laser gyros", and are commonly used for high precision aerospace applications, for example in the inertial measurement units of commercial airliners (Airbus A320 and Boeing 777) or missiles. These devices measure the absolute attitude of an object with respect to an inertial frame of reference, that is, a frame aligned with distant stars that are assumed to be fixed. In the present case, the ring laser gyro that we intend to use for this application (Honeywell GG1320) has the specifications shown in Figure 5.2.

Size	Height 1.77" (4.5 cm) Diameter 3.45" (8.8 cm)
Weight	1 lb. (454 grams)
Start-Up Time	1 second (typical)
Shock (Op & Non-Op) (See below)	22 g, half sine, 11 millisecond
Temperature Range • -65°F to +185°F (Operating) -54°C to 85°C • -65°F to +200°F (Non-Operating) -54°C to 93.3°C	
Power	15 Vdc, 1.6 Watts nominal 5 Vdc, 0.375 Watts nominal
Interface	RS-422, 25 pin micro "D" Asynchronous, 1 MHz, 8 Bit
Bias Stability • 0.0035 deg/hr (typical)	
Angular Random Walk (ARW) • 0.0035 deg/root-hour (typical)	
Magnetic Environment, Operating: 0.002°/hr/gauss	
Altitude, Operating	-20,000 ft. to +80,000 ft. (-610 m to +21,336 m)
Scale Factor – Corrected • Linearity • 30-day Stability	1,164,352 ±18 pulses/rev. 5.0 ppm of full scale 5.0 ppm rms
Sample Frequency Latency	2,000 Hz (typical use) 5,000 Hz (maximum) 168 micro-seconds
Rate Input	900 deg/ sec (maximum)

Figure 5.2 Ring laser gyrometer and basic specifications

Unlike other gyrometers (such as MEMS gyrometers used in smartphones), a ring laser gyro is very accurate, to the point of having a typical error on the order of 0.003 degree per hour of integration. This extreme accuracy allows one to precisely estimate the change in pitch attitude of the beam over long time intervals, in an inertial frame of reference.

Our objective is to estimate the difference of the pitch attitude of the beam, that is $(t+T)-p(t)=\int_t^{t+T}\omega(\tau)d\tau$, where ω(τ) is the rotation rate of the beam along an horizontal axis, as measured by the ring laser gyrometer. Note that modern ring laser gyrometers such as the GG1320 have an onboard integrator and provide the value of *p(t+T)-p(t)* directly.

To estimate the error in pitch attitude over the time interval [*t*, *t*+*T*], we use the datasheet specification of error random walk of 0.0035°/√h. For a truck velocity of 5 meter per second (about 10 mph), this implies a total error of 0.0035°/√3600, over the one second of integration time; that is, an error of about α=0.00005°. This error in attitude estimation will be reduced for higher truck speeds, and increased for lower truck speeds. This error will cause an uncertainty in distance measurement of Lsin(α)=0.004 mm, which is comparable to the error.

Note that this derivation was done assuming that the earth frame was an inertial frame of reference. Since the rotation rate of the earth is 15°/h, this rotation implies a change of the orientation of the earth frame of 0.004° over one second, considerably more than the 0.00005° error of the ring laser gyro. This earth rotation effect causes an uncertainty on the order of 0.24 mm over one second, which is unacceptably high (our target measurement accuracy is less than

0.1 mm). To address this issue, we need to estimate the component of the earth rotation vector on the axis of the gyrometer. This component is a function of the attitude of the beam. One possibility is to equip the beam with a set of multiple gyrometers, which allow one to compute its attitude, and cancel the projection of the earth rotation vector on the horizontal axis of the beam. Another possibility could be to use a lower quality inertial measurement unit coupled with the GPS to estimate the attitude of the beam with respect to the ground frame.

The rotation of the earth around the sun yields a negligible drift, on the order of the intrinsic drift of the gyrometer, which should cause an error lower than 0.004 mm. Hence, a geocentric frame is sufficiently accurate to describe the system.

Using the above-described ring laser gyro, we can estimate $p(t+T)-p(t)$, which allows us to solve for $z(t+T)-z(t)$, since $d2(t+T)=d1(t)+f(p(t+T)-p(t),z(t+T)-z(t))$, where the function f is one to one. Hence, the first two lasers combined with the ring laser gyrometer allow us to compute the attitude of the beam $p(t)$ and the vertical position of the center of gravity $z(t)$ at all times. The error in the estimation of $z(t)$ should be on the order of the intrinsic accuracy of the laser distance sensors. This may be further reduced in practice by exploiting the error properties of these sensors, taking advantage of the fact that the distance measurement sampling rate is much higher than the cutoff frequency of the mechanical system (beam and suspension).

5.5 Measurement Principle

Once the values of $p(t)$ and $z(t)$ are known at all times, one can compute the position of all laser sensors at all times (with respect to a fixed inertial frame of reference). This allows up to correct the laser measurements from sensors 1 and 3 (or equivalently sensors 2 and 3), and compute the actual vertical position of the pavement before (sensors 1 or 2) and after deflection (sensor 3) in the inertial frame of reference.

5.6 Limitations of the Rigid Body Assumption

One of the most important assumptions used in this approach is the modeling of the beam as a rigid body. To check if this assumption would be realistic, we evaluated the flex caused by a static gravitational field to the beam, under various scenarios. While this gives us an idea of the possible deviations of the beam from the rigid body model, a full analysis should be conducted in a dynamic loading setup (in which the truck mounts are excited by some random vibrations) to precisely compute the effect of the vibrations on the rigid body assumptions.

Preliminary computations assuming a beam 5 meters long, 0.7 m high, and 0.2 m wide made of carbon fiber epoxy (the material that has the highest strength to weight ratio), the static flex would be on the order of 0.05 mm, for a thickness of 1 in. The total weight of such a structure is about 600 kg. We can see that this figure is close to the required accuracy, though this represents a static flex in the earth gravitational field that creates a systematic bias which can be corrected. The most important factor is the dynamic flex caused by the time varying loading from the beam mounts, attached to the truck trailer.

To evaluate their effect, we are currently developing a simulation framework on MATLAB to understand the amplitude of the dynamic (time varying) twisting and warping of the beam, under realistic assumption. The amplitude of these motions will be an important factor for the implementation of this system. If the amplitude exceeds the required 0.1mm accuracy, alternative computational methods will have to be found.

If this need arises, one possible method would be to estimate the warping and twisting in real time, using accelerometers, strain gauges and similar devices mounted on the beam. The main issue with this type of solution is that it would cause additional measurement errors in comparison with a regular steel beam. An example of simulation is shown in Figure 5.3.

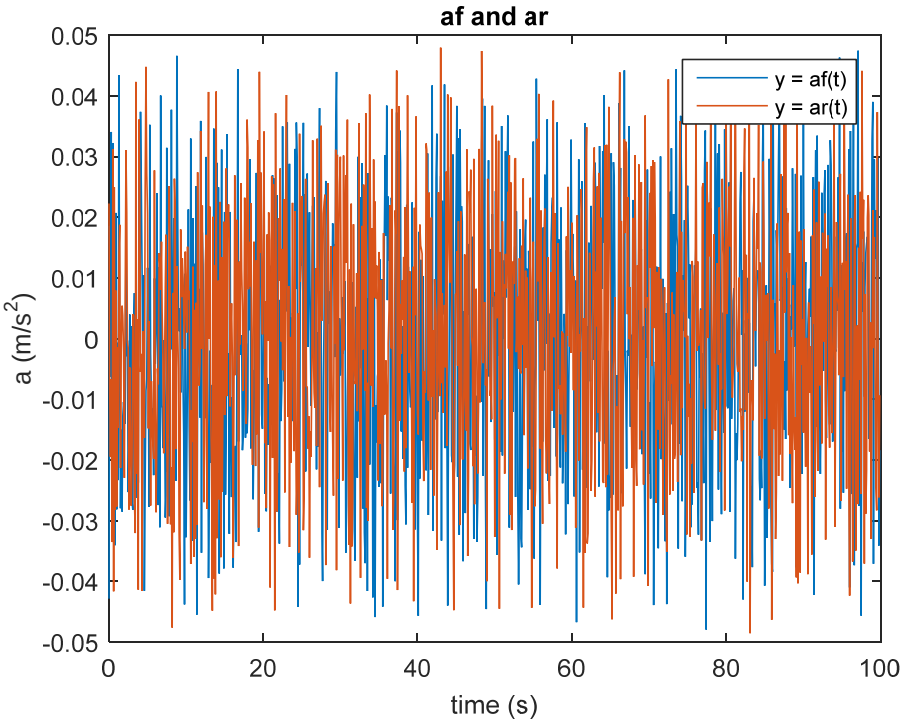

Figure 5.3 Simulation of acceleration measurements

Chapter 6. Lab Testing: Laser System Development

This project developed a laser sensor system based on several sensors mounted on a rigid beam. When the truck moves along the pavement, the laser sensors collect data and we can use the data to calculate the pavement surface deflection. To reach that point, the first problem we needed to solve was how to match the data from different sensors. For simplicity, only two laser sensors were used initially. A simple sensor system was developed for the preliminary lab tests, as shown in Figure 6.1. Two laser sensors were mounted on both ends of a hollow aluminum beam. Then, these lasers were connected to a controller and a laptop used to acquire the data. To perform the in-situ experiment, all of this equipment was placed on a wheeled three-shelf cart.

Figure 6.1 Setup of the initial laser system

6.1 Laser Sensors

Two ultra-long range 3D LJ-V7300 laser sensors developed by Keyence were used. The reference distance of this sensor model is 300 mm. The z-axis (height) measurement range is ±145mm. The X-axis widths are 110 mm, 180 mm, and 240 mm at the near side, middle, and far side respectively (see Figure 6.2).

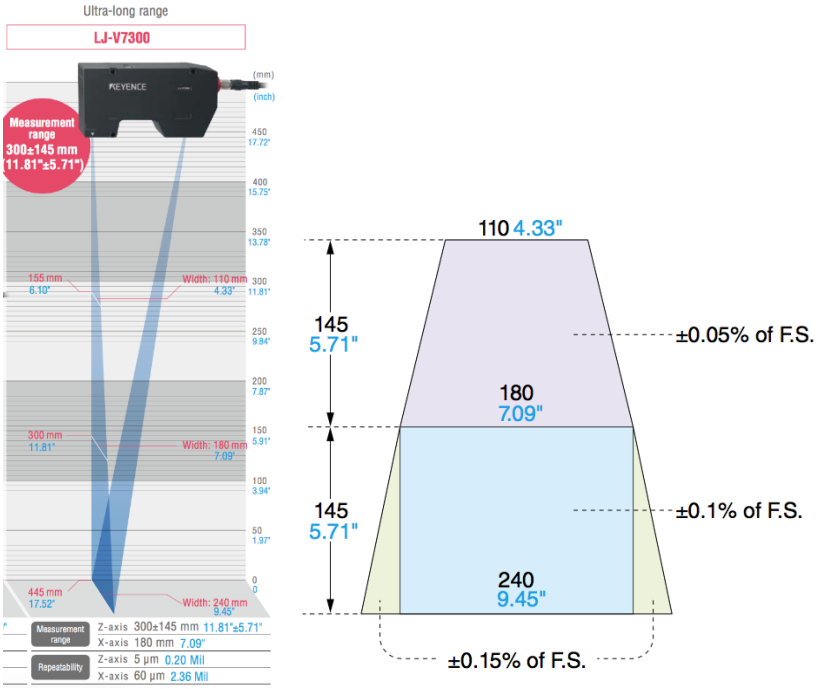

Figure 6.2 The measurement range of LJ-V7300 laser sensor

6.2 Controller and Power Source

A LJ-V7001P controller and a CV-U3 power source were used (shown in Figure 6.3).

Figure 6.3 Controller (left) and power source (right)

At most two laser sensor heads can be connected to this controller, which is connected to a laptop by a USB cable. The controller should be powered by the right source. The rated input voltage and current of the power source are 100 to 240 VAC (50/60 Hz), and 2.1 A maximum, respectively. The rated output voltage and current are 24VDC and 6.0 A, respectively. A CP1500AVRLCD UPS battery was used to power this system.

6.3 Software

The software LJ-Navigator was used to monitor the measurement and acquire the data. Within this software, we can change the measurement range, frequency, and so on as needed.

6.4 Beam, Battery, and Cart

The two laser sensors were mounted on the ends of a rectangular aluminum hollow beam at a 45-degree angle. Table 6.1 shows the beam dimensions.

Table 6.1: Beam dimensions

Dimension Name	Value (inch)
Length	60
Height	8
Width	4
Wall	0.25
Internal Height	3.5
Internal Width	7.5

For the in-situ experiment, a plastic, wheeled, three-level cart was used to hold all the equipment (it can support 200 pounds). The cart weighs 2.2 pounds and the length, width, and height are 33.6 inches, 18.6 inches, and 37.8 inches, respectively.

The research team built this initial system and conducted the lab experiments. Some data was obtained for analysis, which is described in the next chapter.

Chapter 7. Simulation of the Beam Response with Truck-Like Loading

This chapter provides the results of the laboratory testing conducted with the initial cart-based system. We used the modelling software COMSOL to simulate how the beam deforms after loading the laser sensors. The simulation is conducted using the multibody dynamics package in COMSOL.

As the simulation results indicate (see Figure 7.1), the total displacement at any point of the beam (with respect to its non-deformed shape) is on the order of 2 micrometers, with 1g loading (i.e., with the beam static, in the field of gravity). Since the vertical acceleration in a truck is at most 2–3 g units, we expect that the worst case deformation of any point in the beam will be about 6 micrometers, which is compatible with the accuracy required for the deflection measurement experiment (100 micrometers).

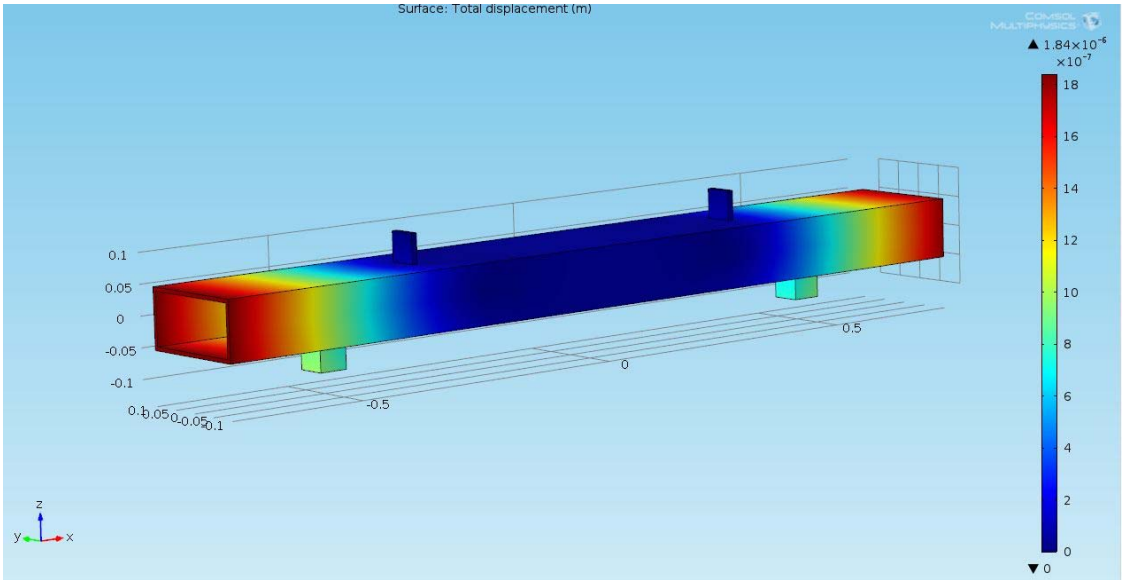

Figure 7.1 Deformation of the beam, as attached to a truck, in the field of gravity. Maximum deflection is 2 micrometers (less than 1 micrometer at the position of the laser heads), which is within our requirements.

7.1 Lab Testing of the Laser Sensors

We evaluated the performance of the laser sensors in the lab (as covered in Chapter 6) before testing them on an actual road setup (which is covered in Chapter 8). The objective of this testing was to determine the actual performance of the laser heads, with respect to the specifications of the manufacturer.

7.2 Laser Sensor Calibration

In this experiment, we mounted the lasers at a 45-degree angle with respect to the beam in order to evaluate the possibility of using the fan laser beam for determining the roll angle of the beam (this was later shown to lead to an uncertainty that is not compatible with deflection

measurements). In practice, the pitch attitude of the beam will be measured by a ring laser gyro, which is much more accurate. Figure 7.2 illustrates the sensor placement calculation.

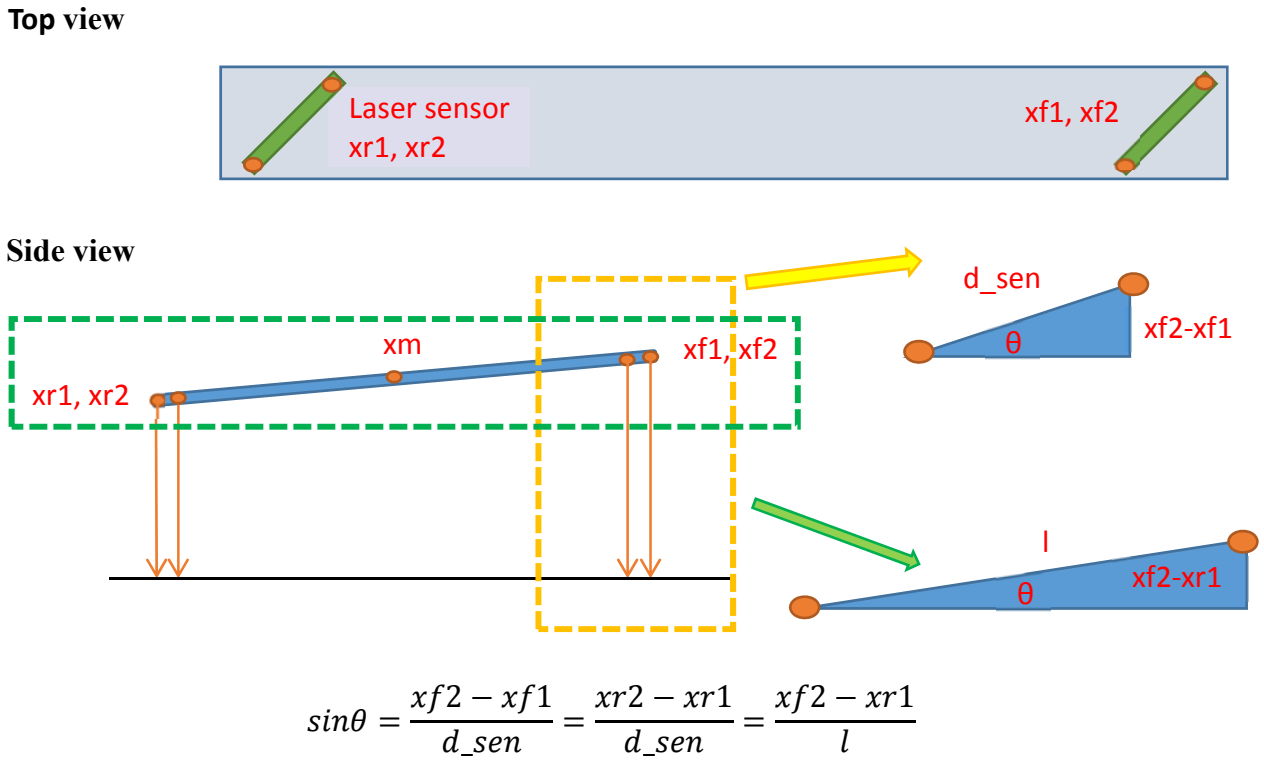

$$sin\theta = \frac{xf2 - xf1}{d\_sen} = \frac{xr2 - xr1}{d\_sen} = \frac{xf2 - xr1}{l}$$

Figure 7.2 Top view and side view of the mounted laser sensor.
By calculating the height measured (xr, xf), we can calculate the elevation angle from the equation, and compare that with the angle calculated from MATLAB simulation.

We first conducted a static test of the sensors: the sensors were attached to a rigid rectangular aluminum beam (2 m long, 5 mm thick) and set up to monitor a static object. The static test allowed us to understand the dispersion of the measurements generated by both laser heads, and identify any systematic errors, including time-varying systematic errors (which could be related to heating inside the sensor, imperfect calibration of the lasers or of the optics, or mechanical defects).

The results of this static experiment are outlined in Figure 7.3.

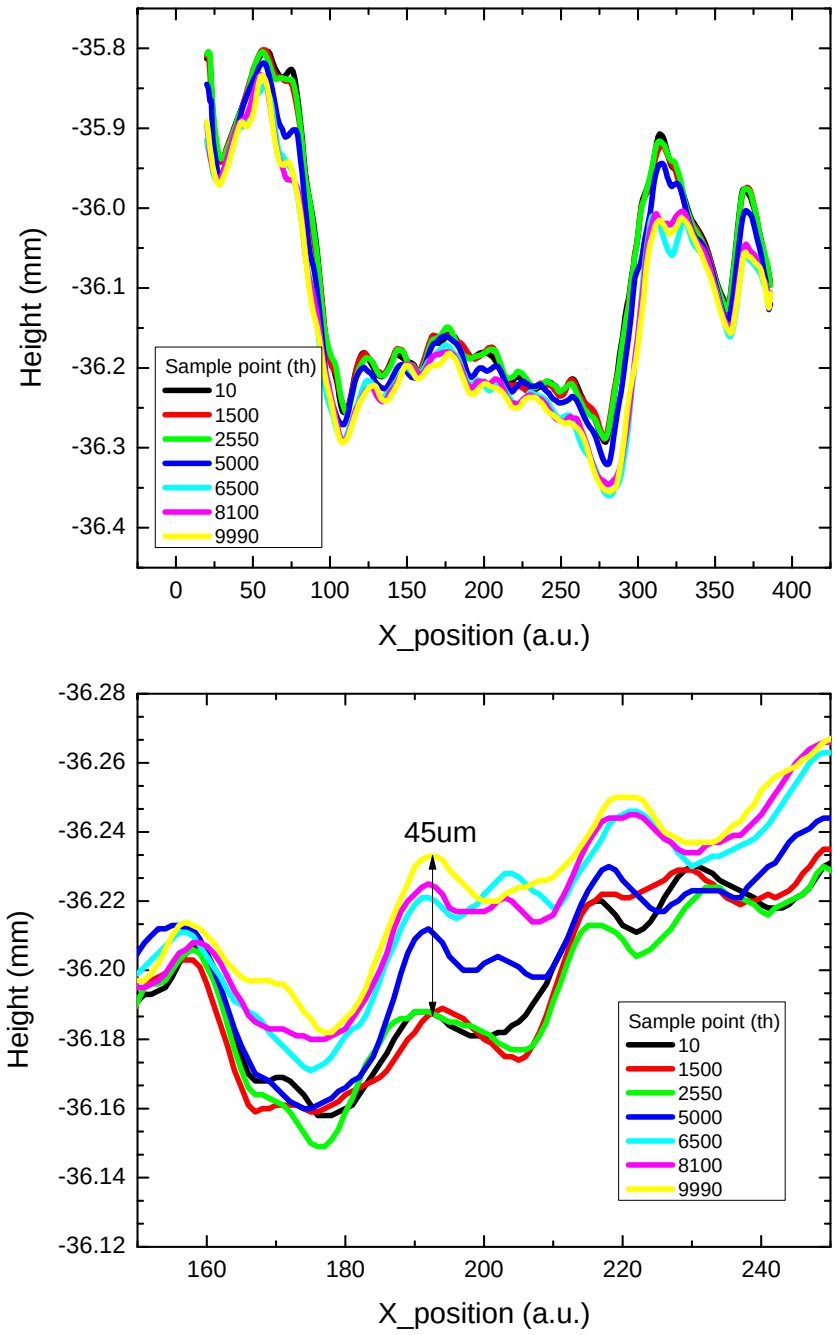

Figure 7.3 Static profile measurement from the laser sensor.
As shown, the measurements evolve over time, and have approximately a 45-micrometer worst-case error.

To determine the type of error generated by the sensor, we plotted the distribution of the errors for various points along the scanline (see Figure 7.4).

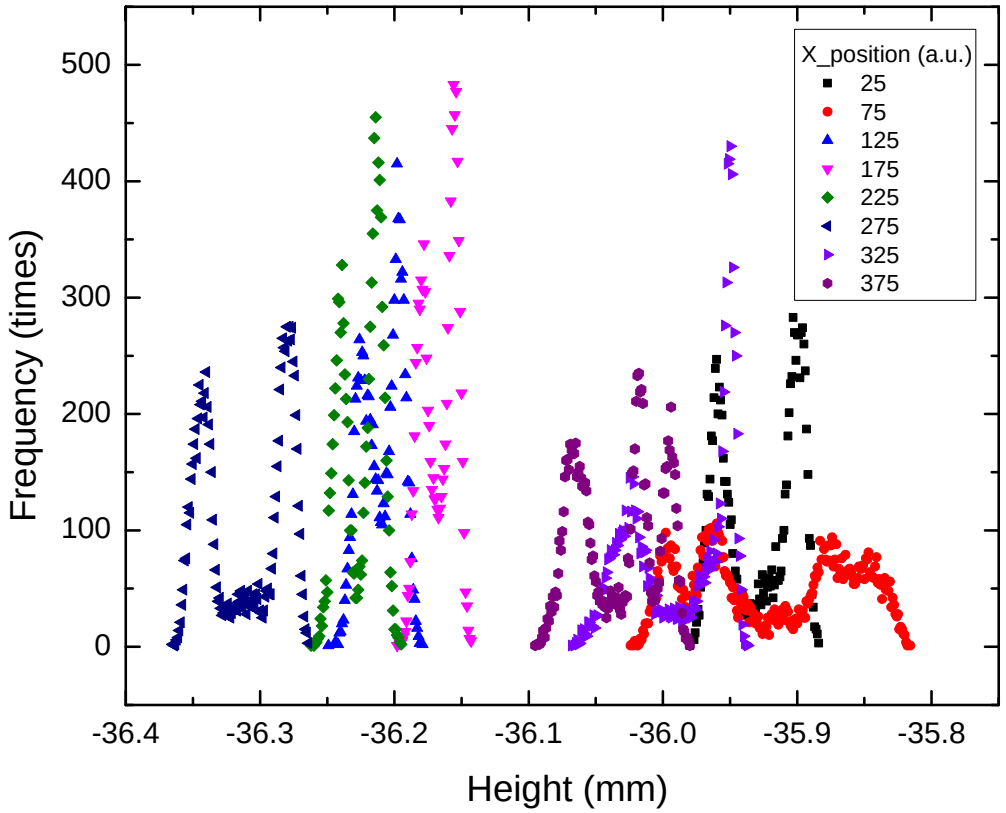

Figure 7.4 Bimodal distribution plots

The Figure 7.4 plot shows that the error distribution is bimodal. We traced this effect to a switching that occurs internally in the sensor. Indeed, if we plot the same data, but select only time steps corresponding to an even or an odd integer, the error distribution clearly shows two Gaussian modes, with some separation. The uncertainty associated with each Gaussian mode is on the order of 15 micrometers, with a total separation on the order of 50 micrometers.

Hence, we can very simply select only half of the data points to obtain a precise position reference. The Gaussian error model is an excellent fit for the data, as shown in Figure 7.5.

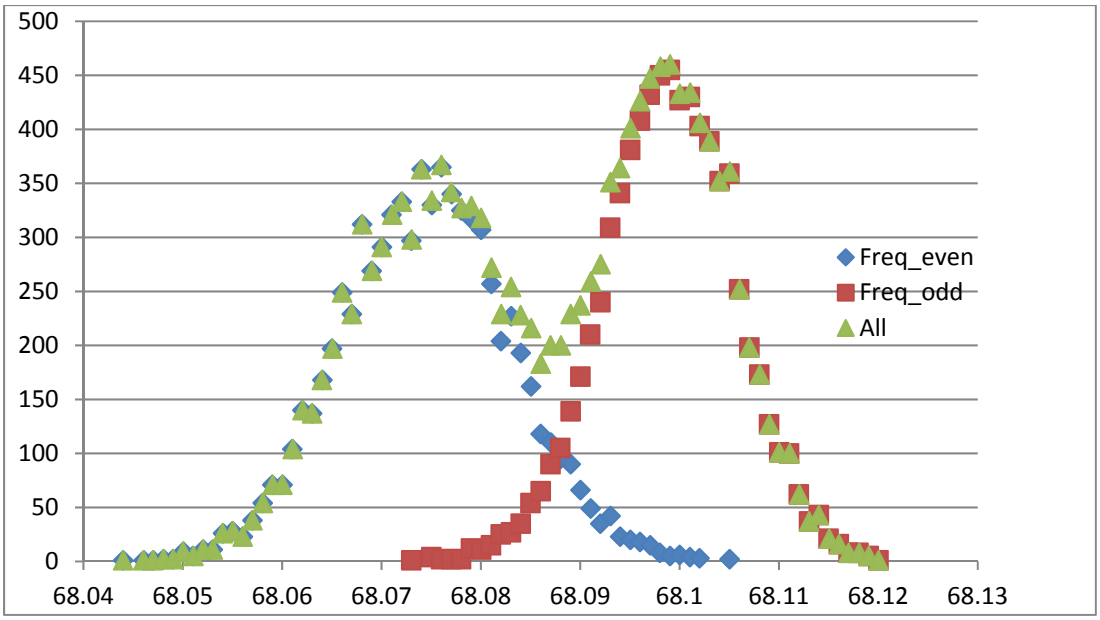

Figure 7.5 Bimodal distribution from the measurement data.
This bimodal distribution can be sorted into the distribution associated with even and odd samples, which add up to the bimodal distribution. This separation of the two peaks is around 45 micrometers, and the width of each peak is around 15 micrometers.

7.3 Dynamic Test and Analysis

After mounting the beam onto the cart (see Figure 7.6), we began the dynamic test.

Figure 7.6 Experimental setup mounted on a cart

In the moving measurement, the data in Figure 7.7 looks skewed because of the 45-degree angle between the heads and the axes of the beam. We set up the starting tape and center tape just for our own convenience to match the corresponding measurement.

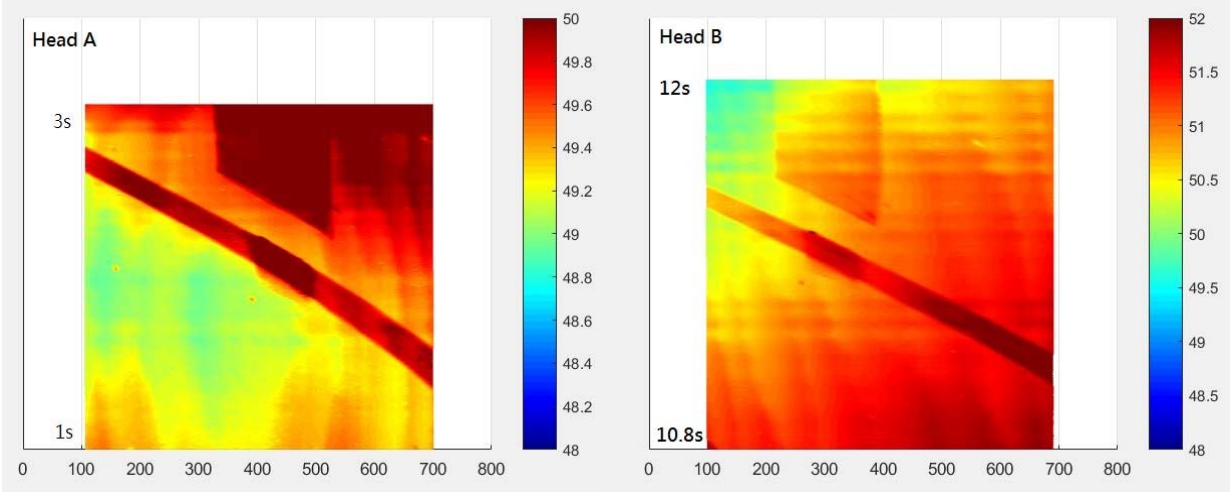

Figure 7.7 Original data from the moving test

To correct this angle distortion effect, we rotated the matrix by 45 degrees, with the resulting measurements shown in Figure 7.8.

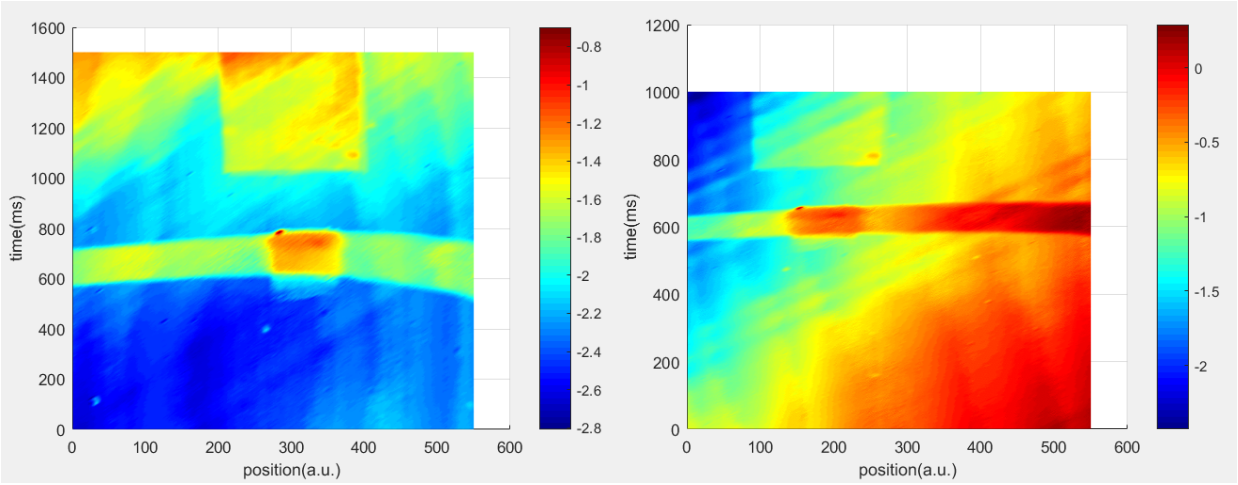

Figure 7.8 Measurement after angle correction.
The correction is done with time delay in each pixel. After the correction, the imaging tape looks same as our design.

The Figure 7.8 graph shows that the moving test can detect some objects on the ground, though we can also observe parallel lines in the direction of the sensing. These parallel lines are caused by errors in the altitude measurements over time, which we now investigate.

7.4 Mechanical Resonance of the Laser Sensor Heads

The parallel lines occurring in these graphs are associated with frequencies on the order of 8 to 10 Hz, as evidenced by the Fourier transform analysis. By mounting the sensor on a different object and observing the same effect, we traced this issue to a mechanical resonance of some internal component of the sensor. To validate this, we gently tapped the sensor, to observe its impulse response (response to an impulse). The impulse response of the sensors is shown in Figure 7.9. Figure 7.10 provides the Fast Fourier transforms.

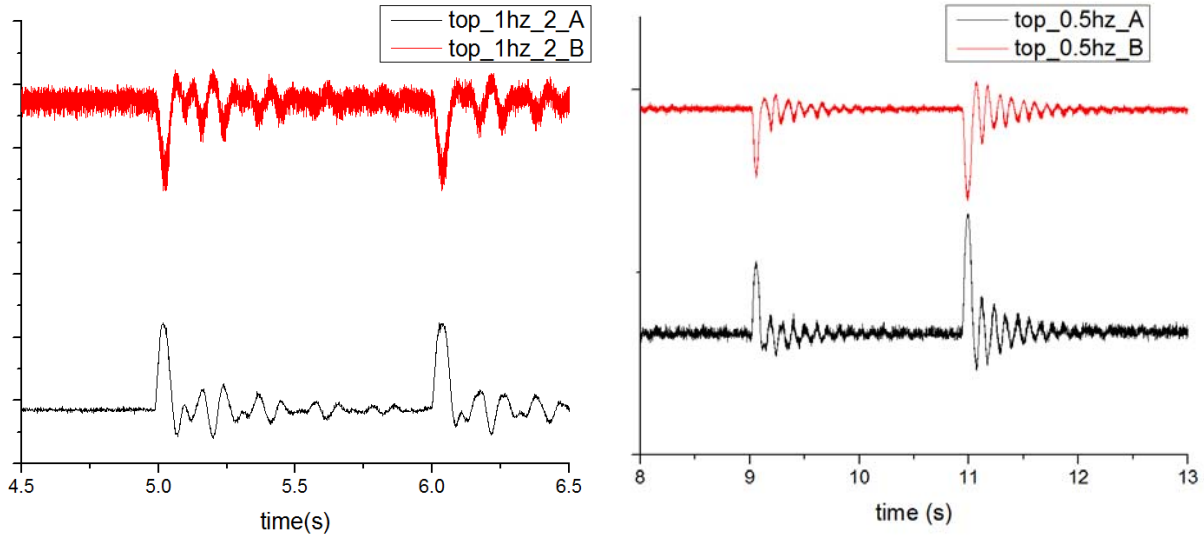

Figure 7.9 Impulse response of both sensors.
Both sensors have similar response, which shows that this response is not caused by a manufacturing defect in one specific sensor.

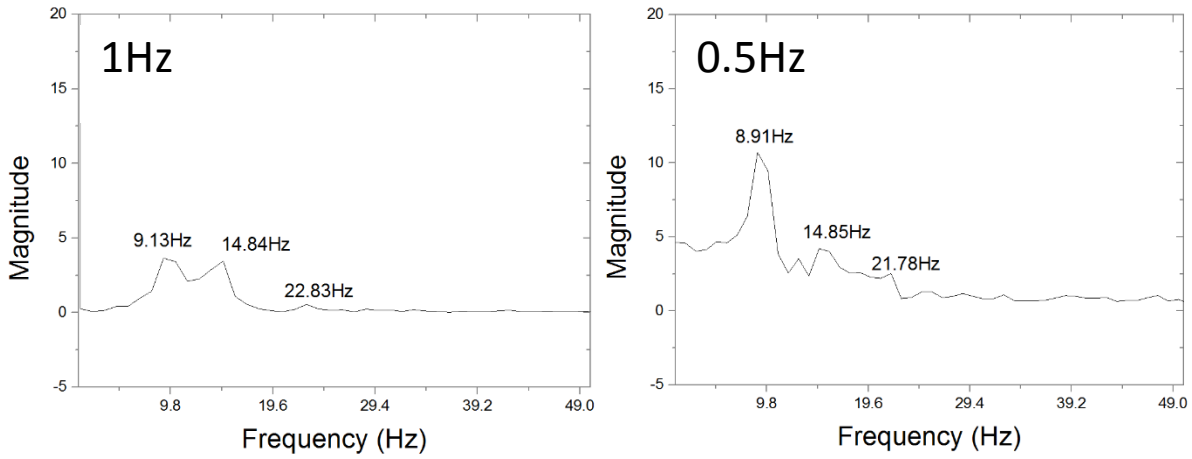

Figure 7.10 Fast Fourier transform of the above signals.
Given the duration of the experiment, the time-frequency uncertainty principle gives an error of $\Delta\omega.T\sim1$, or $\Delta\omega\sim1$ Hz for a duration of the experiment on the order of 1s, which explains the discrepancies between the frequencies measured in the left and the right subfigure (though these frequencies correspond to the same mechanical vibration mode).

The Fast Fourier transforms of the signal confirmed that the sensor has an impulse response with a dominant mode centered around 9 Hz. This can be a significant issue for future experiments, though this effect was not observed in the case of the truck experiments outlined here. The probable reason is that that the power spectral density of the truck vibrations in the 8–10Hz range is too low to excite this mode of resonance significantly. For some reason the cart (which has no suspension to filter high frequency modes, unlike the truck used in the field testing) was probably experiencing vibrations that had a much higher power density in this frequency range.

This problem has two possible solutions, should it arise again in future experiments (for example, with larger trucks that have larger engines, or with higher speeds, or due to aerodynamic noise that may occur in this frequency band):

- *Compensation using machine learning*: through observation, we can learn the functional relationship between the vibrations of the beam (as measured by an accelerometer placed on the beam) and the error created by the sensor. If this relationship can be learned with sufficient accuracy, compensating for these errors will simply amount to monitoring the accelerations around both sensors, and applying the machine-learned corrections to it in real time (which are functions of the vibration signal measured by the accelerometers). This approach provides a software solution to the problem.
- *Development of an active suspension system for the beam*: this approach effectively cancels the 8–10Hz mode through feedback control (for example, using fast hydraulic or electric actuators). This physical solution to the problem would in effect suppress the excitations of the sensors in this frequency band.

Chapter 8. Field Testing: Experimental Setup for Truck Testing

For this stage of experimentation, we used a Ford F150 light truck, which we equipped with two Keyence laser sensors, one accelerometer, and the required electrical equipment for powering the sensors and acquiring the data.

Head A and head B were mounted on a rigid aluminum profile, with a spacing of 0.72 m. An accelerometer was also mounted between heads A and B to measure the vibration levels. The profile was then mounted on the truck nerf bar using high strength plastic zip ties.
We used the following configuration for both heads:

- Operation mode of laser heads – Advanced function
- Triggering mode – Continuous sampling
- Sampling frequency – 1kHz, 2kHz
- Batch Measurement – ON
- Batch points – 15,000 (i.e., 15,000 profiles are measured in each batch). This is a fixed maximum number. The sampling rate governs how fast a batch measurement is completed. The higher the sampling rate, the faster the batch of 15,000 profiles can be acquired.
- 15,000 profiles (scan lines) are obtained by each laser head.
- X and Z ranges were both kept at FULL, resulting in 800 points or pixels (per profile or scan line).
- Binning and Parallel Imaging – OFF.

The complete setup is shown in Figure 8.1:

Figure 8.1 Experimental data acquisition setup, as mounted on Ford F150 light truck. The top image shows the devices as mounted on the truck nerf bar. The bottom image shows a close-up view of head B, as mounted on the aluminum profile.

The devices were mounted on the passenger side of the truck, with head A preceding head B when the truck is driving forward.

8.1 Static Testing

Static measurements were taken to calibrate both the heads and adjust their levels, creating similar measurement values of the height from ground by both the laser heads. These measurements were taken with the truck engine running, and the parking brake ON, allowing the research team to understand the impact of engine vibrations on the measurements.

As a first experiment, an object was placed below both sensor heads, to check the consistency of the measurements generated by both heads. After correction and leveling of the laser heads, the following results were obtained (see Figure 8.2 and 8.3) and then compared (see Figure 8.4):

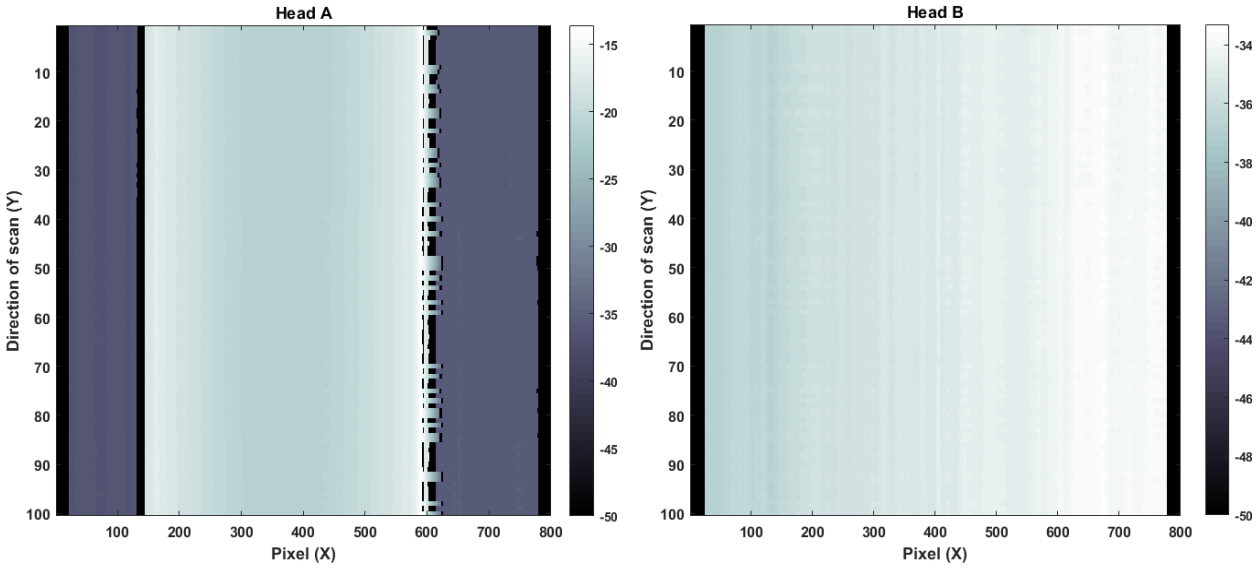

Figure 8.2 Reference object placed under head A

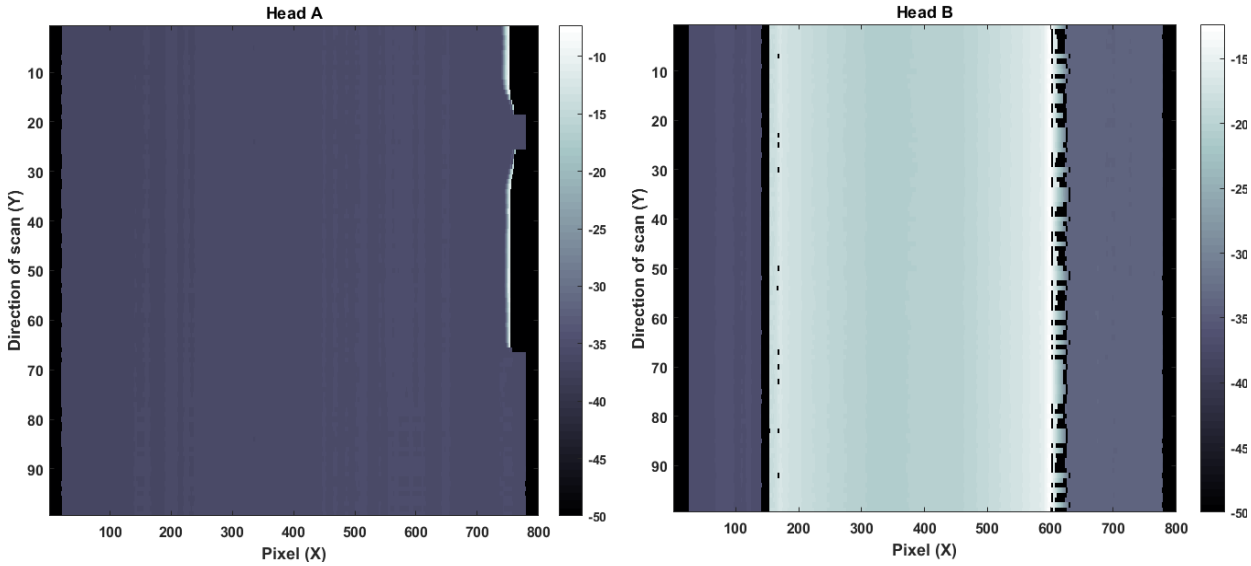

Figure 8.3 Reference object placed under head B

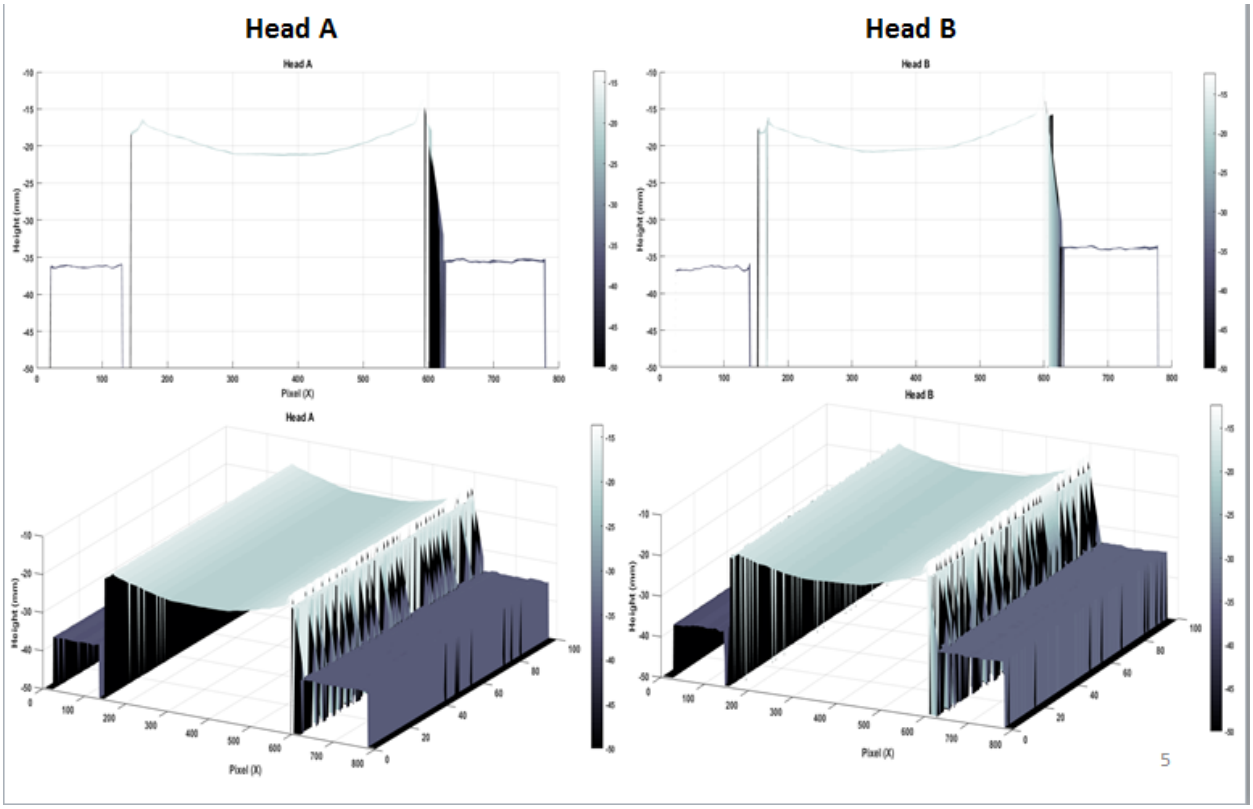

Figure 8.4 Comparison of identical object profile under the laser heads A and B

The ground height measurements taken by both heads are provided in Figure 8.5.

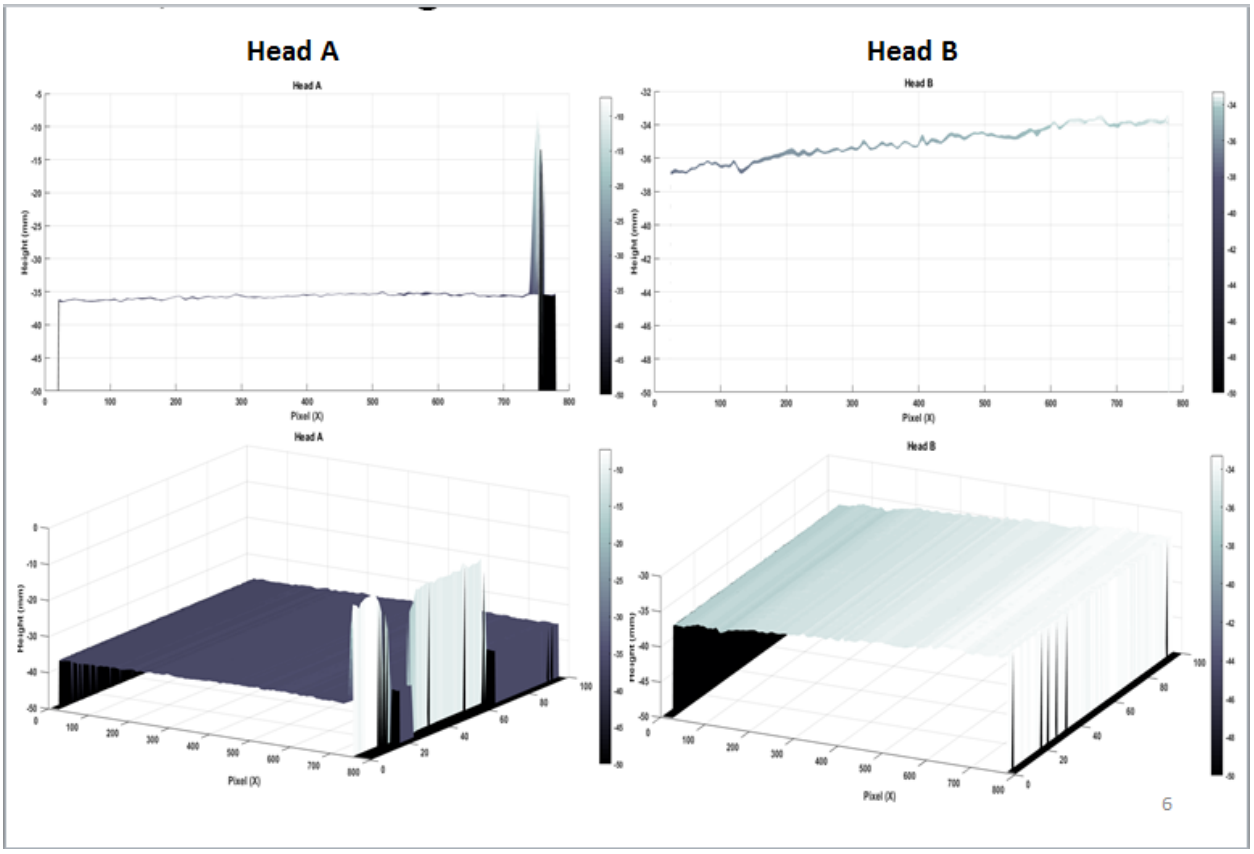

Figure 8.5 Ground height measurement by both heads.
Top left figure height axis is -50 mm to -5 mm. Top right figure height axis is -50 mm to -32 mm. Bottom left figure height axis is -50 mm to 0. Bottom right figure height axis is -50 mm to -30 mm.

8.2 Conclusions of the Static Truck Testing

As Figure 8.5 indicates, the noise levels in head A and head B were fairly consistent between both heads. The spatial variations are on the sub millimeter scale, and are consistent with the texture of the reference object's surface. Figure 8.5 demonstrates that head B was slightly tilted, and exhibited a slight linear bias on the order of 1mm/10cm—that is, about 0.6 degrees. This slight tilt is consistent with mounting errors on the aluminum profile, since we did not use high precision machinery to drill holes and bolt both sensors.

Once static measurement was completed and the heads were leveled to give an approximate height measurement of -35 mm for the ground, the research team conducted experiments with the truck moving over pavement structures.

8.3 Dynamic Testing

The second step was to evaluate the performance of both sensors under a dynamic setting—that is, with the truck moving while the system acquires measurements.

8.3.1 Raw Measurements

In a dynamic setting, the additional vibration and motion caused challenges in terms of data processing. The raw measurement data appears to be quite noisy (see Figure 8.6), with only major features (large cracks) identifiable between the elevation measurements generated by the heads.

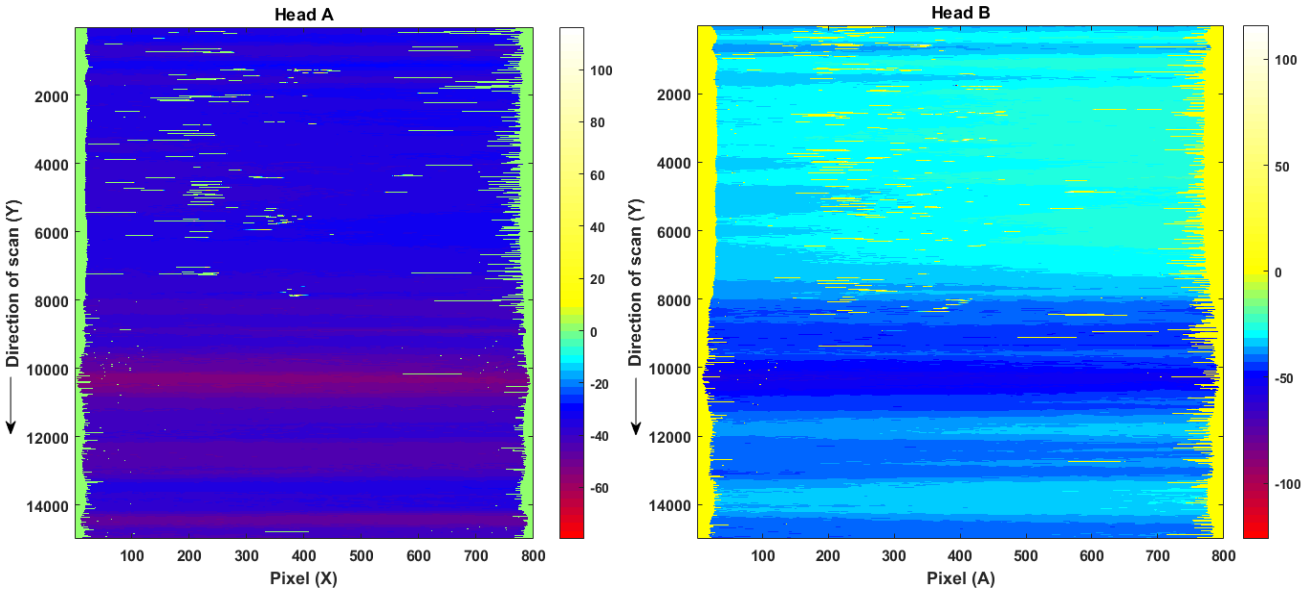

Figure 8.6 Raw data plots

The above plot depicts the scanned data as an elevation image. The X axis represents the data points (pixels) for each profile (800 pixels/data points), while the Y axis represents the number of profiles and direction of scan as time progresses (15,000-line profile measurements in this experiment). The color map depicts the range of height values of various structures in the scanned area (using millimeter units). The bright green and yellow areas in the plots are dead pixels, which we set to a zero value.

As the plot in Figure 8.6 demonstrates, the variations in space and time were considerable, and masked the features of the pavement, which becomes unrecognizable. Therefore, we developed a set of processing tools to filter the noise, which we now explain.

8.3.2 Processing Algorithms

The following flowchart (Figure 8.7) gives a high-level overview of the different steps used to process the data generated by heads A and B, to allow the measurement of the pavement texture and the matching of position data generated by both heads.

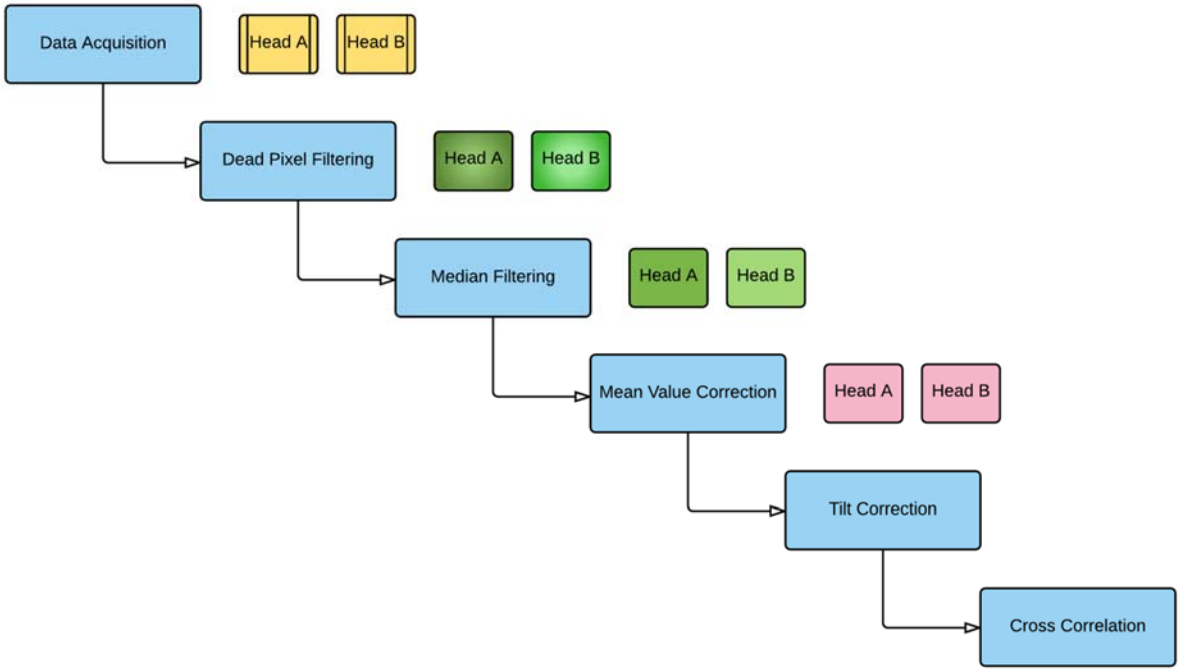

Figure 8.7 Flowchart for data processing

The steps are detailed below:

i) **Data Acquisition** – The data generated by both the laser heads was saved in a CSV file by the software provided by Keyence. This corresponding file was then imported into MATLAB as an array, and the data of each head was extracted into two separate matrix structures.

ii) **Dead Pixel Filtering** – At their full measurement range of 800 points per profile, there were some dead pixels at the edges as well as in the regions that are in shadow. As a result, the laser head did not receive accurate reflection from such areas. These dead pixels always have a fixed value (low off scale, which implies that no signal is reflected back to the head). These values were arbitrarily set to zero within the active region of the scan. The dead pixels on the edges were chopped off by resizing the matrix, eliminating the corresponding columns.

iii) **Median Filter** – Since the data can be affected by impulse noise and spikes, we chose a median filter (which is much more robust to this type of noise than the classical low-pass filter) to eliminate spikes. The median filter we used was a 1×5 filter, in that it computed the median of the height measurements within a 5-pixel window on the X axis, which corresponds to the same scanline. A median filter acts like a mask for a defined area; Figure 8.8 provides an example of a 3-pixel by 3-pixel mask. The mask was moved over the image (in this case, data generated by the laser heads) one pixel at a time.

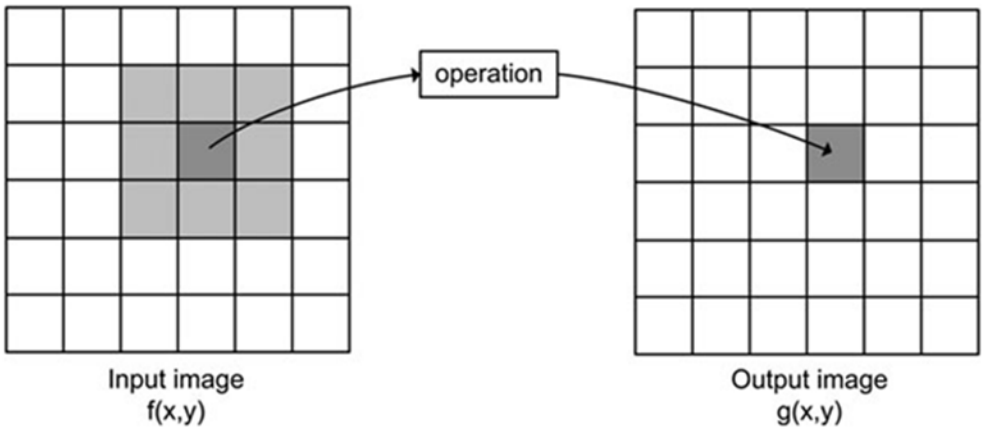

Figure 8.8 Example of 3x3 median filter

In Figure 8.8, the center of the mask is above a pixel in the image (the dark gray area in the figure) and has a neighborhood surrounding it (the figure's light gray area). All these values of image data covered by the mask are then ordered from smallest to largest. From this ordered list of image values, the median value is identified, which replaces the current value of the center pixel. This operation is then repeated for each pixel across the image. Median filtering is widely used to remove noise in images, particularly when this noise is in the form of spurious spikes.

iv) **Mean-Value Correction** – Since head A and head B had a random vertical motion that was not necessarily correlated (since the nerf bar can have a random position and pitch angle), we had to correct the mean values for each scanline to make sure that measurements are reproducible. This correction also eliminated the low-frequency oscillations that appear due to the internal mechanical properties of the laser sensors. This correction used the following operation: for each pixel z=f(x,y), we computed the corrected pixel distance as $z_c = z - \frac{1}{n}\sum_w z(w, y)$, thus removing the mean value of the scanline to each pixel in the scanline. This ensured that all scanlines had a zero mean, and were comparable.

v) **Tilt Correction** – Because of imperfections in the vertical alignment of both heads, we had to estimate the relative tilt between head A and head B (since we did not have high precision angle measurement tools available, we could measure only the relative tilt between A and B, assuming that the tilts of A and B were small). As seen in the static experiment figure, A and B had an approximate angle of 0.5 degrees between them, likely the result of drilling and assembly using non-precision machinery. The corresponding offset was removed from the measurements of head B, which ensured that the tilt angle between A and B was negligible.

vi) **Cross Correlation** – To match the images generated by both heads, we used a cross-correlation approach, which assumes that the images were not too distorted (distortion can be caused here by the roll angle of the truck, by fluctuations in the forward velocity of the truck, or by random lateral motions).The cross-correlation approach computes the correlation coefficient between a reference image (for example, one generated by head A), and a target image (for example, one generated by head B), comparing the position of the

target image with respect to the reference image. A match is achieved when the correlation between the original image and the target image reaches its highest level, and the resulting correlation coefficient provides us information on the quality of the match.

8.3.3 Results from the Cascaded Filters

Figure 8.9 represents the raw data after the dead pixels were removed (by resizing the matrices) and the median filter applied. As this figure demonstrates, the results are much more accurate than in Figure 8.6, and allow us to view the random mechanical vibrations of the laser sensors, which create horizontal bands.

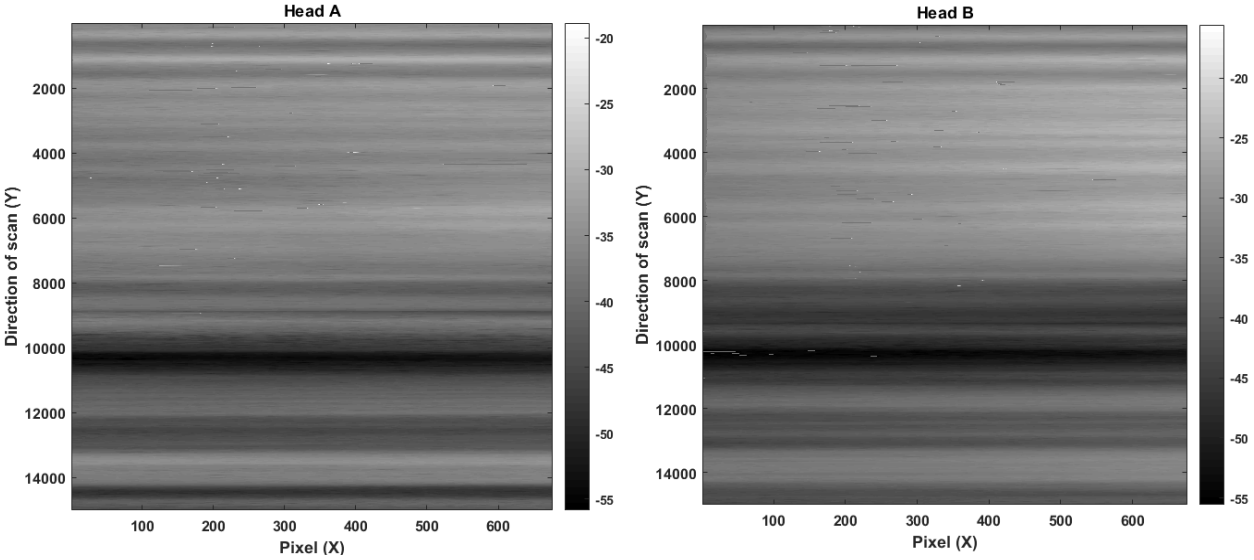

Figure 8.9 Median-filtered data generated by head A and head B

The frequency of the oscillations appearing in this figure is consistent with the frequencies that were observed earlier in the lab tests. The amplitude of these oscillations is significant enough to mask the underlying texture of the pavement, which requires the application of the mean-removal filter.

8.3.4 Experiment 1 – Median-filtered Head A Data Plot

Figure 8.10 and 8.11 illustrate the same data as in Figure 8.9, but in tridimensional surface plots. Noise spikes persisting even after the filtering operation can be easily observed. While this noise could be removed by applying a median filter with larger window size, such a filtering would in effect cause all textures that vary over a scale smaller than the window of the median filter to disappear, greatly affecting the matching between the images generated by head A and head B.

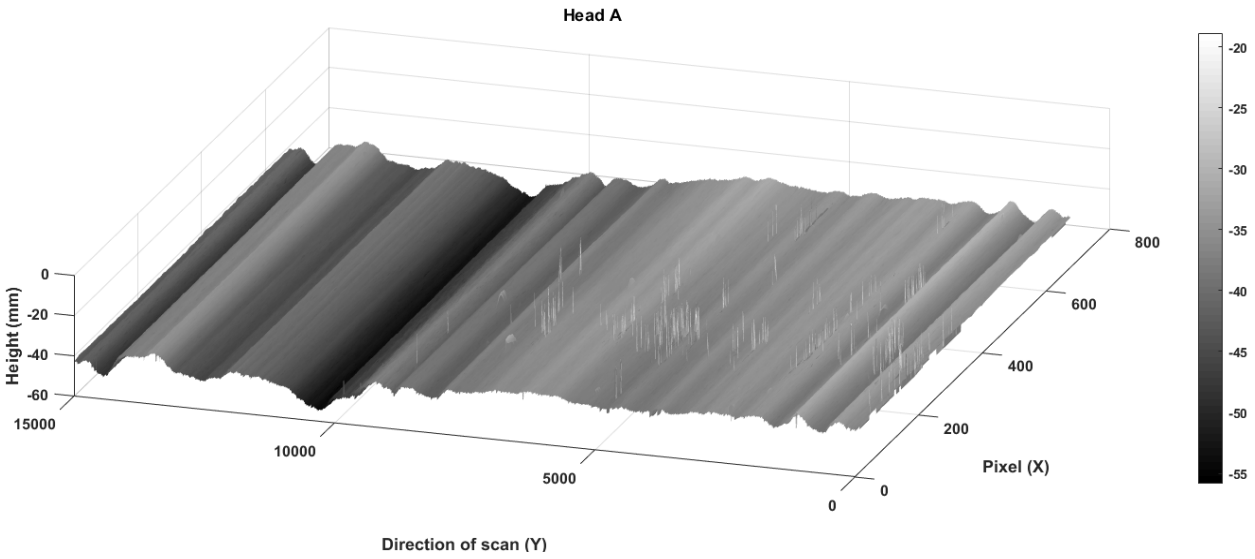

Figure 8.10 Experiment 1 – head A filtered data 3D plot

The following 3D plot is for head B. One can observe a similar performance between head A and head B. The vertical bands do not match (since they are caused by random vibrations inside each device, which are largely independent), but the level of uncertainty (in millimeter) is comparable.

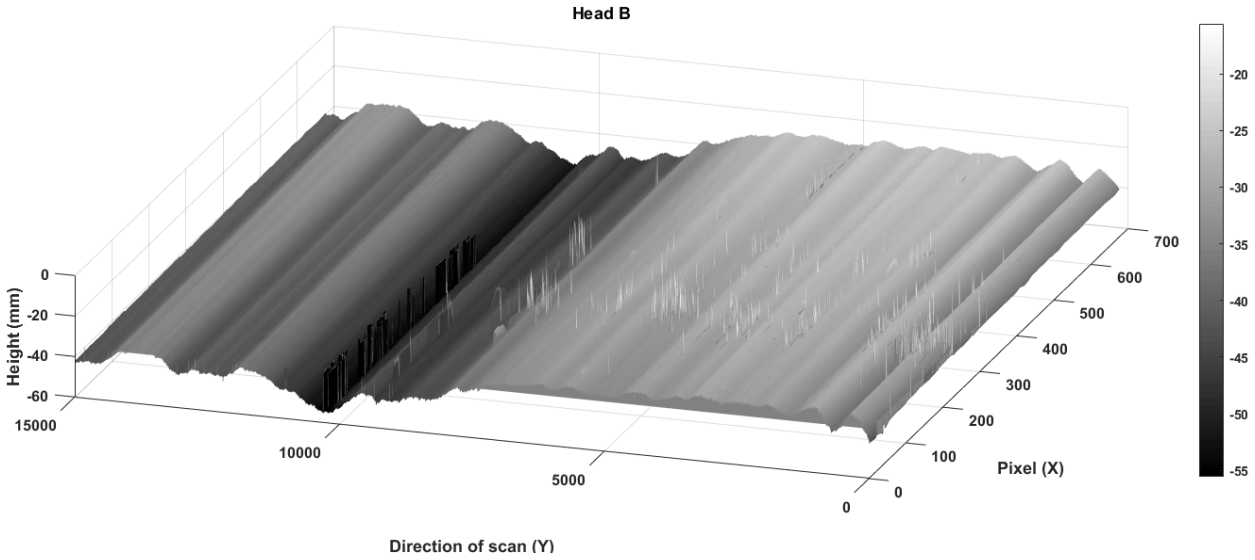

Figure 8.11 Experiment 1 – head B filtered data 3D plot

In this experiment, we translated the measurements of head B in time, such that the Y axes represent the same physical position for both sensors. With this correction, the data generated by both sensor heads should be in agreement. As Figure 8.12 indicates, there is a considerable discrepancy between both measurements, with banding at a time scale on the order of 1s or less. This effect is due to the vibrations of the truck and laser sensor system, at a scale of a few millimeters, and prevents us from matching the measurements from both sensors head directly, as the tridimensional plots in Figure 8.12 show.

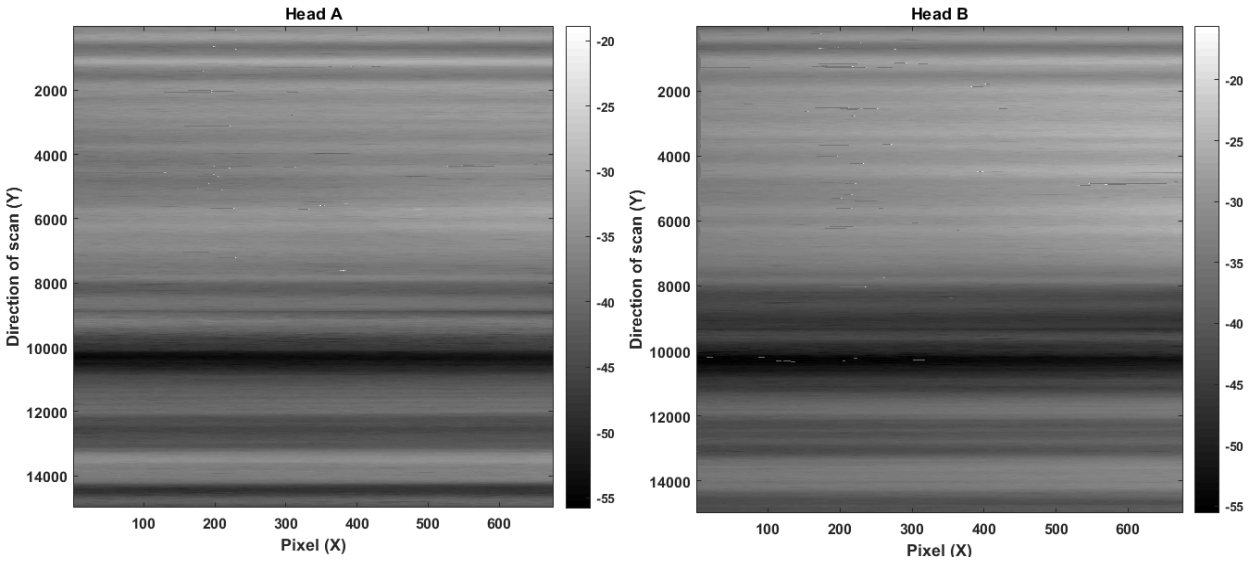

Figure 8.12 Experiment 1 – head A and head B translated data

8.3.5 Plot of a Section of the Data for Head A

Figure 8.13 illustrates a section of the scanned area for head A. In the previous 3D plots, the texture is not distinguishable due to the high volume of data. The plot in Figure 8.13 depicts the minute texture of the pavement, on the order of a few millimeters, that the laser head was able to capture while on a moving vehicle, though the vibrations of the system (truck + laser sensors) severely affected our ability to identify the actual ground surface characteristics. Figure 8.14 provides the plot for head B.

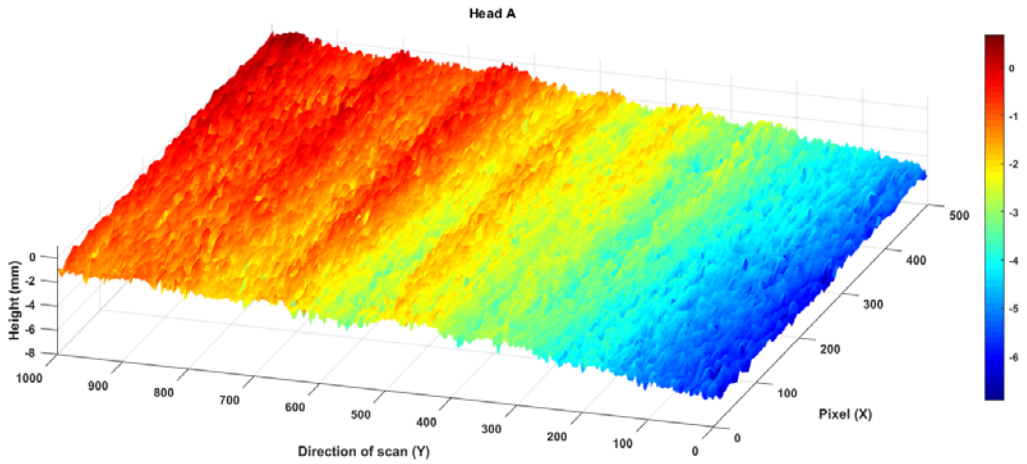

Figure 8.13 Plot of a section of the data for head A

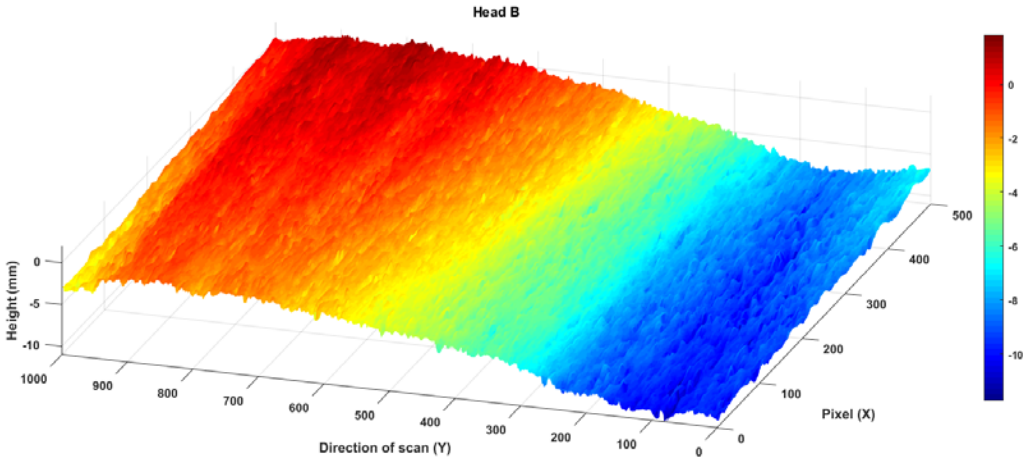

Figure 8.14 Plot of a section of the data for head B

Both the sectional plots of head A and head B are of the same area.

We now investigate the mean value correction algorithm. The mean value correction algorithm was based on the following considerations:

- The time required to execute a complete scanline (less than 1 ms) was considerably less than the duration of the mechanical resonance of the sensor (about 100 ms).
- The mechanical vibrations of the truck were filtered by the suspensions, which acted as a low pass filter with a cutoff frequency of a few hertz. If we exclude the contribution from the engine and the transmission, the truck-induced vibrations also lasted considerably longer than the duration required to perform a scan line.

We validated this hypothesis by plotting the time series of the mean of the measurements across the x axis (scanline), over time. As Figure 8.15 indicates, the time constants associated with evolution of the mean (across a scanline) of the elevation are on the order of 1s.

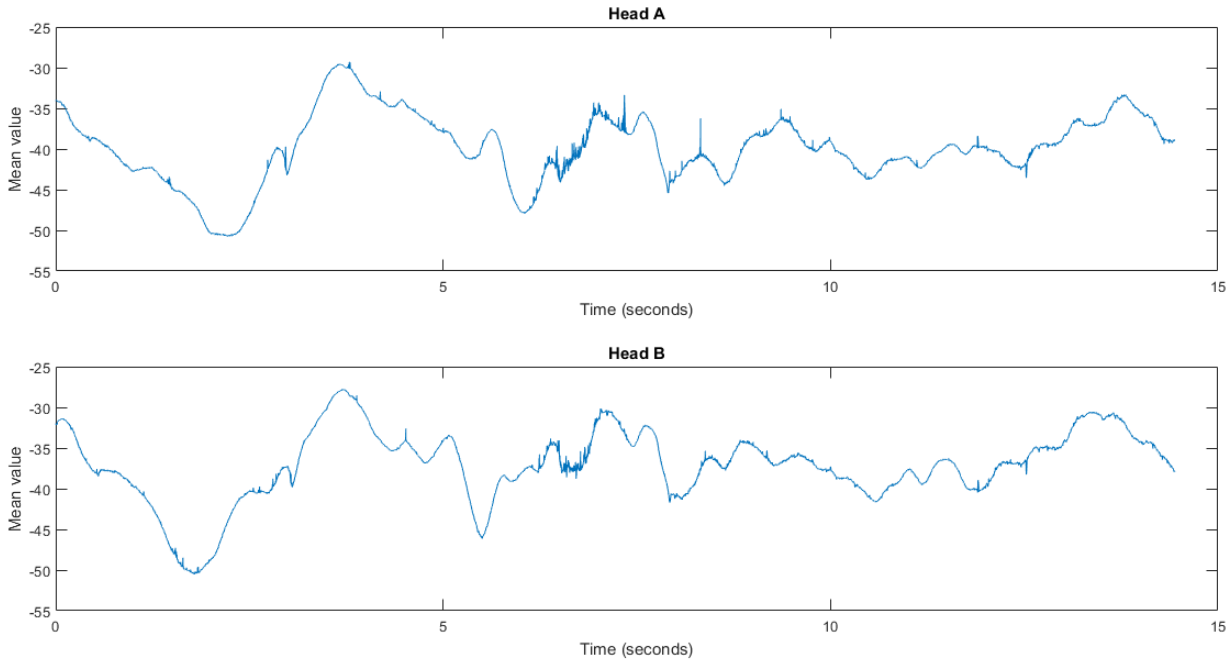

Figure 8.15 Time constants associated with evolution of the mean

The Fourier transform of the signal shows the frequencies associated with the signal. These frequencies are vastly lower than the sampling frequency of the sensor. Note that the sensors were configured with a sampling frequency of 1 kHz, which is considerably lower than the settings that will be used in future experiments (the sensor itself can be configured to frequencies up to 64 kHz), which will maintain the validity of the above assumptions in practical experiments. For example, at a 32 kHz setting, we can exclude the effect of disturbances associated with frequencies that are less than 500 Hz. Since the time constants associated with the vibrations are much larger than the time constant associated with a scanline, we can exclude any motion of the truck occurring during this scanline. In effect, the disturbances can be modeled as a time-varying offset (which remains highly correlated over time, since the time constants differ so greatly).

To filter this offset, we subtracted the mean value (across a scanline) from the corresponding values of the elevation measured by the sensor. This step created a much smoother surface, allowing us to identify the texture of the pavement. Figure 8.16 illustrates the detection of a crack by both heads.

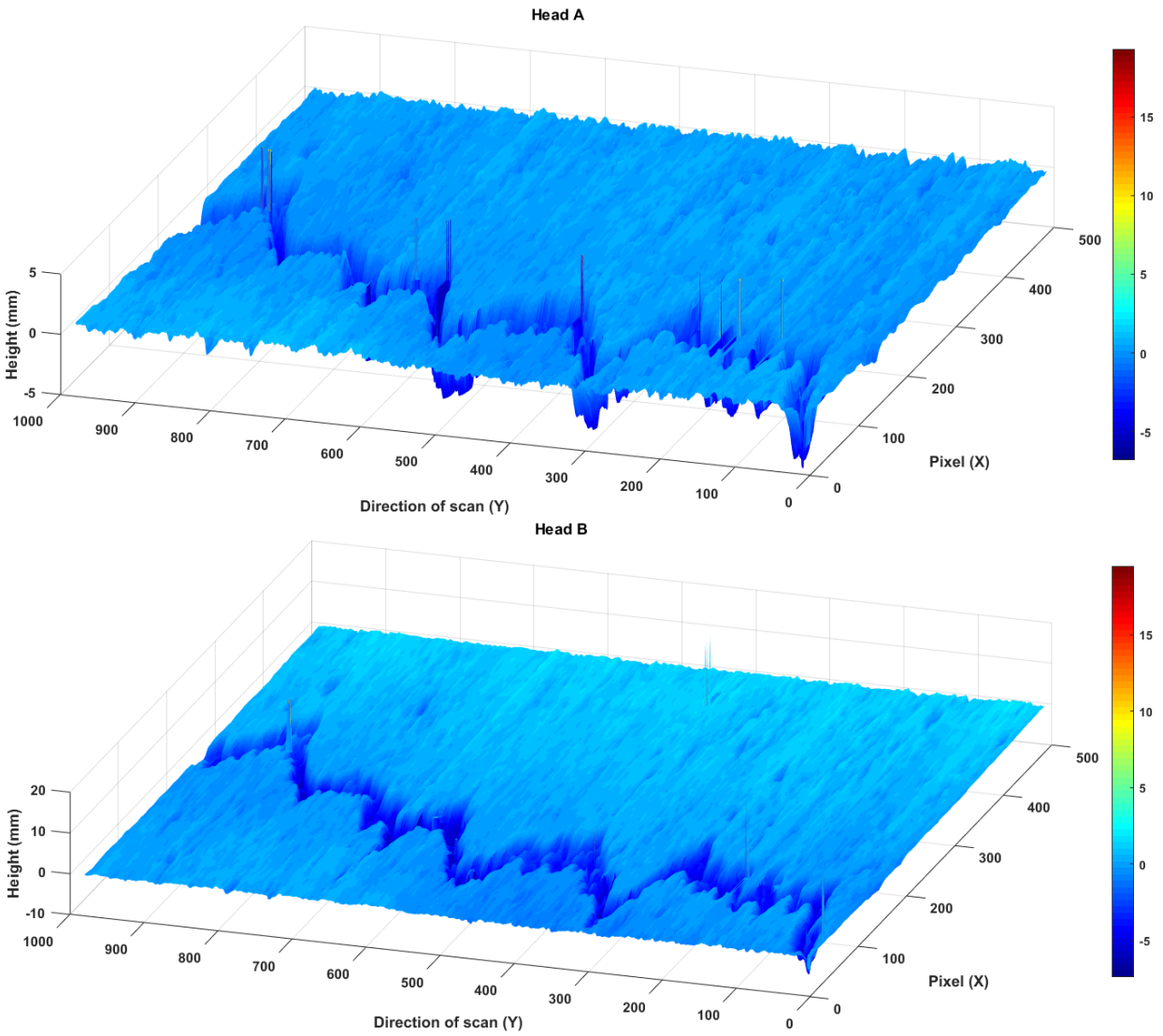

Figure 8.16 Detection of a road crack using head A and head B

As Figure 8.16 attests, the pattern of the crack is similar, which shows that the measurements are reliable. To analyze the data further, we had to take one final correction step, to address the issue of the unknown tilt between heads A and B.

8.3.6 Tilt Correction

The sensors were attached to an aluminum profile using bolts and nuts. The alignment between the sensor and the profile was not perfect, due to manufacturing tolerances (and because the torque tension of the bolt cannot be too high, as this would damage the laser sensor structure). Since the angles are extremely small, we can assume that their sine is equal to the angle, and the correction becomes a linear function of x to add or subtract to the data. The slope of this function was determined by comparing the data generated by both sensors, and minimizing the residuals over a large number of data samples. We found that the angle between head A and head B was less than 1 degree, and the optimal angle (that minimized the residuals) was fairly consistent between

datasets, indicating that this angle was induced during the mounting process, and not caused by other environmental effects (such as thermal expansion), which would be time varying.

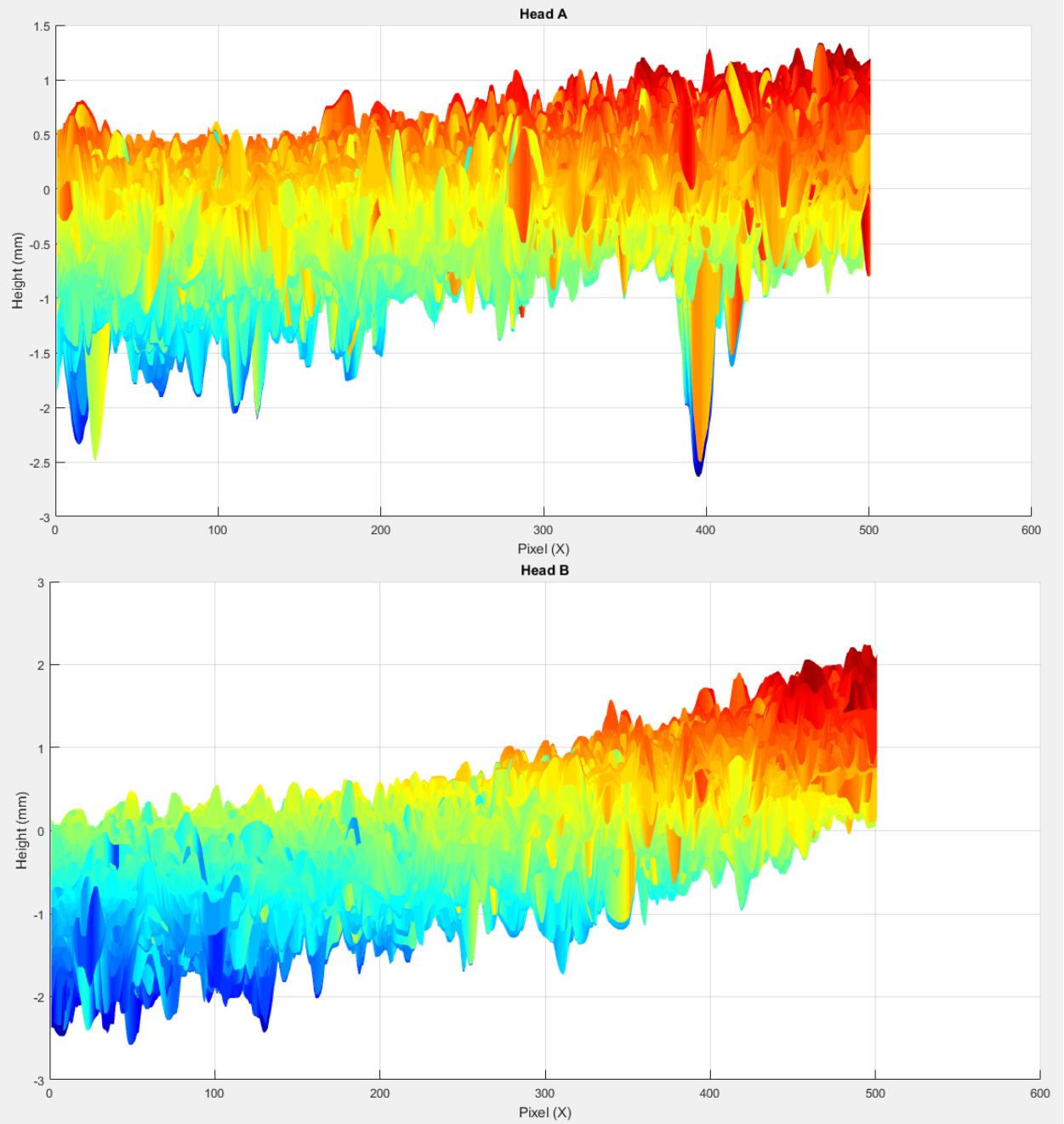

Figure 8.17 Systematic errors induced by relative angles (tilt) between both sensor heads

Figure 8.17 shows the effects of tilt on the data. Tilt correction allows one to cancel this effect, resulting in an accurate matching between sensor heads, which we now outline.

8.3.7 Matching between Sensor Heads

With all the above corrections, the research team was able to attain an excellent level of matching between sensor heads. Correlation can be performed automatically by computing the cross-correlation function, which measures the degree of correlation of the two images as the images are translated above one another, and determines the best X and Y positions for both images to match.

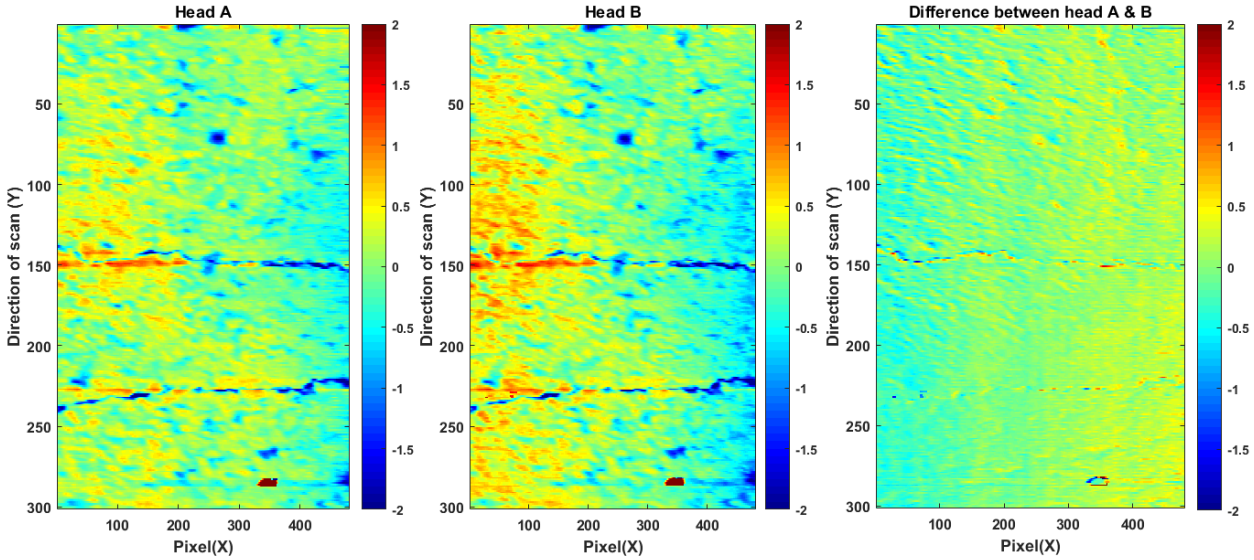

Figure 8.18 Matching the data generated by head A and head B, over a 0.3s pavement scan

As Figure 8.18 indicates, the matching between heads A and B is excellent, with very few features remaining when subtracting both images. This result indicates the following:

1) The sensors provided highly accurate vertical distance measurements, with residual errors on the order of 0.5 mm or less (per pixel), which is commendable given the very fine scale irregularities of the pavement (the positional uncertainties are on the same order of magnitude, as can be seen with the residuals of the horizontal cracks in Figure 8.18).
2) Matching the horizontal positions of heads A and B during an experiment is possible, with great accuracy (about 0.5 mm).
3) The velocity of the truck did not change by more than 0.5 mm/s over the scan time (based on the residuals), which implies that the velocity of the truck is very stable. At higher speeds, the relative error on the velocity will be even less, which will allow us to efficiently search a very small domain in space (defined by the uncertainty in relation to the speed of the truck) to match the image generated by head B with head A (and with head C in the deflection scanning configuration).

We found similar results across multiple experiments. Figure 8.19 shows a similar high level of precision in matching over datasets.

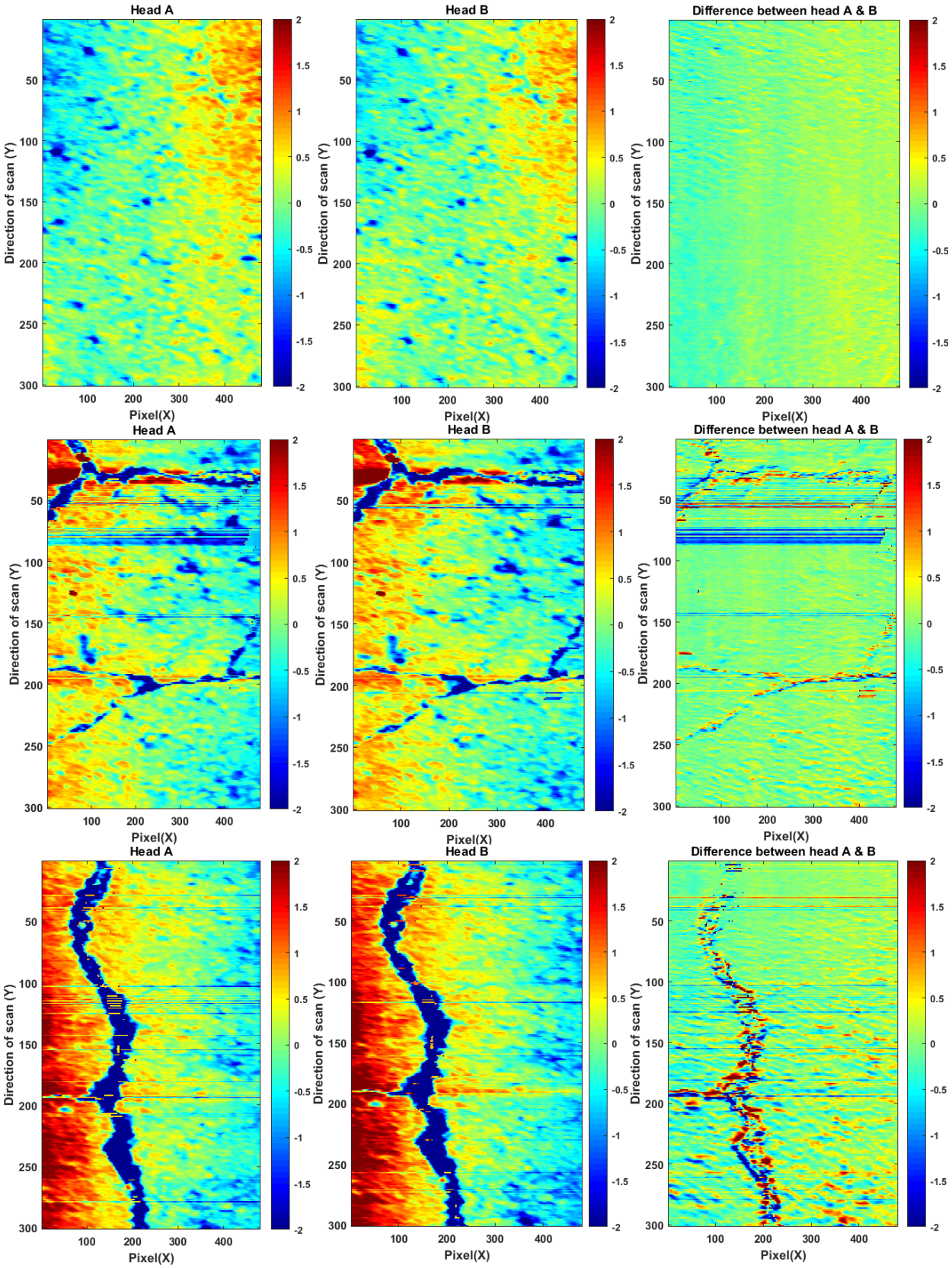

Figure 8.19 Matching over datasets

As the above figures attest, only residual errors are noticeable, found at the boundaries of large features (such as road cracks), which are caused by the imperfect positioning of the laser (due to uncertainties in truck velocity, truck lateral position, and random roll variations in the truck attitude).

Another example of matching between head A and head B is provided in Figure 8.20.

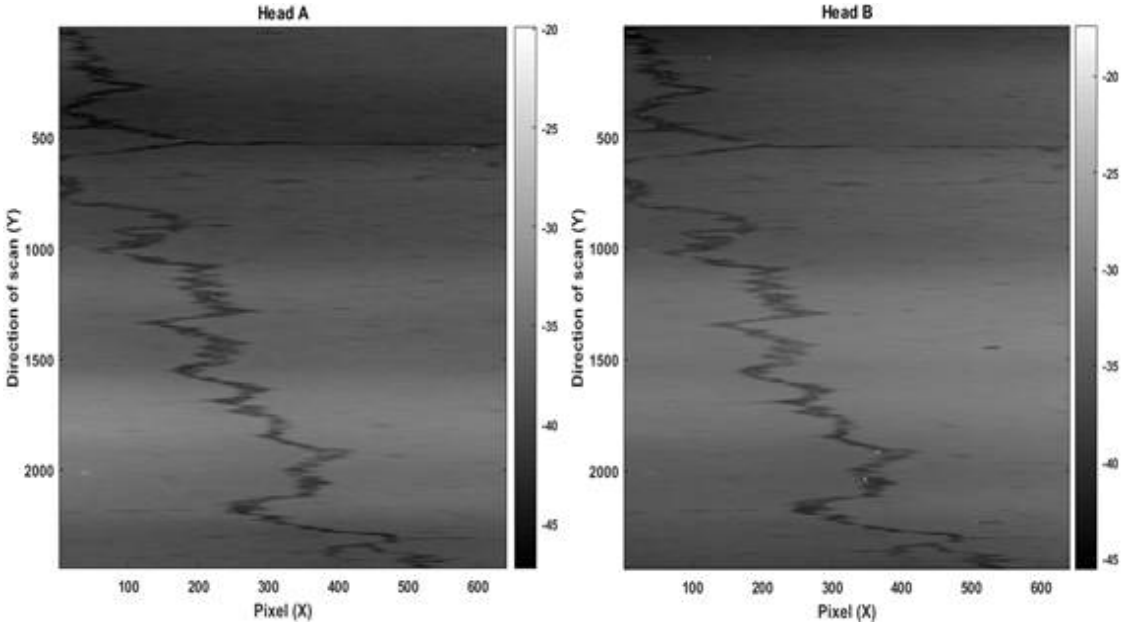

Figure 8.20 Matching between head A and head B

8.3.8 Matching Accuracy

The correlation between head A and head B was primarily hampered by the imprecision of the sensor readings around large objects, which affected the reflected signal. Table 8.1 summarizes the correlation coefficients obtained for our complete dataset:

Table 8.1: Correlation coefficients obtained

Run	Section	Processing	Base correlation (over entire data)	Clean section correlation
5	Section 1 (10000 to 11000 scan lines)	Translation Tilt correction 1x5 median filter	0.67	0.84
5	Section 1 (10000 to 11000 scan lines)	Translation Tilt correction 5x5 median filter	0.81	0.87
5	Section 2 (11000 to 12000 scan lines)	Translation Tilt correction 1x5 median filter	0.81	0.92
5	Section 2 (11000 to 12000 scan lines)	Translation Tilt correction 5x5 median filter	0.86	0.93
5	Section 3 (12000 to 13000 scan lines)	Translation Tilt correction 1x5 median filter	0.64	0.76
5	Section 3 (12000 to 13000 scan lines)	Translation Tilt correction 5x5 median filter	0.80	0.88
5	Section 4 (13000 to 14000 scan lines) (crack)	Translation Tilt correction 1x5 median filter	0.76	0.84
5	Section 4 (13000 to 14000 scan lines) (crack)	Translation Tilt correction 5x5 median filter	0.85	0.94

As always, the correlation coefficient summarizes the degree of correlation (linear dependence) between the two datasets. Matching can be further improved by considering a nonlinear dependence between datasets—for example, using nonlinear machine vision tools such as contour detection or thresholding.

8.3.9 Practical Feasibility of the Above Corrections

All the corrections outlined above work in a practical setting for pavement matching purposes. The mean correction step provides us the relative difference in altitude of head A and head B, as they pass over a given point in space X. We evaluated the accuracy of the resulting relative position measurement, which is one of the two measurements required to determine the deflection (the other measurement is the attitude of the beam, which is provided by the ring laser gyro attached to it). To this end, we computed the RMS error in the residuals between head A and head B, which show us the uncertainty we have in the vertical axis when performing the matching. A 1-mm RMS error, for example, would mean that on average the points measured by A and the points measured by B differ by about 1 mm in elevation, even after doing our best to match them.

For the experiments we carried out with the truck, the RMS error was on the order of 0.1 mm or less (ranging from 0.08 mm to 0.1 mm). Though this performance is very good, recall that

we need a vertical position matching that is significantly less than 20 micrometers to ensure that our residual error in position estimation from head C is less than 50 micrometers.
Since the RMS error measures the average dispersion of the measurements for each single point, it overestimates the altitude estimation error that can occur when averaging the altitude measurement over a complete scanline. If the distance measurement error is Gaussian (which appears to be the case from the early lab tests, as noted earlier), then the error e in estimating the altitude from N points can be determined from the RMS error of a single point r by:

$$e = \frac{r}{\sqrt{N}}$$

Hence, if we consider half a scanline (400 points), for example, the actual error in altitude estimation is on the order of $e = 5.10^{-6}\, m$, or 5 micrometers, which is well within our specifications.

The positioning error related to the ring laser gyro is on the same order of magnitude (according to the ring laser gyro datasheet that we consulted), and therefore we expect a total measurement uncertainty on the order of 50 micrometers, provided that the preliminary analysis we conducted in this low-speed setting holds at higher speeds.

Following are the identified sources of uncertainty and the order of magnitude of uncertainty that they induce:

- Deviation from the rigid body assumption (deformation of the beam): 5 micrometers
- Altitude error when matching head A and head B: 5 micrometers
- Altitude error of head C: 5 micrometers
- Pitch error (ring laser gyro integration) over 1 second, for a 5-meter beam: 4 micrometers

Since the performance of the ring laser gyro has not been validated in this setting, the last figure is highly uncertain. It is based on a random-walk assumption (error growing in $\sqrt{t}$), with the diffusion coefficient specified in the datasheet, which the research team has not validated.

Chapter 9. Pavement Deflection Measurement: Experiment Setting and Observations

This chapter provides the results of the field testing conducted with the truck-based system. Two sets of experiments were performed to obtain pavement deflections induced by front and rear wheels of a Ford F150 XLT truck.

9.1 Field Testing Equipment and Setup

These devices were used to quantify the pavement deflections:

- Road Surface Deflectometer (RSD)
- Keyence High Precision laser (LJ-V 7300)
- PCB 393B31 Accelerometer

These experiments consisted of driving the vehicle straight from a distance towards the assembled setup of RSD, laser, and accelerometer at varying speeds. Figure 9.1 illustrates the second experimental setup.

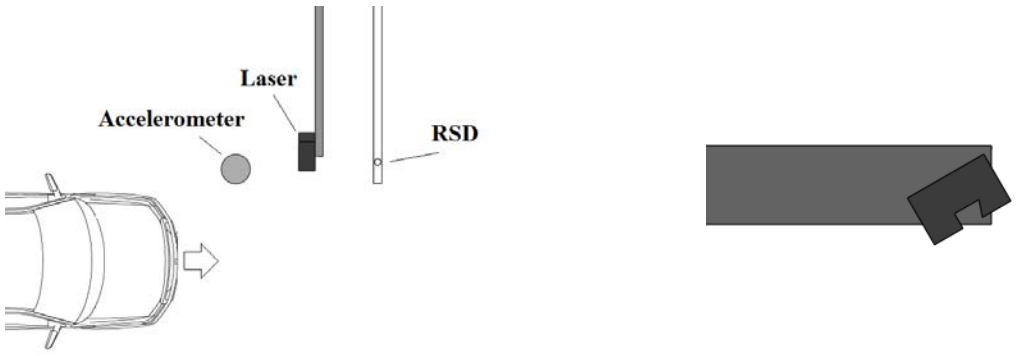

a) b)

Figure 9.1 Second experimental setup: a) top view of setup of RSD, laser, and accelerometer; b) side view of laser on cantilever beam at an angle of 30 degrees

Each experiment comprised conducting multiple runs of driving from a distance across the setup of sensors to observe pavement deflections from the front and rear wheels. In all the runs depicted, the first deflection observed is from front wheel and second deflection is due to rear wheel. Table 9.1 elaborates more on the conditions of the experiments.

Table 9.1: Experimental conditions and setup

Experiment	Set 1	Set 2
No. of runs conducted	4	15
Load	Ford F150 XLT	Ford F150 XLT
Laser sampling frequency	2kHz	2kHz
No. of datapoints/pixels measured by laser	400 (9cm wide region)	400 (9cm wide region)
Laser measurement height range	+/- 75 mm	+/- 75 mm
Laser mounting angle (with respect to ground)	0 degrees	30 degrees
Accelerometer sampling frequency	1.652kHz	1.652kHz
Ambient light conditions for the laser	Continuously in shade	Shade provided briefly by the truck

To summarize the results and observations from the experiments, we will detail a few runs from the two experiments in later sections. The next section briefly elucidates the processing steps applied to the laser measurement data.

9.2 Processing Algorithms

The following flowchart (Figure 9.2) gives an overview of the techniques used to process the data generated by the laser for obtaining the deflection regions. Table 9.2 summarizes the runs.

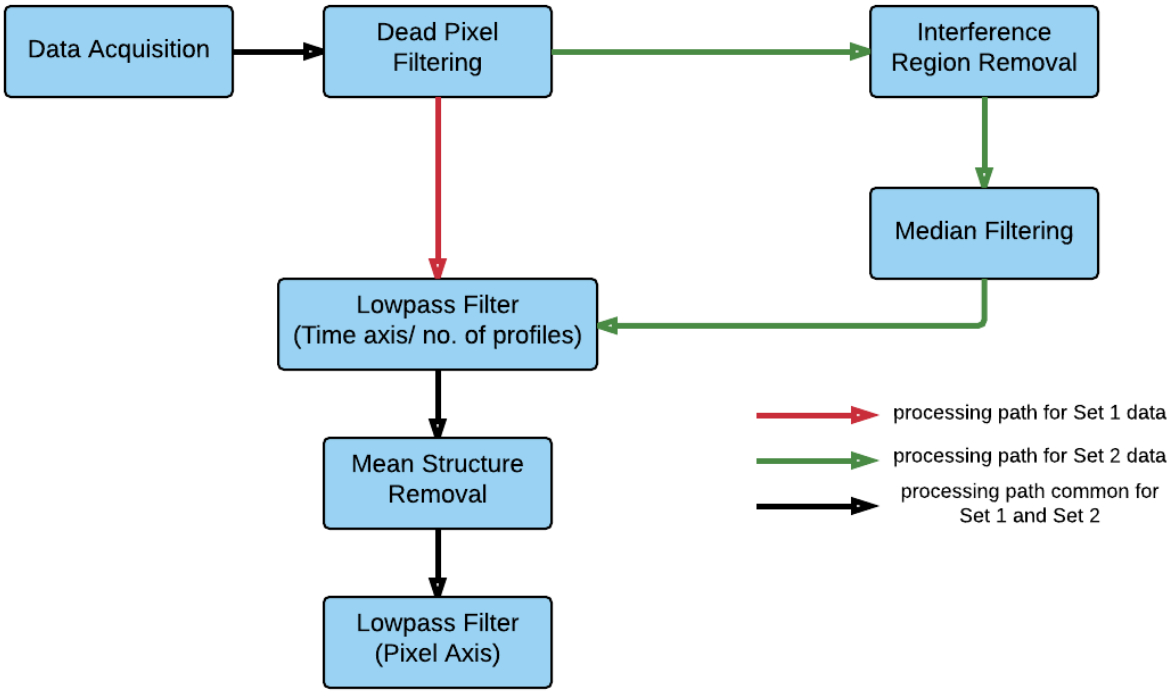

Figure 9.2 Flowchart for data processing

The processing steps are as follows

i) Dead pixel region removal: They are caused as a result of the laser not receiving accurate reflections. For further processing we remove the dead pixels since the areas are consistent and localized to the edges of measured region.

ii) Interference removal (for Test 2 data only): Considerable amount of interference is seen in Set 2 data. Interference occurs due to erroneous reflections from the measured region due to change in ambient light conditions.

iii) Median filtering (for Test 2 data only): A 25x25 window median filter is applied for removing any remaining interference/ impulse noise.

iv) Low-pass filter: After applying the median filter we apply a low-pass filter across the time axis to filter out 2.2 Hz vibrational noise (in case of Set 1) and residual noise after median filtering (in case of Set 2).

v) Mean correction: Mean of the flat area observed in measurement data is computed to obtain the average road structure. This mean road structure is then subtracted from all the profiles to highlight the deflection regions.

vi) Low-pass filter: Once the mean road structure is removed we see some residual noise around the deflection region. To remove this noise, we apply another low-pass filter along the pixels' axis.

Table 9.2: Summary of runs discussed

Run Number	Experimental Set Number	Estimated Speed
A	1	1.6 mph
B	2	1.2 mph
C	2	2.1 mph
D	2	4 mph

9.3 Tests and Results

This section provides the results for Runs A through D.

9.3.1 Run A

Figure 9.3 provides the Run A deflection.

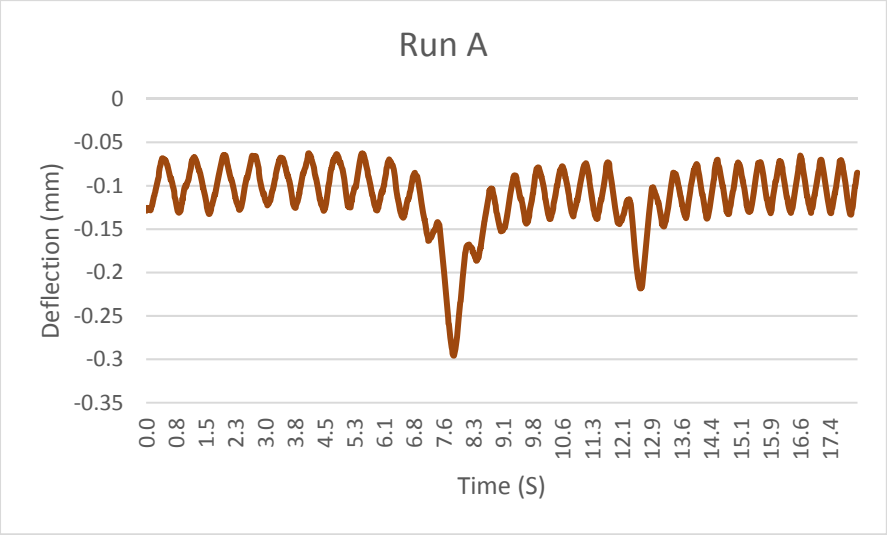

Figure 9.3 Run A: deflection obtained from RSD

For the laser data the dead pixels on the edges are removed and the mean value of a patch of 10 pixels is taken for all the profiles to obtain the data shown in Figure 9.4. The vibrations (induced by supporting structure and wind) are easily observed and have ~2.2 Hz frequency (shown in the Fast Fourier transforms plot).

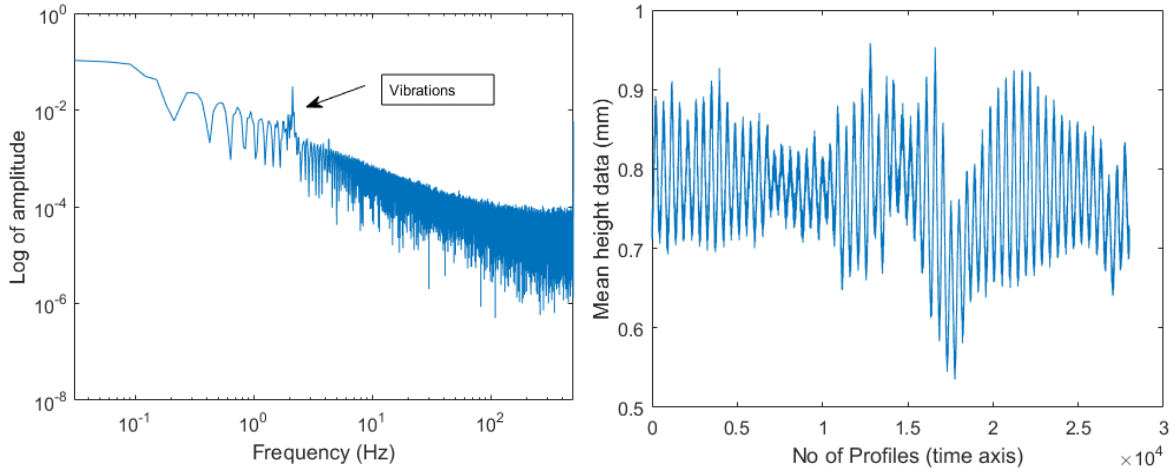

Figure 9.4 Run A: a) Fast Fourier transforms of small patch (vibration of ~2.2 Hz); b) patch of 10 pixels

To remove these vibrations, we applied a low-pass filter along the time axis. The results obtained are shown in Figure 9.5.

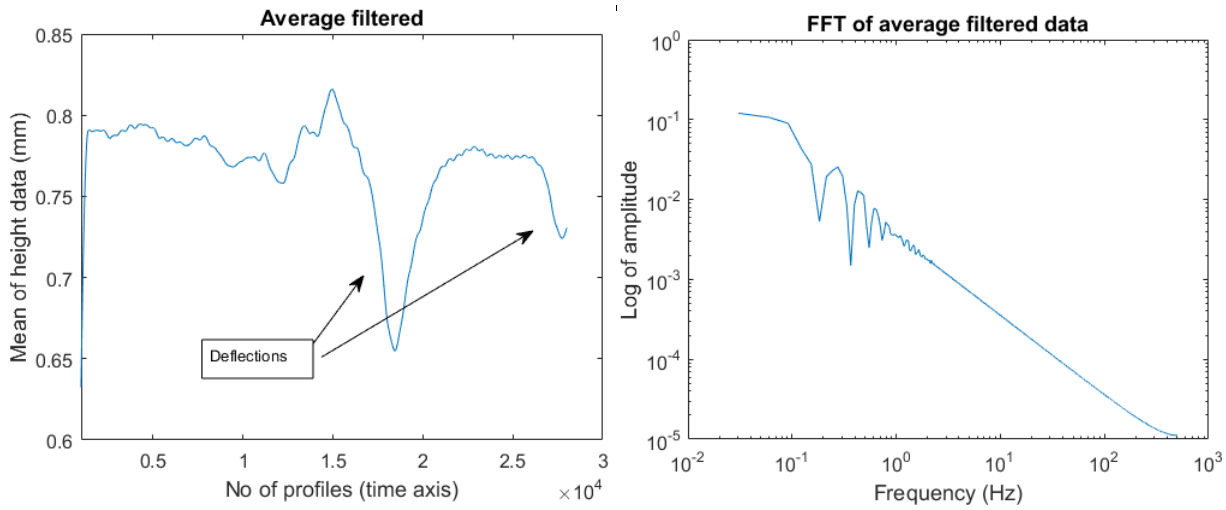

Figure 9.5 Run A: average filtered and Fast Fourier transforms for small patch (10 pixels)

Next we filter all the profiles with the low-pass filter used earlier. The road structure seen in Figure 9.6 is very stable, and thus we can subtract the road structure from all the profiles to highlight the pavement deflection.

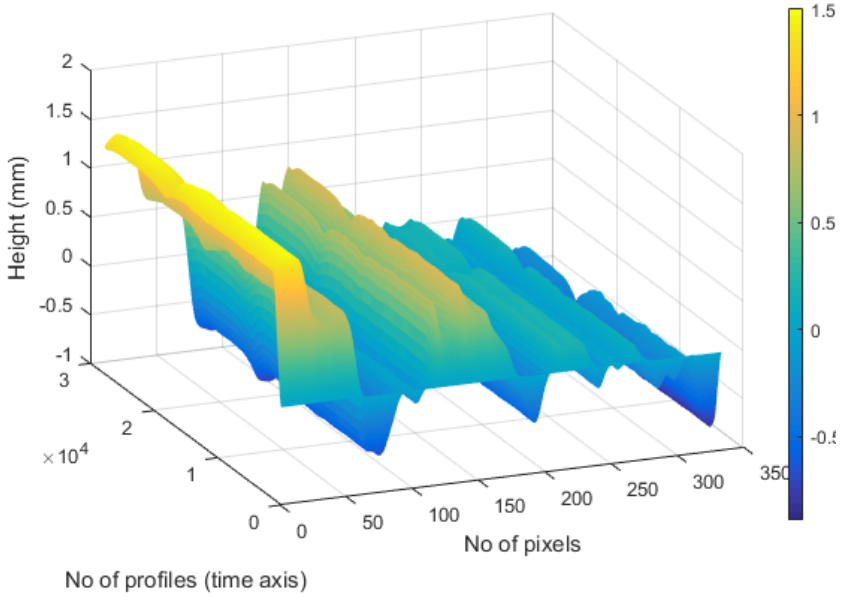

Figure 9.6 Run A: laser data after applying averaging filter across time axis

After removing the road structure, the profiles captured before deflections are flat and centered at zero. But some noise can be seen around the deflection region (marked with arrows in Figure 9.7). We suspect this noise to be from the motion of the vehicle. Thus, a low-pass filter is applied along the pixels.

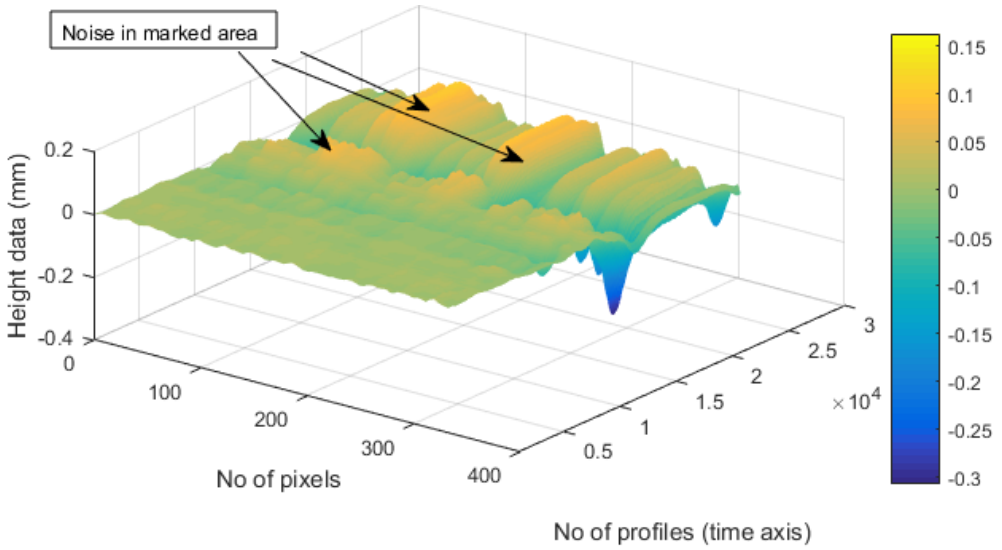

Figure 9.7 Run A: after removing road structure, noise can still be observed around deflection region

The result obtained from low-pass filtering is shown in Figure 9.8; the deflection region can be observed to increase from one end of the laser beam to the other. There are two deflections observable, one due to the front wheel and the other due to the rear wheel of the truck. Deflection from the front wheel is greater than that of the rear wheel because the front wheel is more heavily loaded (due to the engine location); see Figure 9.9. Some resolution is lost due to the low-pass filter applied.

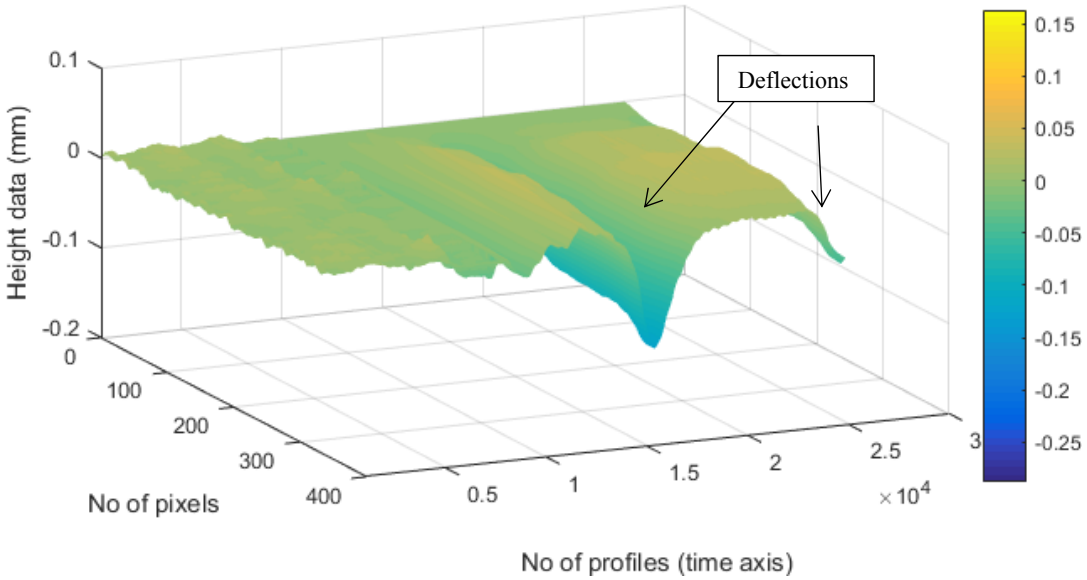

Figure 9.8 Run A: after applying low-pass filter to pixels around the deflection region; deflections are observed

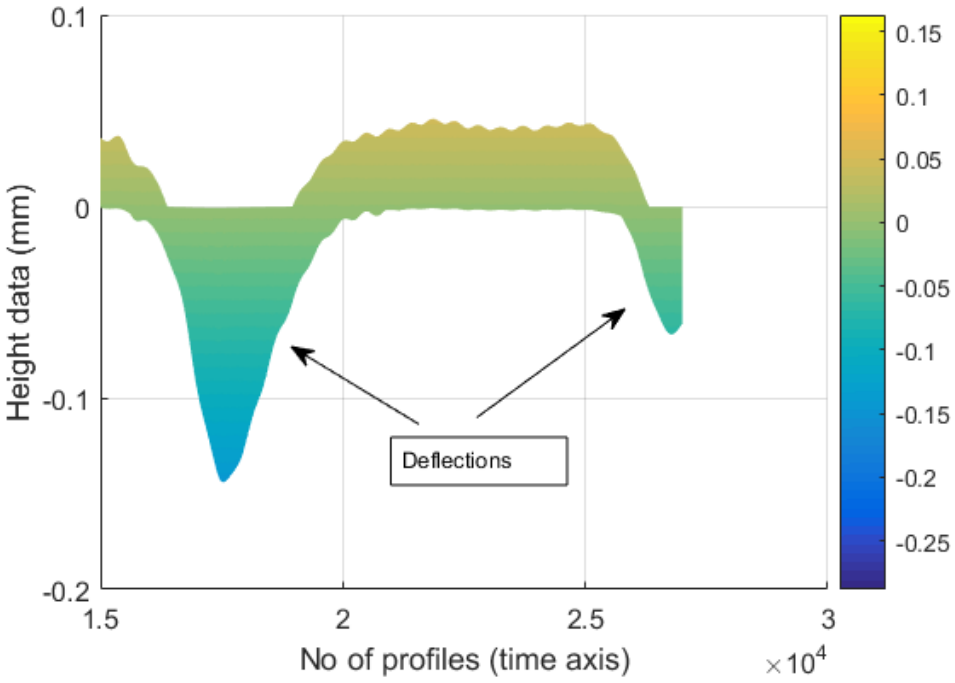

Figure 9.9 Run A: different view portraying the deflection of the front and part of the second wheel

Measurements from the accelerometer were used for verifying deflections (Figure 9.10; Table 9.3). The accelerometer does not perform very well since the vehicle is moving at lower speed.

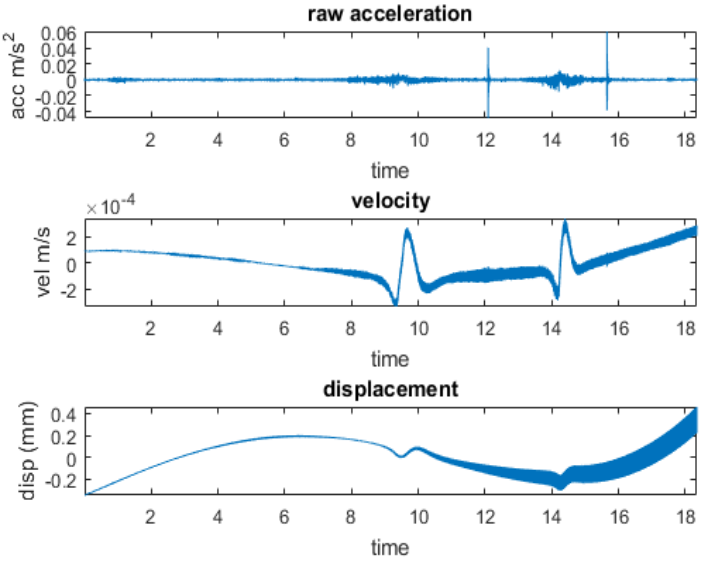

(a)

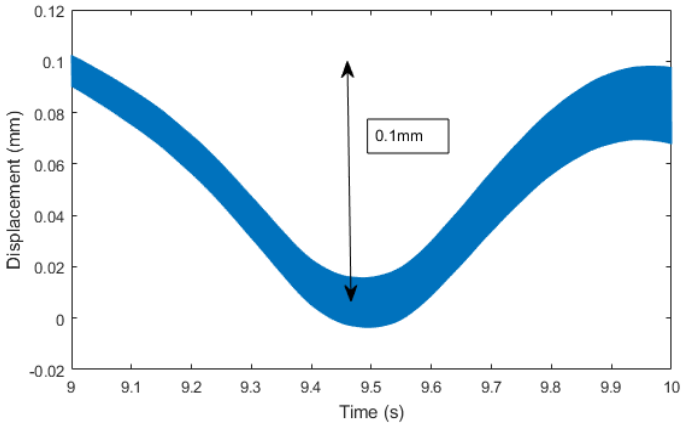

(b)

Figure 9.10 Run A: (a) acceleration, velocity, and displacement data (two dips in displacement data corresponding to deflections can be observed); (b) first dip corresponding to first wheel deflection zoomed in

Table 9.3: Comparison of results for Run A

Device	Front wheel (mm)	Back wheel (mm)	Comments
RSD	0.2	0.1	
Accelerometer	0.1	0.05	Accelerometer works more reliably at higher vehicular speeds (as in Run D)
Laser	0.15	0.07	Some measurement resolution is lost due to heavy Low-pass filtering applied to remove residual noise*

*Using a less aggressive low-pass filter along the pixels in the subsequent runs, results in more accurate deflection data from the laser.

9.3.2 Run B

It was observed that the performance of RSD remained consistent over the different speeds acquired by the vehicle (Figure 9.11).

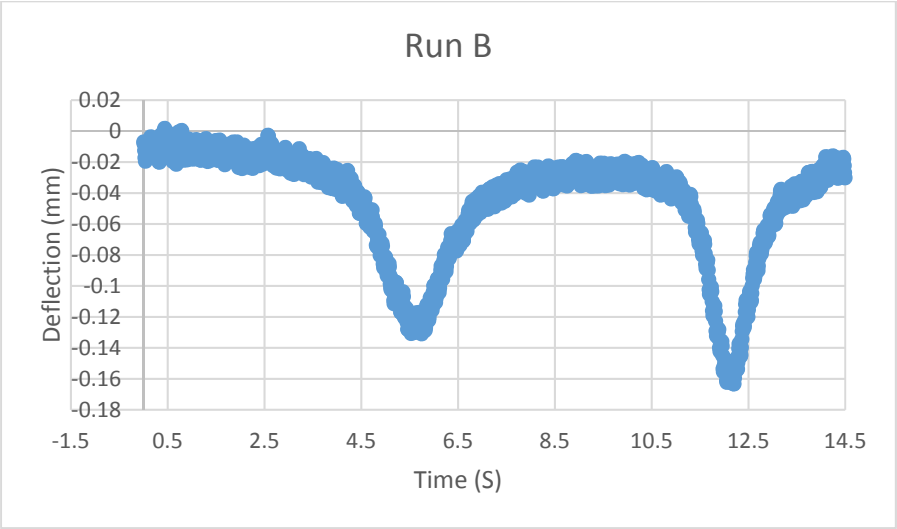

Figure 9.11 Run B: RSD data (first deflection from front wheel and second deflection from back wheel)

An accelerometer was also used for making deflection measurements. Figure 9.12 illustrates the graphs of the results obtained from the accelerometer. We can observe that the deflection from the front wheel measured by the accelerometer is too small to distinguish. As we had suspected, the accelerometer does not give very reliable results for low vehicular speed measurements.

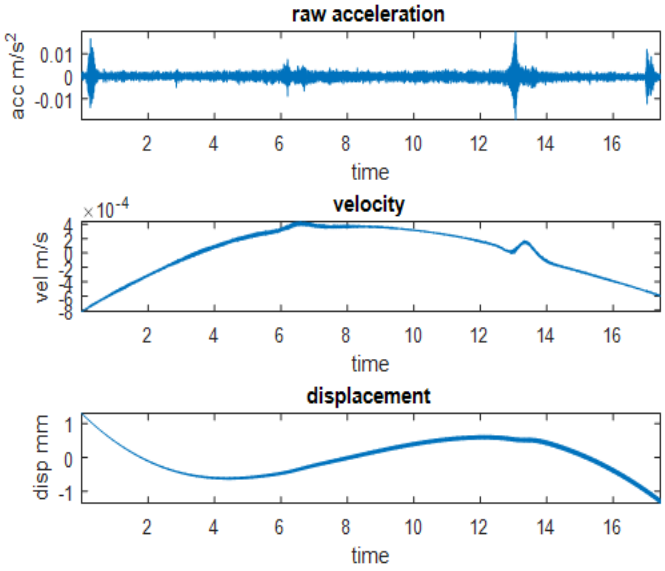

(a)

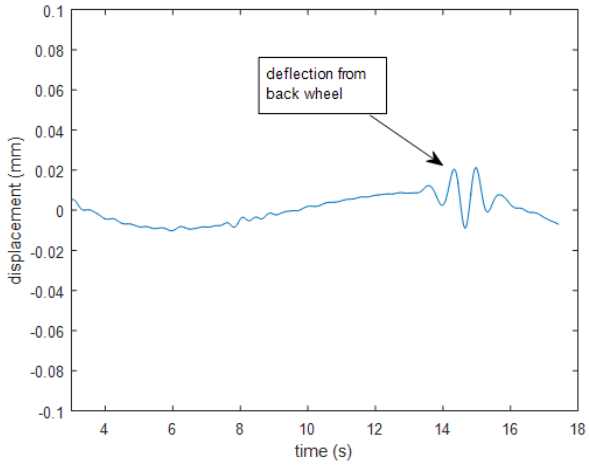

(b)

Figure 9.12 Run B: (a) acceleration, velocity and displacement data from the accelerometer; (b) filtered displacement data (first deflection from front wheel and second deflection from back wheel)

The measured data was integrated and processed to obtain velocity and displacement data. Furthermore, the displacement data is bandpass filtered to remove low frequency drift as well as unwanted high frequency content. See Figures 9.13–9.16 and Table 9.4.

In Figure 9.13, which illustrates the raw data obtained from the laser, the two sidebands are representative of dead pixels (area where no measured data is obtained) and the spikes are representative of interference (caused by ambient light condition changes). In our experiment setup the ambient light is affected due to sunlight.

Once interference region is removed along with the dead pixels, we apply a median filter to remove any of the remaining interference/impulse noise.

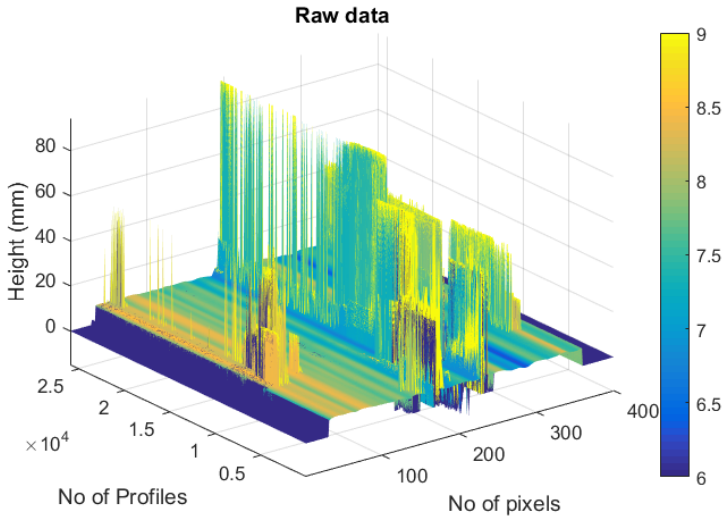

Figure 9.13 Run B: raw data from laser (dead pixels are on the edges and high amplitude spikes are representative of interference)

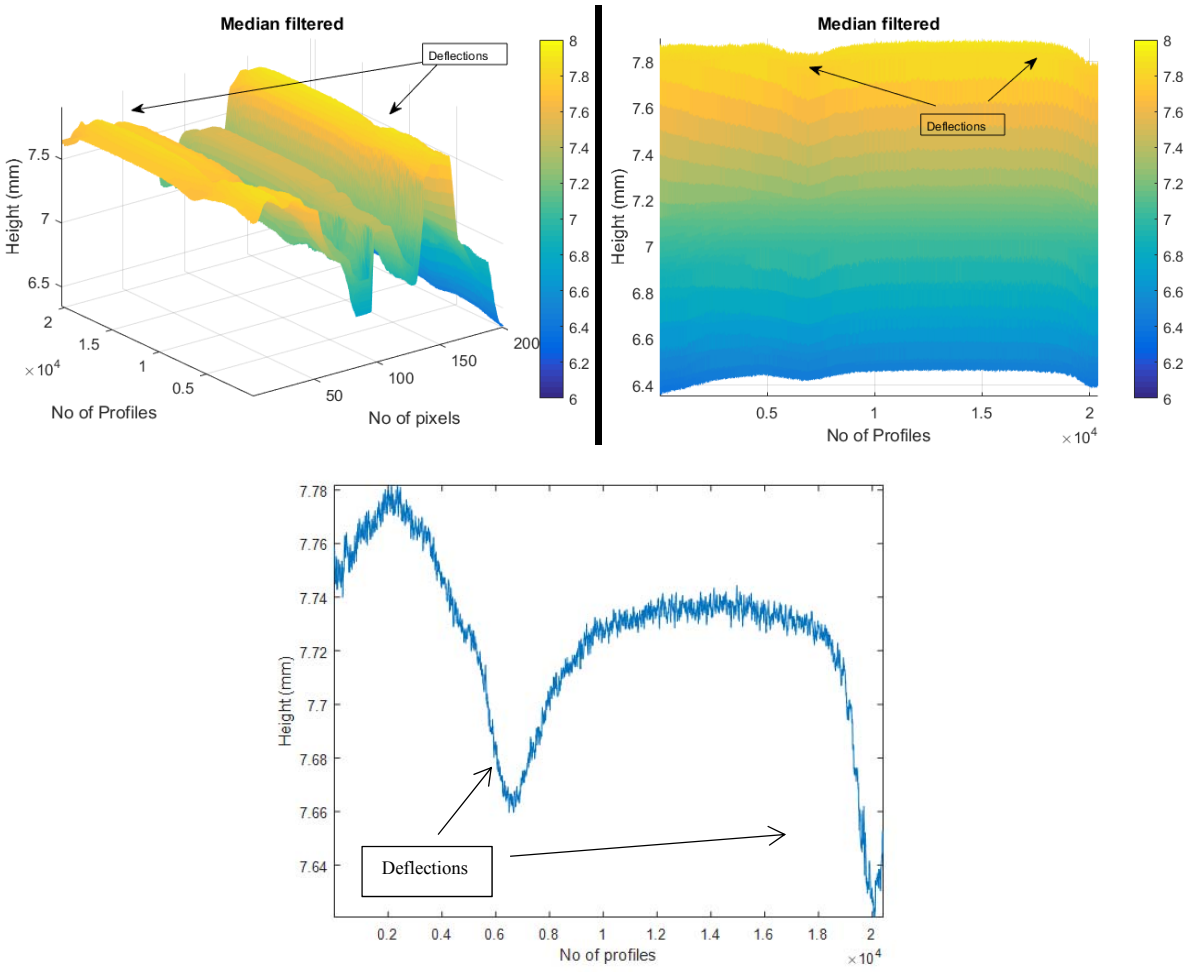

Figure 9.14 Run B: (a) median filtered laser data; (b) height vs time view of graph in (a); (c) Median filtered laser data for 10 pixels

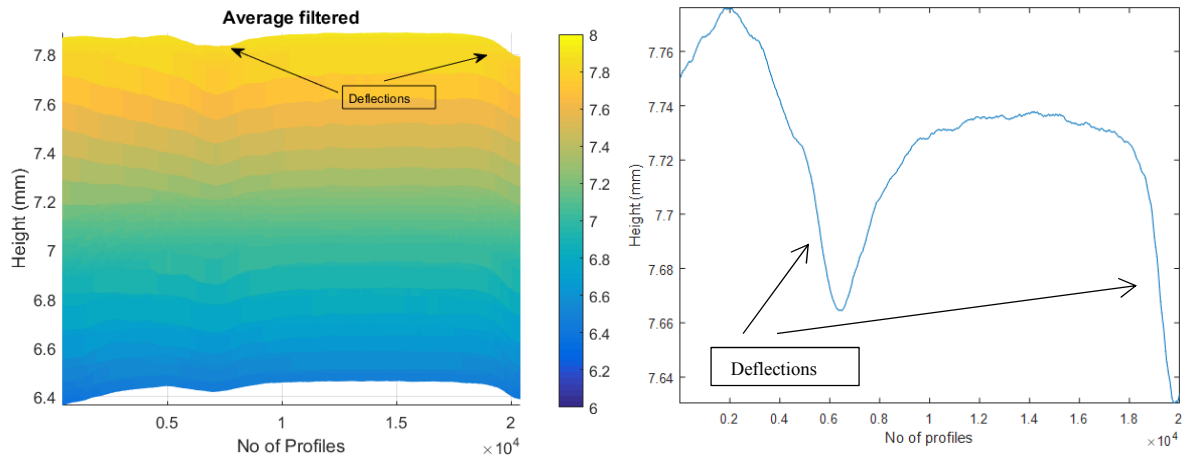

Figure 9.15 Run B: (a) low-pass filtered laser data (height vs time view of graph); (b) low-pass filtered laser data for 10 pixels

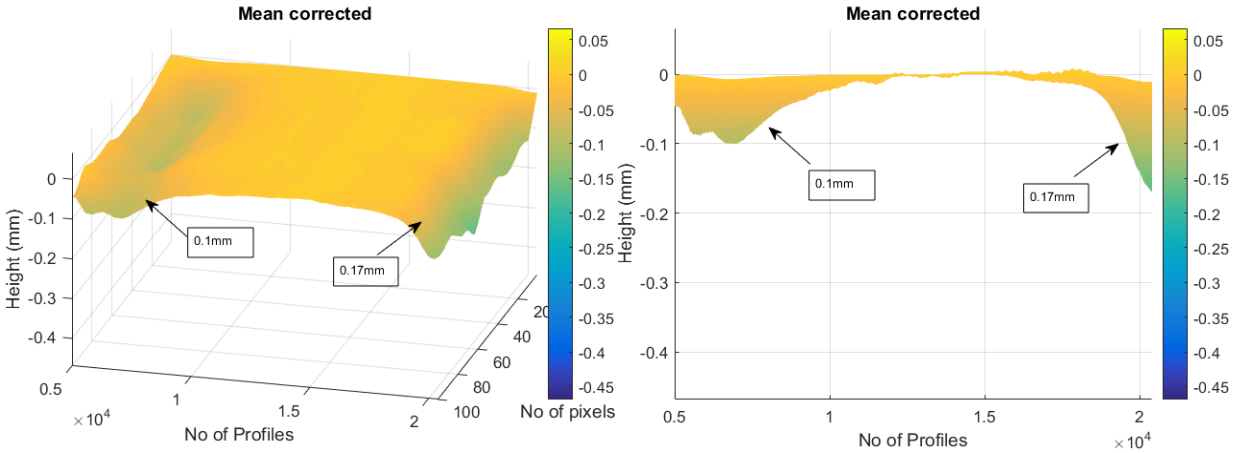

Figure 9.16 Run B: (a) mean corrected laser data with deflection marked; (b) height vs time view of graph in (a)

Table 9.4: Comparison of results for Run B

Device	Front wheel (mm)	Back wheel (mm)	Comments
RSD	0.1	0.15	
Accelerometer	NA	0.05	Accelerometer works more reliably at higher vehicular speeds (as in Run D)
Laser	0.1	0.16	

9.3.3 Run C

Pavement deflections recorded by RSD are shown in Figure 9.17.

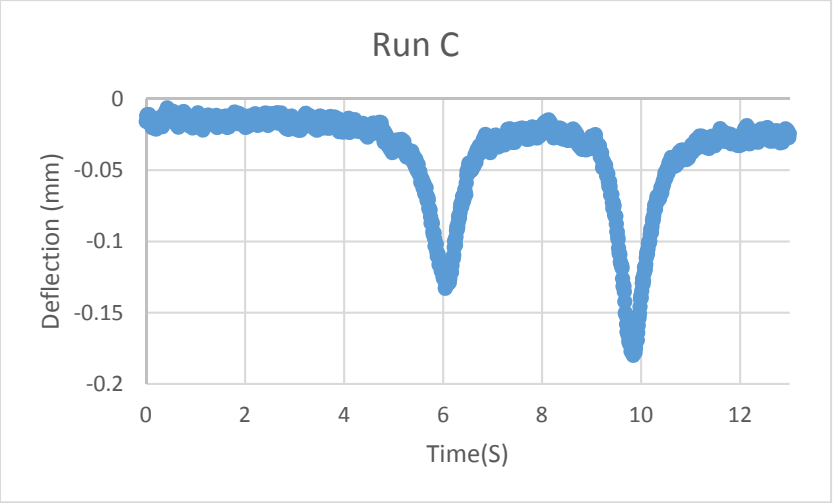

Figure 9.17 Run C: RSD data (first deflection from front wheel and second deflection from back wheel)

The corresponding acceleration, velocity, and displacement data obtained are shown in Figure 9.18.

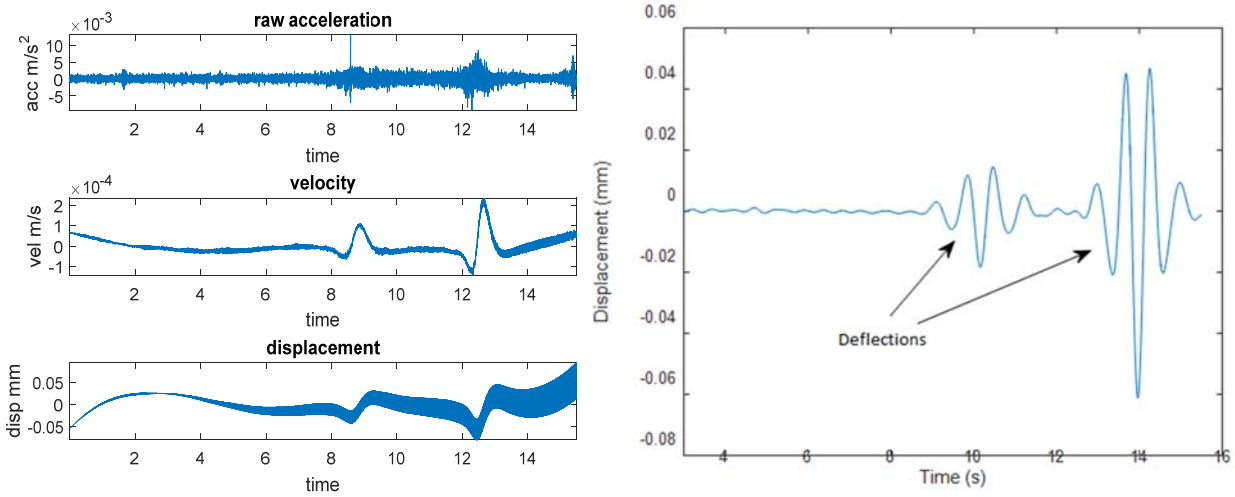

Figure 9.18 Run C; (a) acceleration, velocity, and displacement data from the accelerometer; (b) filtered displacement data (first deflection from front wheel and second deflection from back wheel)

Acceleration, velocity and displacement data is processed similarly to Run B. Since this run is conducted at double the vehicular speed of the previous two runs, we observe better performance from the accelerometer. See Figures 9.19–9.22 and Table 9.5.

The data generated from laser is processed in the same manner as discussed for Run B.

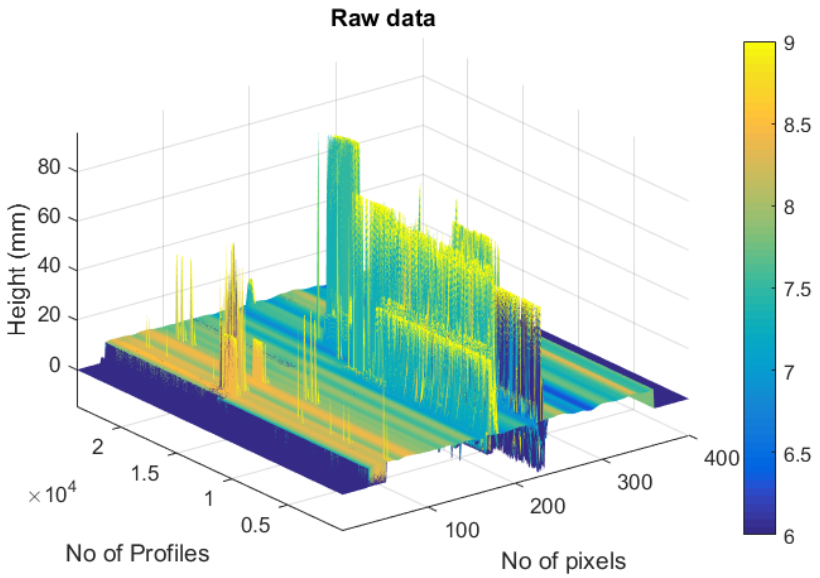

Figure 9.19 Run C: raw data from laser (dead pixels are on the edges and high amplitude spikes are representative of interference)

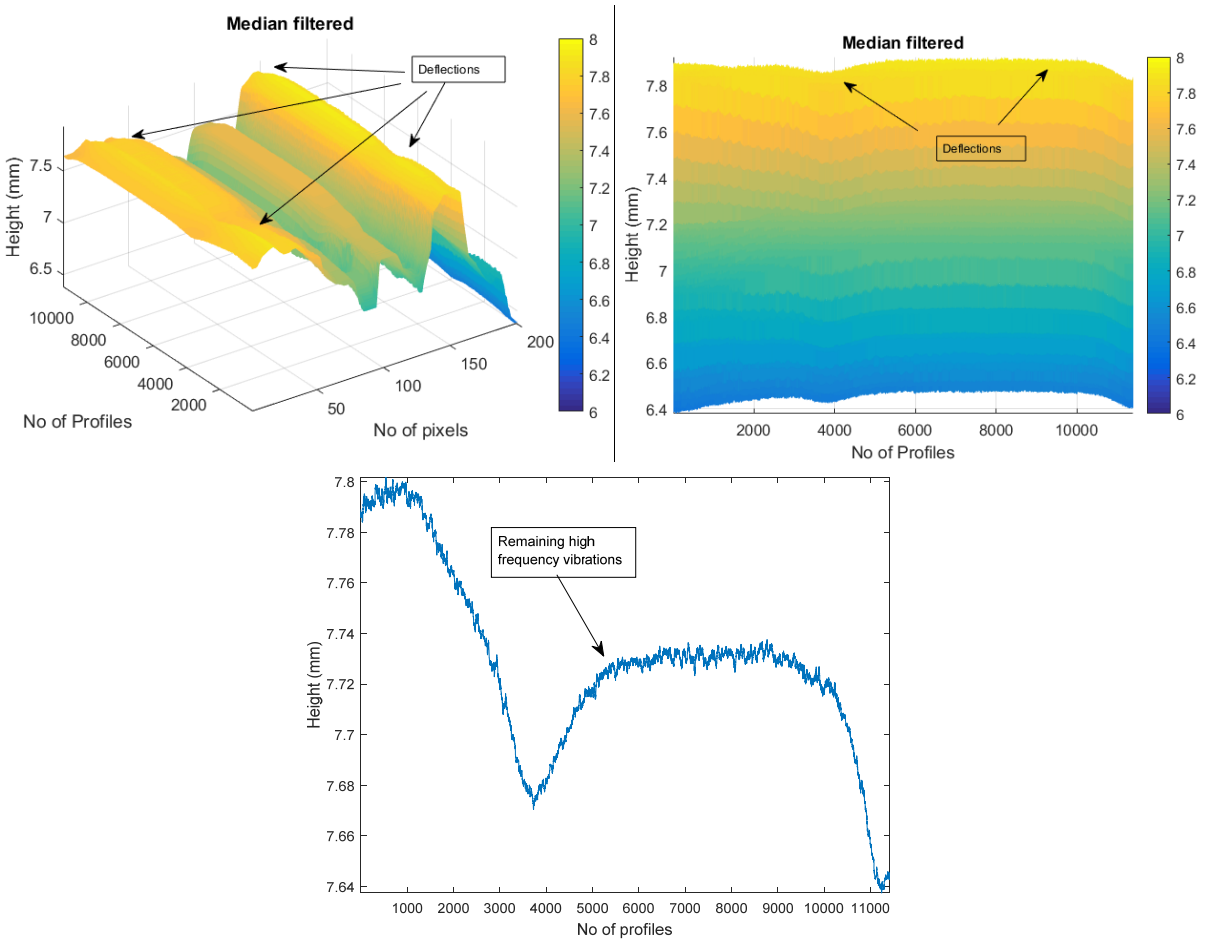

Figure 9.20 Run C: (a) median filtered laser data; (b) height vs time view of graph in (a); (c) median filtered laser data for 10 pixels

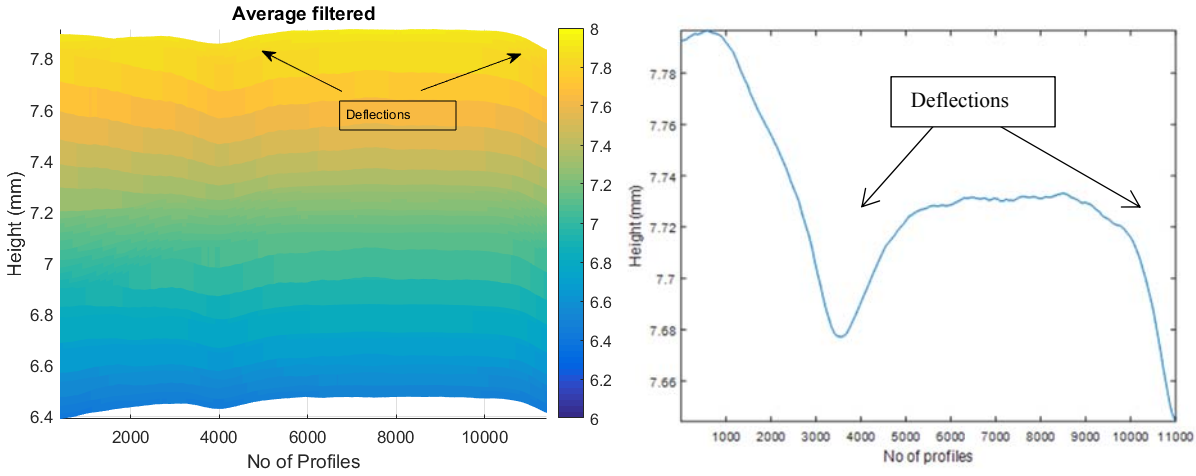

Figure 9.21 Run C: (a) low-pass filtered laser data (height vs time view of graph); (b) low-pass filtered laser data for 10 pixels

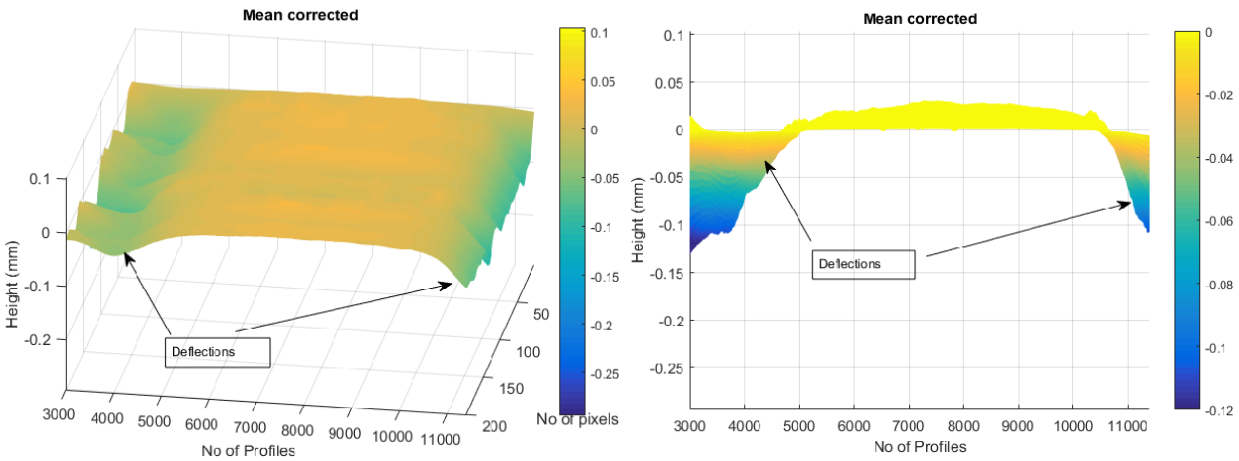

Figure 9.22 Run C: (a) mean corrected laser data with deflection marked; (b) height vs time view of graph in (a)

Table 9.5: Comparison of results for Run C

Device	Front wheel (mm)	Back wheel (mm)	Comments
RSD	0.1	0.15	
Accelerometer	0.05	0.1	
Laser	0.07	0.12	Some measurement resolutions is lost due to applying averaging filter

9.3.4 Run D

Pavement deflections recorded by RSD are shown in Figure 9.23.

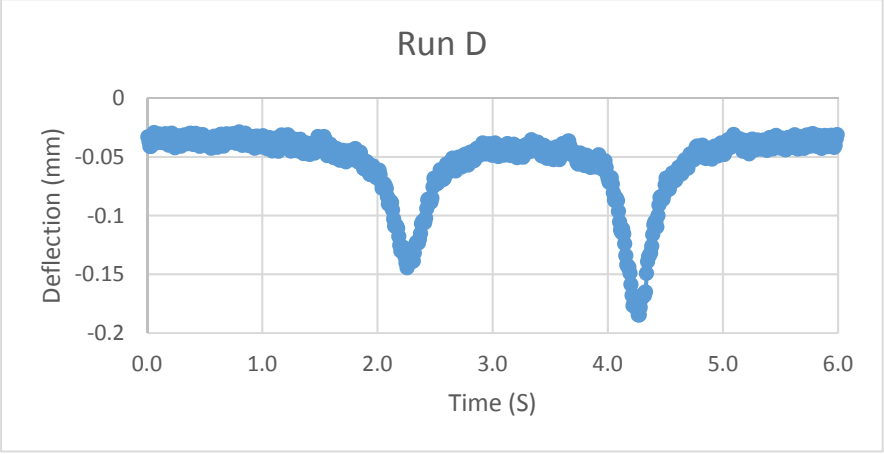

Figure 9.23 Run D: RSD data (first deflection from front wheel and second deflection from back wheel)

The corresponding acceleration, velocity, and displacement data obtained are shown in Figure 9.24.

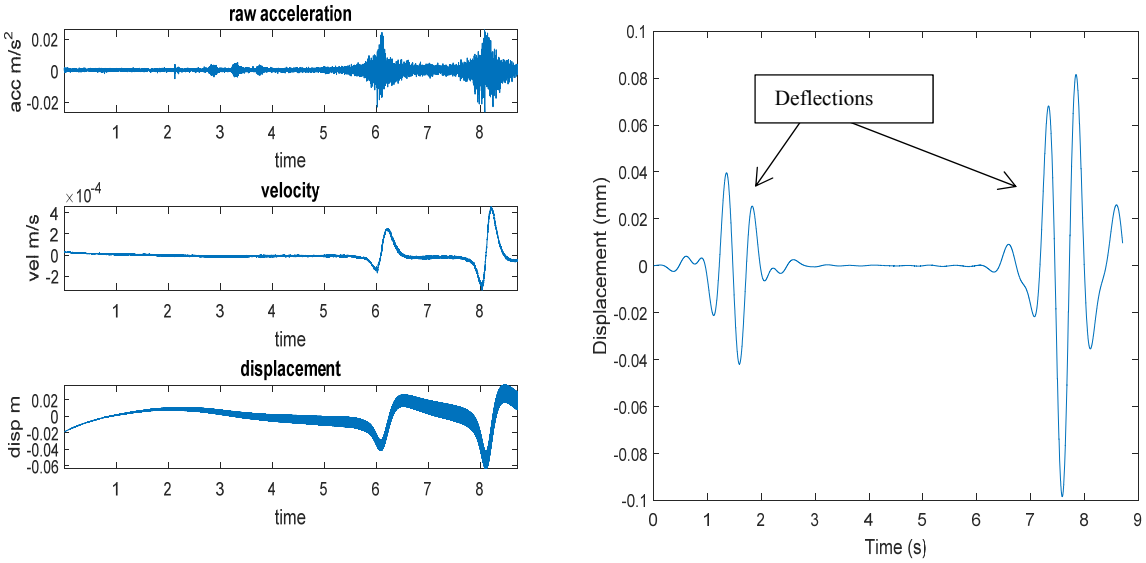

Figure 9.24 Run D: (a) acceleration, velocity and displacement data from the accelerometer; (b) filtered displacement data (first deflection from front wheel and second deflection from back wheel)

Since this run was conducted at a considerably higher speed than all the previously discussed runs, it is observed that the accelerometer performs more reliably when the vehicle is moving at faster speed. See Figures 9.25–9.28 and Table 9.6.

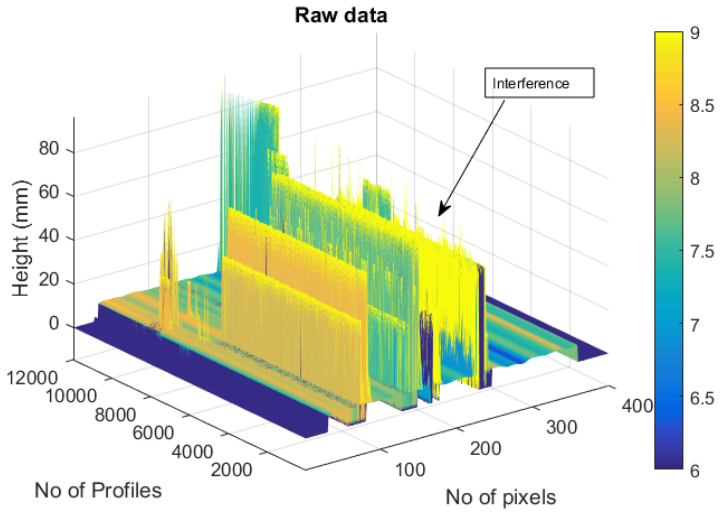

Figure 9.25 Run D: raw data from laser (dead pixels are on the edges and high amplitude spikes are representative of interference)

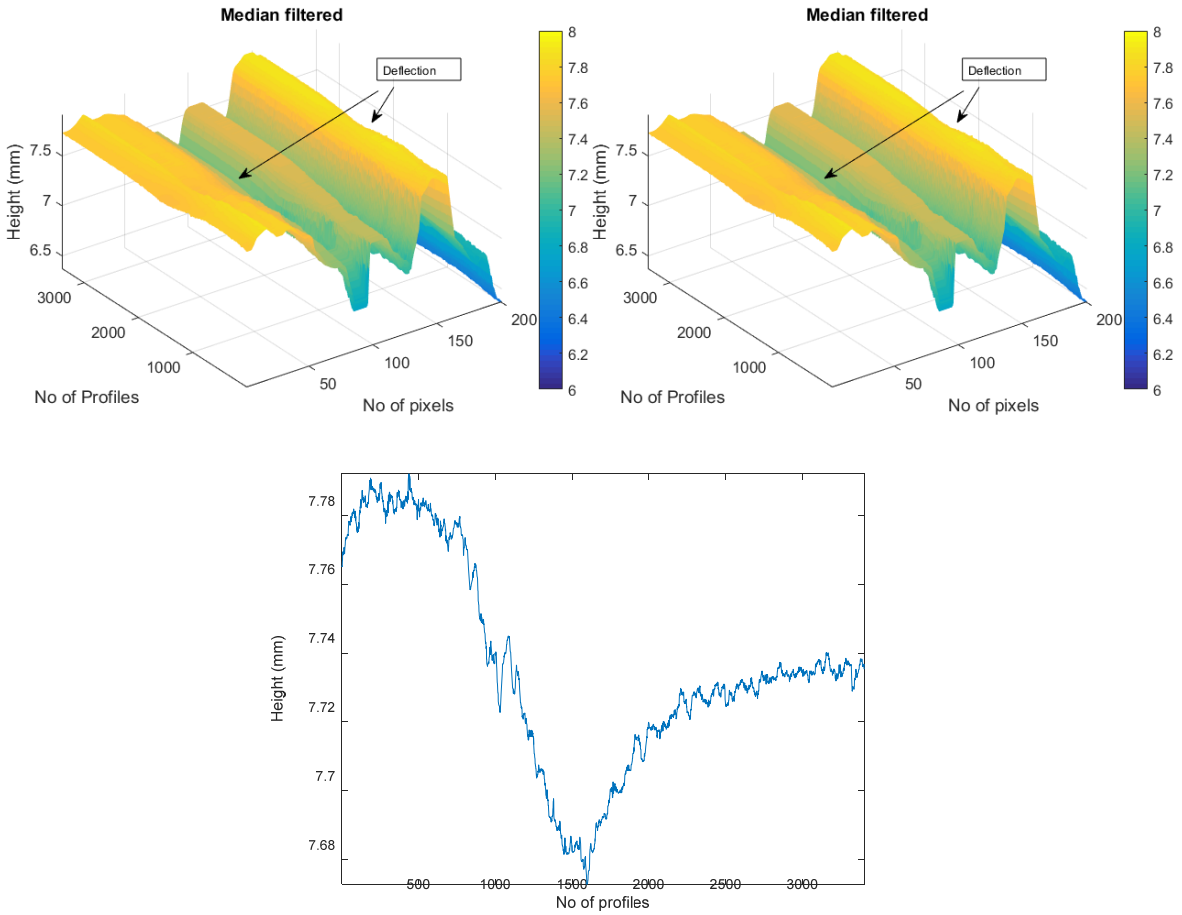

Figure 9.26 Run D: (a) median filtered laser data; (b) height vs time view of graph in (a); (c) median filtered laser data for 10 pixels

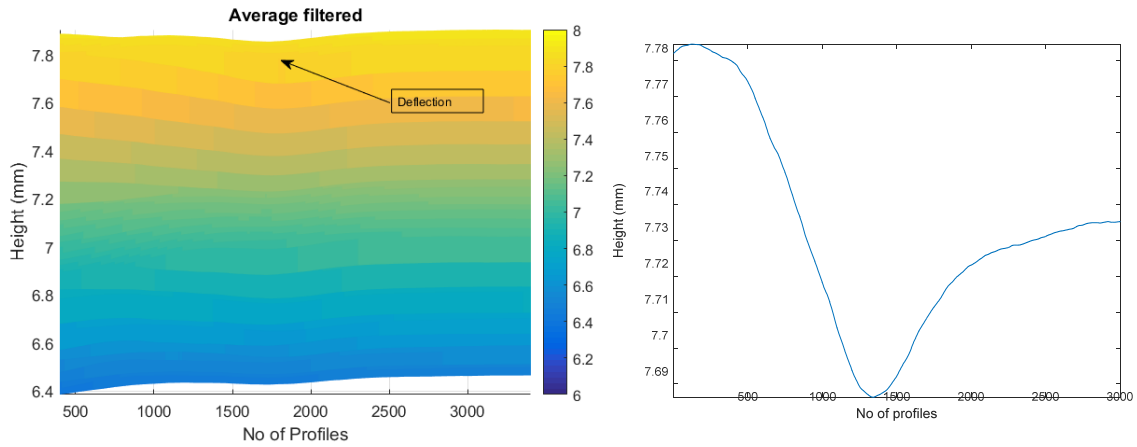

Figure 9.27 Run D: (a) low-pass filtered laser data (height vs time view of graph); (b) low-pass filtered laser data for 10 pixels

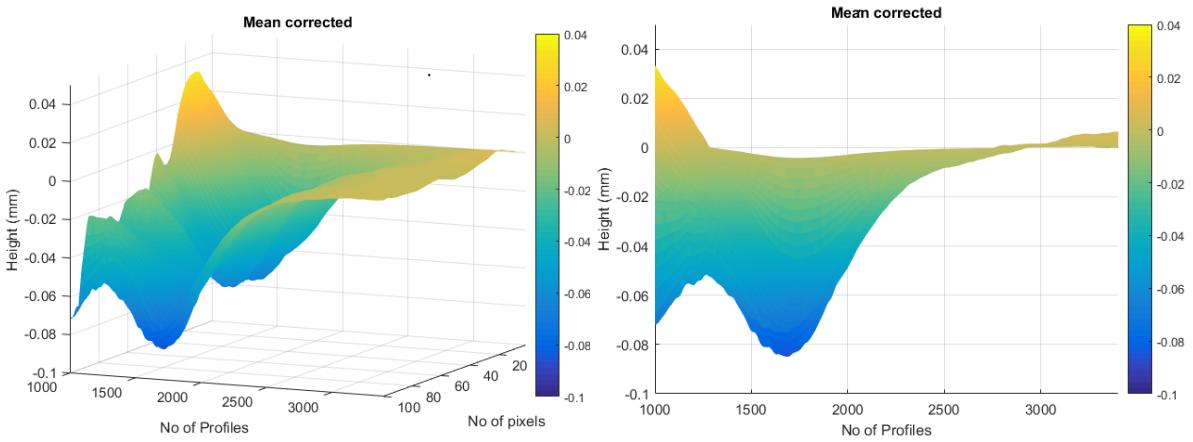

Figure 9.28 Run D: (a) mean corrected laser data with deflection marked; (b) height vs time view of graph in (a)

Table 9.6: Comparison of results for Run D

Device	Front wheel (mm)	Back wheel (mm)	Comments
RSD	0.1	0.14	
Accelerometer	0.08	0.16	Better performance of the accelerometer is observed for this run (due to higher vehicular speed).
Laser	0.09	NA	

9.4 Observation and Summary

- The laser is able to capture pavement deflections both from front and back wheels under different load conditions and for varied vehicle speeds. The deflections obtained from laser closely match up to those captured by the RSD (the reference device).
- We observe some interference in laser data (spurious reflections from road surface) when the laser measurement area is exposed to variations in ambient light. No interference is observed in Run A (when the laser was continuously in shade) and in other runs once the truck was next to the laser providing shade, confirming our initial idea that the laser should be operated in shade.
- The accelerometer suffers from drift at lower vehicle speeds and thus loses the ability to reliably measure deflections. At higher vehicle speeds we see an improvement in its performance.
- Extensive low-pass filtering of the laser data along the pixel axis leads to some loss in resolution—the larger the filter, the greater the loss in resolution.
- The 2.2Hz vibrational noise present in Set 1 (Run A) data is not present in Set 2 datasets. This confirms our belief that the vibrational noise in the first experiment originated from the cantilever structure used to mount the laser, as it was not rigid enough. We used a new rigid cantilever structure for Set 2 measurements.

- For Run D, only one deflection (from the front wheel) was measured by the laser because the data acquisition system was stopped too early. With an extra second's worth of data, the second deflection would have been captured. We believe this is an issue of the buffering system presently implemented on the computer and can be easily fixed.
- Table 9.7 lists the test descriptions and provides additional commentary.

Table 9.7: Test descriptions

Test No.	Run No.	No. of deflections from laser	No. of deflection by RSD	No. of deflections measured by accelerometer	Comments
1	4	2	2	2	
2	1	2	2	2	
2	2	1	2	2	First deflection measured by laser
2	3	1	1	2	First deflection measured by laser
2	4	1	2	2	Only first deflection by laser
2	5	1	1	2	First deflection measured by laser
2	6	1	2	2	Only first deflection measured by laser
2	7	1	2	2	Only first deflection measured by laser
2	8	1	2	2	Only first deflection measured by laser
2	9	1	2	2	First deflection measured by laser, scale of first deflection measured by accelerometer is very small
2	10	2	1	2	RSD was hit, scale of first deflection measured by accelerometer is small
2	11	2	1	1	RSD was hit, second deflection measured by accelerometer
2	12	2	1	2	RSD was hit, scale of first deflection measured by accelerometer is small
2	13	2	2	2	Scales of both deflections measured by accelerometer are very small
2	14	2	1	2	RSD was hit, scales of both deflections measured by accelerometer are very small
2	15	1	1	2	First deflection measured by laser

References

1) Andrejaši˘c, M. and I. Poberaj (2008), "*Mems Accelerometers*", Seminar Paper, University of Ljubljana, Faculty for Mathematics and Physics, Department of Physics.

2) Arraigada, M. and M. Partl. "*Calculation of displacement of measured accelerations, analysis of two accelerometers and application in road engineering*." 6th Swiss Transport Research Conference, March, 2006.

3) Arraigada, M. and M. N. Partl, S. M. Angelone and F. Martinez. *"Evaluation of accelerometers to determine pavement deflections under traffic loads*." Materials and Structures, Vol. 42, 2009.

4) Baltzer, S., Pratt, D., Weligamage, J., Adamsen, J., and Hildebrand, G., (2010). "*Continuous Bearing Capacity Profile of 18,000 Km Australian Road Network in 5 Months*," 24nd ARRB Conference, 12-15 October 2010, Melbourne, ARRB Group.

5) Bay, J. A., and Stokoe, II, K. H., (1998), "*Development of a Rolling Dynamic Deflectometer for Continuous Deflection Testing of Pavements*." FHWA/TX-99/1422-3F, FHWA/Texas Department of Transportation, Center for Transportation Research.

6) Briggs, R.C., R.F. Johnson, R.N. Stubstad, and L. A. Pierce. "*Comparison of the Rolling Weight Deflectometer with the Falling Weight Deflectometer*." Nondestructive Testing of Pavements and Backcalculation of Moduli, third volume, ASTM STP 1375, S.D. Tayabji and E.O. Lukanen, Eds., American Society for Testing and Materials, West Conshohocken, PA, 2000, pp. 444-456.

7) Doran (n.d.) "*360HD*" http://www.doranmfg.com/fleet-truck-tire-pressure-monitors-doran-360hd.htm

8) Dynatest, (n.d.), CSIR Licensed Products, Retrieved August 21, 2014 from http://www.docstoc.com/docs/74656003/CSIR-Licensed-Products.

9) Elseifi, M. et al. (2012) "*Implementation of Rolling Wheel Deflectometer (RWD) in PMS and Pavement Preservation*", FHWA/11.492, Department of Civil and Environmental Engineering, Louisiana State University.

10) Ferne, B. W., P. Langdale, N. Round, and R. Fairclough. "*Development of a Calibration Procedure for the U.K. Highways Agency Traffic-Speed Deflectometer."* Transportation Research Record: Journal of the Transportation Research Board, No. 2093, Transportation Research Board of the National Academies, Washington, D.C., 2009, pp. 111–117.

11) Gedafa, D.S., M. Hossain, R. Miller, and D. Steele. "*Network Level Pavement Structural Evaluation Using Rolling Wheel Deflectometer.*" Paper No. 08-2648 Presented at the 87th Transportation Research Board Annual Meeting, Washington, D.C., 2008.

12) Gedafa, D.S., "*Estimation of Remaining Service Life of Flexible Pavements from Surface Deflections*." PhD dissertation. Kansas State University, 2008.

13) Geem, C. V., "*Overview of Interpretation Techniques Based on Measurement of Deflections and Curvature Radius Obtained with the Curviameter*," Presentation, 6th European FWD User's Group Meeting, 10 June – 11 June, 2010, Sterrebeek.

14) Imou, K., M. Ishida, T. Okamoto, Y. Kaizu, A. Sawamura, N. Sumida. "*Ultrasonic Doppler Sensor for Measuring Vehicle Speed in Forward and Reverse Motions Including Low Speed Motions*." Agricultural Engineering International: the CIGR Journal of Scientific Research and Development. Manuscript PM 01 007. Vol. III.

15) Jenkins, M. "*Geometric and Absolute Calibration of the English Highways Agency Traffic Speed Deflectometer.*" Young Researchers Seminar, 2009.

16) Katicha, S. W. and G. W. Flintch. "*Field Demonstration of the Traffic Speed Deflectometer in New York."* Transportation Research Record: Journal of the Transportation Research Board. 2015.

17) Krarup, J., S. Rasmussen, L. Aagaard, P. Hjorth. "*Output from the Greenwood Traffic Speed Deflectometer.*" Presented at the 22nd ARRB Group Conference, 2006.

18) Muller, W.B. and J. Roberts. *"Revised approach to assessing traffic speed deflectometer data and field validation of deflection bowl predictions."* International Journal of Pavement Engineering, Vol. 14, 2013.

19) Pedersen, L. "*Viscoelastic Modelling of Road Deflections for use with the traffic speed deflectometer.*" An industrial Ph.D. study in collaboration with Greenwood Engineering, Technical University of Denmark and the Ministry of Science and Innovation. 2012

20) PCB® a, (n.d.) "*Triaxial MEMS DC accelerometer. Model: 3713B112G Specifications*" http://www.pcb.com/Products.aspx?m=3713B112G

21) PCB® b (n.d.) "*Series 5400 Multi-Axis Wheel Force Transducer*", http://www.pcb.com/auto/MultiAxis_Wheel_Force_Transducer.aspx,

22) Prozzi, J. A., (1994), "*The Non-destructive Measurement of Engineering Properties of Roads*," IR 93/371, Council for Scientific and Industrial Research, Pretoria, South Africa.

23) RoaDyn® (n.d.) "*S6XT sp System 200*" http://www.kistler.com/tw/en/product/force/9262A1,

24) Ryynanen, T., T. Pellinen and J. Belt*. "The use of accelerometers in the pavement performance monitoring and analysis*." Materials Science and Engineering, Vol. 10, 2010.

25) Steele, D., J. Hall, R. Stubstad, A. Peekna, and R. Walker. "*Development of a High Speed Rolling Wheel Deflectometer,*" Presentation made at the 88th Transportation Research Board Annual Meeting, Washington, D.C., 2009.

26) Stokoe, II, K. H., Lee. J. –S., Lewis, M., Hayes, R., Scullion, T., and Liu, W., (2013), "*Developing a Testing Device for Total Pavement Acceptance – Final Report*," Publication Report No. FHWA/TX-13/0-6005-3, FHWA/Texas Department of Transportation, Center for Transportation Research and Texas Transportation Institute.

27) Weligamage, J., Piyatrapoomi, N., and Gunapala, L., (2010) "*Traffic Speed Deflectometer – Queensland Trial*," Retrieved August 21, 2014, from http://www.tmr.qld.gov.au...ads-technical-journal.aspx.

28) Weligamage, J., N. Piyatrapoomi, L. Gunapala. "*Traffic Speed Deflectometer*." Queensland Trial.

29) Zofka, A., J. Sudyka. Traffic speed deflectometer (TSD) measurements for pavement evaluation. International Symposium Non-destructive Testing in Civil Engineering (NDT-CE), 2015.